Physical properties of the plasma membrane studied by local probe techniques

**Dissertation an der Fakultät für Physik
der Ludwig-Maximilians-Universität
München**

vorgelegt von

**Arnd Pralle
aus Bremen**

München, den 2. November 1998

Zusammenfassung

Im Rahmen dieser Arbeit wurden physikalische Meßmethoden entwickelt, um die Struktur und Dynamik der Plasmamembran lebender Säugetierzellen zu untersuchen. Dabei lag der Schwerpunkt zum einem auf der mechanischen Kopplung der Membranlipidschicht zu dem darunter liegenden, unterstützend wirkenden Zytoskelett, und zum anderen auf der Beweglichkeit einzelner Membrankomponenten innnerhalb der Membranlipidschicht. Ausgangspunkte für die Entwicklung neuer Methoden waren die Rasterkraftmikroskopie (RKM) und ´single-particle tracking´ (SPT). Die RKM ermöglicht die Abbildung von Ober‡ächen mit hoher Au‡ösung in physiologischer Umgebung, so lange die Wechselwirkungskräfte die Probenober‡äche nicht zu sehr deformieren. SPT ist eine Technik, um die Bewegung von einzelnen Molekülen zu verfolgen. Dafür werden diese mit Polysteren-kügelchen oder kolloidem Gold markiert und mit Videomikroskopie beobachtet. Auf diesen Techniken aufbauend wurden folgende Verfahren und Geräte für diese Arbeit entwickelt:

Das Scanning-Photonic Force Microscope (SPFM) als Analogon zum RKM: In einer Laserfalle (einem mit einem Objektiv hoher Apperatur (100x, NA 1.3) fokussierten infraroten (IR) Laser) wird ein Fluorophor gefülltes Polysteren-kügelchen (bead, r=0.1¹m) gefangen. Die Fluorophore des als Sonde verwendeten Kügelchens werden über einen Zwei-Photonen Prozeß durch den IR-Laser zur Fluoreszenz angeregt. Eine Auslenkung aus der Halteposition durch eine äußere Kraft führt zum Abfall der Fluoreszenz. Im SPFM wird die Sonde mit Hilfe des Lasers analog zum mechanischen Hebelarm im RKM über die Probe bewegt. Dabei wird wie beim RKM die Auslenkung und somit Kraft gemessen. Die wesentlichen Unterschiede sind die fehlende mechanische Verbindung zur Umwelt, die ein Abrastern beliebiger transparenter 3D-Strukturen ermöglicht, die extrem kleine Federkonstante des Sensors (0.1-1¹N/m), welche daher besser an die Elastiztät von biologischen Objekten angepaßt ist, sowie die stark reduzierte viskose Dämpfung der kleineren Sonde, was schnelleres Messen ermöglicht.

Das Photonic Force Microscope (PFM) ist die Weiterentwicklung des SPFM. Bei der verwendeten kleinen Federkonstante werden die thermischen Positions‡uktuationen sehr groß. Daher wurde ein Detektor entwickelt, der Messung der Position der Sonde in der Falle in drei Dimensionen mit Nanometer Ortsau‡ösung und 50kHz-Bandbreite ermöglicht. Der Detektor basiert auf der Interferenz des an der Sonde vorwärts gestreuten Laserlichts mit dem ungestreuten Licht. Dieses Prinzip wurde zuvor nur für seitliche Auslenkungen entlang einer Achse verwendet und erstmals in dieser Arbeit drei dimensional angewandt. Die vollständige theoretische Beschreibung des Detektorsignals ist ebenfalls ein Novum. Im PFM werden mit diesem Detektor die thermischen 3D-Positions‡uktuationen einer durch den Laser in einem Volumen von 0.1*0.1*0.6¹m^3 gehaltenen Sonde analysiert. Zusätzlich wirkende Potentiale und die Viskosität des umgebenden Mediums können gemessen werden.

Contents

Folgende biologische Fragestellungen wurden im Rahmen dieser Arbeit mit obigen Methoden bearbeitet:

Die Zellmembranen von Neuronen und Fibroblasten wurden mit dem RKM und dem SPFM abgebildet. Während das SPFM die Oberfläche der Membran zeigte, waren auf den RKM Bildern im wesentlichen Strukturen des unterstützenden Zytoskeletts sichtbar.

Mit der Laserfalle wurden Membranlipidfäden aus den Zellmembranen verschiedener Zelltypen extrahiert. Während dies bei Neuronen und Erythrozyten leicht möglich war, mußte in Leberzellen erst das Aktinmembranskelett depolymerisiert werden bevor eine Fadenbildung möglich war. In Neuronen war der viskose Widerstand gegen das Fadenziehen am Zellkörper höher als weit entfernt von diesem an den Zellausläufern. Diese Unterschiede wurden auf eine stärkere Bindung der Lipidmembran an das Membranskelett und eine höhere Proteinkonzentration am Zellkörper zurückgeführt.

Ein Fluß der Membrankomponenten in jungen, wachsenden Neuronen von den Enden der Zellausläufer bis auf den Zellkörper wurde mit SPT gemessen. In entwickelten Neuronen wurde eine solcher Fluß nicht mehr beobachtet. Statt dessen wurden teilweise Diffusionshindernisse entdeckt.

Die 3D Analyse des thermischen Rauschens im PFM wurde genutzt, um die viskose Reibung einzelner Membranproteine in der Zellmembran von Fibroblasten zu messen und die Bindung dieser Proteine zum Zytoskelett zu untersuchen, sowie die Membranelastizität zu bestimmen ($k=5^{1}$N/m). Die viskose Reibung der GPI-verankerten Placetal Alkaline Phosphatase (PLAP, $3.3 \cdot 10^{-9}$ Pa·s·m) war wesentlich größer als die des transmembranen Transferrin Rezeptors (TrfR, $1.6 \cdot 10^{-9}$ Pa·s·m). Nach Extraktion des Cholesterins aus der Zellmembran sank die viskose Reibung der PLAP unter den Wert vom TrfR ($0.6 \cdot 10^{-9}$ Pa·s·m). Während zuvor weder die PLAP noch der TrfR aus der Membran gezogen werden konnten, genügten nach der Cholesterinextraktion Pikonewton Kräfte, um die GPI-verankerte PLAP von der Membrane zu entfernen. Dieses wird durch ein Auflösen der durch Cholesterin stabilisierten Lipidmikrodomänen erklärt, an welcher GPI-verankerte Proteine binden. Durch Anwendung der Saffman-Delbrück Theorie der Proteindiffusion in Lipidbilayern wurde aus den Messungen der viskose Reibung die Membranviskosität (0.16 Pa·s) und die Größe der Lipidmikrodomänen (r=26nm), an welche die PLAP gebunden ist bestimmt.

Abbreviations

AFM	-	Atomic Force Microscopy
BFP	-	Back-focal Plane
BHK	-	Baby Hamster Kidney cells
BSA	-	Bovine Serum Albumin
ChTx	-	Cholera Toxin
CML	-	Carboxyl-modi...ed Latex
DIC	-	Di¤erential Interference Contrast
DIG	-	Detergent-Insoluble Glycolipid-enriched complex
FRAP	-	Fluorescence Recovery after Photobleaching
FSG	-	Fish Skin Gelatin
GFP	-	Green Fluorescent Protein
GPI	-	Glycophosphatinositol
HA	-	Hemagglutinin
MDCK	-	Madine-Darby Canine Kidney cells
MFM	-	Magnetic Force Microscopy
MSD	-	Mean-square Displacement
PLAP	-	Placental Alkaline Phosphatase
PBS	-	Phosphat Bu¤ered Saline
PFM	-	Photonic Force Microscopy
RMS	-	Root-mean Square
QPD	-	Quadrant Photodiode
SEM	-	Scanning Electron Microscopy
SFM	-	Scanning Force Microscopy
SPM	-	Scanning Probe Microscopy
SPT	-	Single Particle Tracking
STM	-	Scanning Tunneling Microscopy
TM	-	Tapping Mode
TNA	-	Thermal Noise Analysis
TrfR	-	Transferrin Receptor
TrfR¢T	-	TrfR with truncated cytoplasmic tail

Part I

Preface

1.1 Introduction

The past decade has seen a rapid development of tools to measure the properties of individual molecules. Especially mechanical properties of single proteins became accessible by the development of force spectroscopy using the scanning force microscope and di¤erent types of electro-magnetic traps. First applications were the measurement of intermolecular forces between ligand-receptor pairs [Moy et al., 1994], and of intramolecular forces in polymers and proteins [Rief et al., 1997] .

So far, little is known on how the interaction of individual molecules with their environment leads to the assembly of larger structures. In cell biology one important and easily accessible structure is the cell membrane. The cell membrane, separating the intra-cellular volume from the extra-cellular space, provides a multifunctional interface that has to allow a controlled passage of proteins and other molecules. The structure of several membrane components is well studied. However, little is known on their relative location and dynamic in the membrane because the techniques applied need to disintegrate the components or do not provide the required spatial and temporal resolution. The general concept of the membrane is still the ‡uid-mosaic model [Singer and Nicolson, 1972], although the vast functions and specialized components point toward a more structured system.

Hence, the aim of this thesis work was to develop methods yielding information on the interaction of an individual molecule with its natural environment, i.e. the plasma membrane.

Investigation of mechanical properties include the application of a probe force which is require to be extremely low in lipid membranes to minimize the perturbations. Therefore, the …rst part of this thesis work included the development of a scanning force microscope capable of measuring forces in the pN range and below.

The instrument uses a small sphere held in a laser gradient trap as a force sensor. The small spring constant of such an instrument leads to increased thermal position ‡uctuations which is often thought to limit measurements. In this thesis, methods to analyze the three-dimensional thermal position ‡uctuations of a probe in a laser trap were developed to obtain information about the three-dimensional potential sensed by the probe and about the viscous damping of the probe. These methods lead to the development of the photonic force microscope (PFM). The con…nement of the probe to a small volume ($0.1 ¢ 0.1 ¢ 0.6 \, ^1m^3$) allows localized measurements of interactions, potentials, and di¤usion of single molecules on the nanometer scale.

In this work, the PFM was applied to investigate the potentials anchoring individual proteins and to measure the viscous drag of individual molecules in the membrane. Measurements of an increased local viscous drag of some membrane proteins, provided evidence that these were part of microdomains that moved as one entity. The theory of di¤usion in a bilayer was applied to determine the size of these domains.

The PFM developed is not restricted to biological applications, but can be used more general to study the in‡uence of surfaces on the motion of particles in nanoscale devices.

1.2   The structure of the plasma membrane

The following section summarizes the current knowledge and is mainly based on the book "Molecular biology of the cell" [Alberts et al., 1994] and recent publications.

   A cell is compartmentalized by membranes formed of lipid bilayers. These consist of a variety of lipids and speci...c proteins. The outer surface of cells, the plasma membrane, separates the intra-cellular or cytoplasmic volume from the extra-cellular or exoplasmic space. The ‡uid-mosaic model from Singer and Nicolson [1972] describes the membrane as a ‡uid lipid bilayer, in which freely di¤using membrane proteins are embedded. This ‡uid-mosaic model provided the framework for the thinking about the structure and the dynamics of cellular membranes during the past 25 years. But by now, several observations suggest a more structured model of the plasma membrane. First, the plasma membrane provides a multifunctional interface of the cell to its environment: proteins are taken up or secreted, signals to the cell are passed through the membrane, and ion gradients across the membrane are maintained within tight limits. The speci...city of all mentioned functions would be di¢cult to achieve in the ‡uid-mosaic model. Secondly, the membrane contains a large variety of special lipids, which in some cells are distributed unevenly over the surface. The ‡uid-mosaic model provides no explaination for this variety.

Building blocks of the plasma membrane are lipids and proteins   About 50% of the mass of the plasma membrane are lipids. The main lipid components are glycerophospholipids (55%), glycosphingolipids (5%) and cholesterol (20%). Concentrations might vary depending on the cell type. The glycerophospholipids are composed of a hydrophilic headgroup connected by a glycerol to two hydrophobic acyl-chains. In the plasma membrane of mammalian cells these acyl-chains are about 16 to 18 carbon atoms in long, and one chain is completely saturated while the second often contains double bonds (i.e. unsaturated). The sphingolipids of the plasma membrane are formed by a sphingosine-base linking a carbon chain of 18 atoms and a saturated acyl-chain of 18-24 carbon atoms (...g. 1-1).

   The larger carbon-chain and the higher degree of saturation result in a higher transition temperature from the ordered gel phase to the liquid-crystalline phase of sphingolipids (sphingomyelin $T = 37^{\pm} \, \text{¡} \, 41^{\pm}C$) in comparison to phospholipids ($T < 0^{\pm}C$) [Schroeder et al., 1994; Brown, 1998]. Sphingolipids are potential donors and acceptors of hydrogen-bonds. Glycerophospholipids are only possible acceptors for hydrogen-bonds [Boggs, 1987]. Cholesterol is an almost planar molecule of four rings with one polar OH group which is in the membrane orientated towards the water surface. The OH group can act as a donor or acceptor for hydrogen-bonds. The ring structure of cholesterol also restricts the motion of neighboring lipids [Boggs, 1987].

   In model systems of sphingolipids and glycerophospholipids a phase separation was observed. Electron-spin resonance (ESR) and nuclear-magnetic resonance (NMR) spectroscopy have shown that cholesterol associates preferentially with the sphingolipids [Sankaram and Thompson, 1990]. Due to its ability to form hydrogen
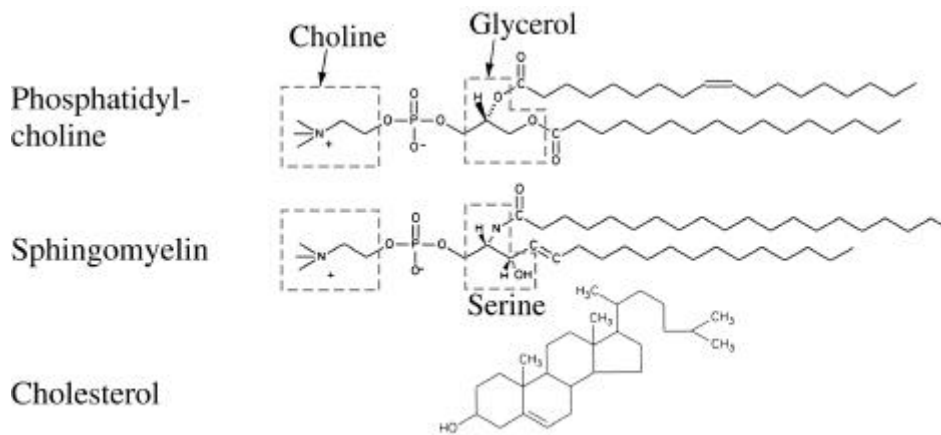
Figure 1-1: Examples for the three common lipid types in the plasma membrane: phosphatidylcholine (PC, a glycerophospholipid), sphingomyelin (SM, a sphingolipid) and cholesterol. The cis-double bond in the fatty acid chain of PC causes a kink in the chain. The molecules are aligned according to their hydrophobic parts which would be in the lipid bilayer (fatty acid and carbon chains for PC and SM and entire molecule except OH of cholesterol). The left of the molecules would be exposed to the water.

bonds cholesterol stabilizes the domains containing the sphingolipids (see ...g. 1-4) [Boggs, 1987]. Also biological membranes containing sphingolipids and glycerophospholipids are thought to partition into two phases [Vaz and Almeida, 1993; Brown and London, 1997]. A phase separation in two-dimensional systems occurs in form of many microdomains of one phase in the other phase to minimize the tension along the phase-borders [Vaz and Almeida, 1993].

Proteins are associated with the lipids mainly in two ways: directly by one or more hydrophobic domains in their amino acid sequence that traverse the lipid bilayer (transmembrane proteins) or indirectly by a lipid anchor (see ...g. 1-2). In addition to the hydrophobic domain transmembrane proteins may contain lipid modi...cations that also associates them to the lipid bilayer. The transmembrane proteins investigated in this work are the transferrin receptor (TrfR) and the in‡uenza virus hemagglutinin (HA) protein. HA which contains a lipid modi...cation in the cytoplasmic domain (as (1) in ...g.1-2), associates with sphingolipids via its transmembrane domain [Schei¤ele et al. 1996]. Most proteins using a lipid anchor utilize a structure called glycosylphosphatidylinositol(GPI)-anchor which inserts preferentially into sphingolipids [Schroeder et al., 1994]. The attached proteins are either exclusively exoplasmic, like the placental-alkaline phosphatase (PLAP) used in this work, or cytoplasmic, like various kinases. It was postulated that the preference of the GPI-linked proteins for the sphingolipid rich phase creates microdomains of these proteins and lipids which move raft-like in the remaining phospholipids and
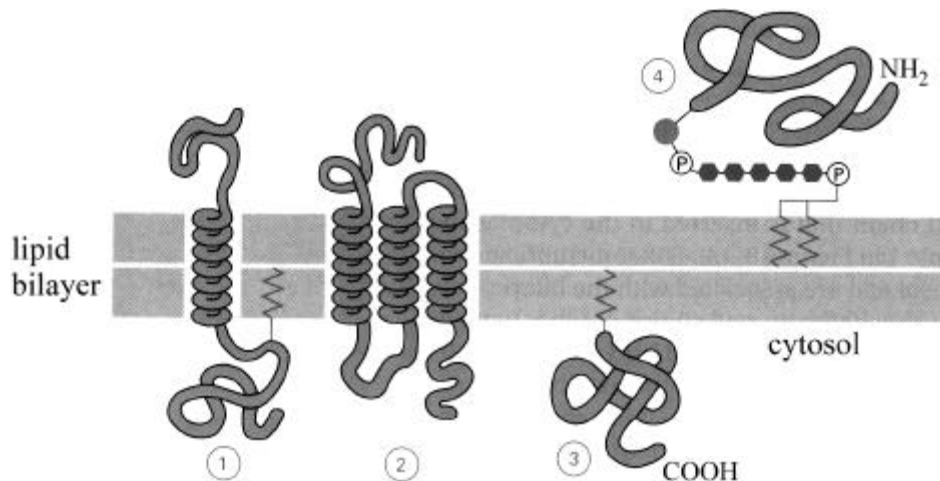
7

Figure 1-2: Various possible associations of membrane proteins to the lipid bilayer: Transmembrane proteins have one or more hydrophobic domains in their amino acid sequence that cross the membrane (1 and 2). They might have in addition a fatty chain or lipid covalently attached (1). Other proteins are just bound via attached lipids (3 and 4). The most common lipid anchor is the GPI-anchor (4).

proteins (see ...g. 1-4) [Simons and Ikonen, 1997].

All the proteins and lipids are synthesized centrally within the cell and have to be transported to the appropriate location.

Polarized cells contain membrane domains of distinct composition

In some cells, the composition of the membrane di¤ers between the two "poles" of the cell: they are polarized, e.g. epithelial and neuronal cells (...g. 1-3). Epithelial cells form a layer of cells, an epithelium, lining the walls of any lumen, e.g. in the intestine or kidney. The surface bordering the lumen is called apical membrane. The remaining cell surface is the baso-lateral membrane. Lipid and protein distributions di¤er widely: the apical membrane is enriched in sphingolipids and GPI-anchored proteins [Simons and van Meer, 1988; Keller and Simons, 1997]. In an epithelium the individual cells are connected by tight junctions. These tight junctions are protein structures that form a barrier to the lateral di¤usion in the outer lea‡et of the plasma membrane bilayer.

Neuronal cells are another cell type with a polarized membrane protein distribution. Mature neuronal cells have several processes to receive signals, the dendrites, a cell body, the soma, and one process to send signals, the axon. The axonal membrane's protein composition is distinct from the somato-dendritic membrane. The analogy to epithelial cells is drawn by comparing the axonal membrane to the apical one and the somato-dendritic to the baso-lateral membrane [Dotti and Simons, 1990; Dotti et al., 1991].
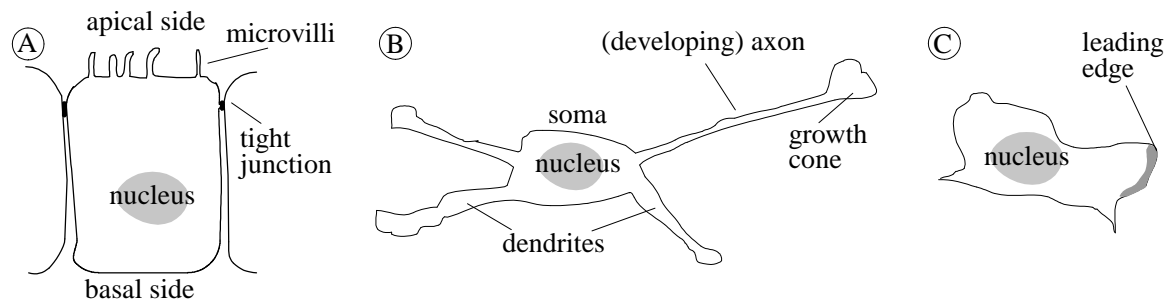
8

Figure 1-3: Some of the cell types that exhibit uneven membrane protein distribution: (A) epithelial cells grow polarized in a monolayer; (B) neuronal cells have an axonal membrane composition that di¤ers from the composition of the somato-dendritic membrane; (C) migrating ...broblasts express a special sub-set of membrane proteins in the leading edge.

Hippocampal neurons are well suited to study the development of polarization because they can be plated unpolarized into culture and maintained and studied during the development. In culture the cells can be observed and manipulated in the light microscope. Studies with ‡uorescently labelled vesicles from the Golgi have shown that newly synthesized membrane is transported speci...cally to the growth cones [Craig and Banker, 1995]. The development of the neurons from round cells to polarized neurons takes about two weeks. Only in the ...nal stage after 11-14days in culture, is the speci...c membrane protein distribution established. However it is not clear what structure could provide a di¤usion barrier separating the two domains because it has been reported the di¤usion of some proteins is hindered while lipid labels can pass freely [Kobayashi et al., 1992; Winkler and Poo, 1996].

An uneven distribution of some surface molecules has also been observed in ...broblasts: the leading edge of a crawling ...broblast contains mainly proteins, that would be sorted baso-laterally in epithelial cells [Bretscher, 1996]. Also, in these cells the structure that separates the two domains has not been determined.

Assembly of the membrane components and their dynamics

The most common method to achieve a polar distribution of membrane constituents is the targeted delivery of the membrane constituents inside the cell (sorting). In epithelial cells, most membrane proteins are selectively transported to speci...c membrane areas: the GPI-anchored proteins, e.g. PLAP, and HA are among the proteins that are localized on the apical side, while for example, the vesicular stomatitis virus glycoprotein (VSV-G) is found exclusively in the baso-lateral membrane [Rindler et al., 1984; Mellman et al., 1993]. The lipids are also targeted, i.e. sphingolipids are delivered speci...cally to the apical membrane [Simons and van Meer, 1988; van Meer et al., 1987]. The polarized distribution of membrane proteins

9

in hippocampal neurons is also achieved by sorted delivery [Ledesma et al., 1998].

The observation of the large variety of lipids present in the cell membrane and their unevenly distribution, together with the knowledge about the phase separation of sphingolipids and glycerophospholipids, has led to the hypothesis that glycosphingolipid-microdomains structure the cellular membrane dynamically [Simons and Ikonen, 1997] (see ...gure 1-4). Strong lateral interaction between sphingolipids and cholesterol is thought to initiate the formation of microdomains or "rafts". Due to the richness in long saturated fatty-acid chains these rafts would separate from the normal lipids and mediate sorting of lipids and associated proteins as early as in the Golgi [Brown and Rose,1992; Parton and Simons, 1995; Simons and Ikonen, 1997]. Recently, evidence for microdomains in the membrane bilayer has accumulated. Applying the detergent Triton-X100 leaves complexes of sphingolipids, sphingomyelin, cholesterol and certain proteins as detergent-insoluble groups (DIG) [Brown and Rose, 1992]. Some of the proteins found together with DIGs are the glycosylphosphatidylinositol(GPI)-anchored proteins and the in‡uenza virus hemagglutinin (HA) [Schei¤ele et al., 1997]. In epithelia, most of the apically sorted proteins will concentrate in DIGs. Several studies have focused on the fate of these microdomains upon arrival in the plasma membrane. Using two antibodies, Harder et al. [1998] have cross-linked di¤using membrane proteins on the surface of intact ...broblasts to show that GPI-anchored proteins are part of percolating microdomains. GPI-anchored proteins formed larger, percolating clusters that excluded other membrane proteins, while the cross-linking of a non-raft protein resulted in an homogenous labelling of the cell surface. Using ‡uorescent resonant energy transfer (FRET) Varma and Mayor [1998] have shown that a GPI-anchored folate-receptor isoform is clustered in domains smaller than 70nm. The degree of energy transfer for a ‡uorescent analogue of folic acid bound to a GPI-anchored folate-receptor isoform, a measure for the intermolecular distance, was found to be independent
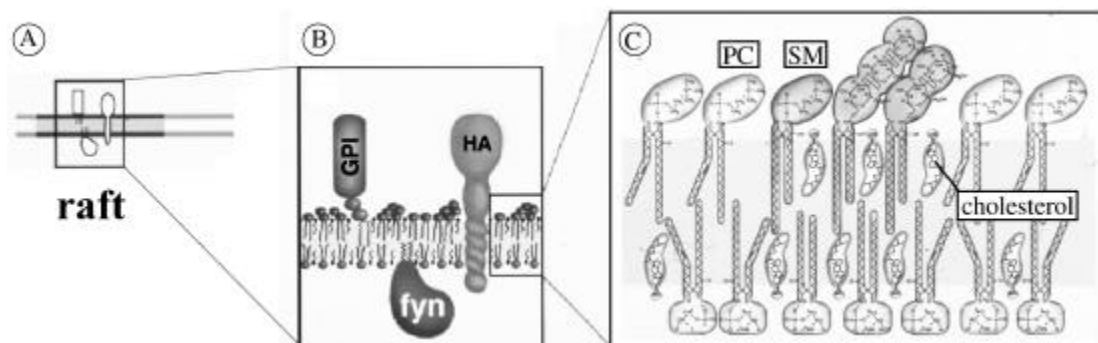

Figure 1-4: (A) Model of the lipid raft as microdomain in the membrane; (B) zoom depicting the associated proteins; (C) further zoom showing the role of the involved lipids (PC, SM and cholesterol) [after Simons and Ikonen, 1997].

of the density of proteins on the surface. Friedrichson and Kurzchalia [1998] have used a 11.4Å-long chemical linker to cross-link another GPI-anchored protein. They conclude that domains of at least 15 molecules exist in the membranes of intact cells.

In addition to its intrinsic structure, the lipid bilayer with the membrane proteins is structured further by the supporting membrane skeleton on the inside of the cell and the extracellular glycocalyx. Their relative dominance and coupling varies largely between cell types, and during the life time of a single cell.

It has been shown by single-particle tracking (SPT) that the membrane skeleton can influence the diffusion of transmembrane proteins within the membrane bilayer. For SPT, a membrane component is specifically labeled with an antibody attached to a colloid gold particle or a fluorescent polystyrene sphere. The trajectory of the particle is tracked by video-microscopy [Gelles et al. 1998; Jacobson et al., 1987]. The motion may be unrestricted, or transiently confined to areas of a few hundred nanometers diameter [Kusumi et al., 1993; Sako and Kusumi, 1994]. Transient confinement results in a "hopping diffusion": local free diffusion followed by a jump into a neighboring area. Kusumi proposed the membrane-skeleton fence model as explanation: a filamentous network with meshsize of 300 to 600 nm in diameter lying closely underneath the membrane bilayer. The degree of confinement of a transmembrane protein to such a mesh depends on the size of its cytoplasmic domain.

The outer glycocalyx consists of carbohydrates bound to lipids and proteins. Very little about its role in membrane structure and dynamics is known so far.

1.3   Aim and summary of this study

In this work established and newly developed physical methods were used to further elucidate the structure and dynamics of the outer cellular membrane - the plasma membrane. Starting point were two techniques developed in the past decade: scanning force microscopy (SFM) and single-particle tracking (SPT). SFM provides high resolution images of the topography of surfaces, and mechanical information of the underlying structure. If the compliance of the probe is matched to the one of the sample, macromolecular resolution has been achieved on solid supports. In SPT the movement of a molecule in the membrane can be analyzed by labelling it with a polystyrene sphere or a colloid gold particle and tracking the movement of the particle-molecule complex. This yields information on the overall dynamics of the membrane and the mobility of individual membrane proteins.

To investigate the exchange and barriers between macrodomains in the plasma membrane, SPT of the motion of the GPI-anchored protein Thy1.1., the transmembrane protein TrfR and the ganglioside lipid GM_1 was performed in developing hippocampal neurons. In young unpolarized cells it was observed that GM_1 ‡owed retrogradely onto the cell body with speeds of 15 ¡ 35¹m=min. Later, in maturing cells the motion of spheres onto the cell body ceased, however often a reduced ‡ow within the neurite remained. Furthermore, using the molecule Thy1.1 several di¤usion barriers were observed on the major neurite. However, due to the limitations of SPT to two dimensions and the high vertical extend of the hippocampal neurons in culture, the existence of the proposed di¤usion barrier at the base of the axon could not be demonstrated.

The association of the membrane bilayer to the membrane skeleton was investigated by tethering the membrane. In neurons, tethers were readily formed. The force required to extract a tether was lowest at the growth cone. Once formed, tethers were easily moved over the cell surface. In other cell types, such as acinar cells and hepatocytes, membrane tethers could only be extracted after depolymerization of the actin skeleton.

SFM was applied to depict a ...ner image of the plasma membrane and the underlying membrane skeleton of epithelial and neuronal cells at high topographic and mechanical resolution. On the apical membrane of living epithelial cells, a network of submembrane ...laments was resolved. On ...xed cells, the membrane with the microvilli, long thin cellular protrusions could be imaged. But, often high lateral resolution was not achievable due to a dense glycocalyx. In images of growth cones of hippocampal neurons, bundles of ...laments were visible but no detailed membrane structure. In this mechanical SFM the cantilever exerted relatively large forces of about 0:1nN onto the membrane. This caused the extracellular structures and the bilayer to collapse on the membrane skeleton. In addition, on villous surfaces the resolution is limited by the pyramidal shape of the probe and the large mechanical lever arm: the angle of the pyramid determines the maximal steepness of a surface, that can be resolved, and the viscous drag of the mechanical lever reduces the

maximal speed of force control.

The limitations of the force sensor of the SFM are overcome by the scanning photonic force microscope (SPFM), which is a newly developed scanning force microscope without mechanical lever. In the SPFM a polystyrene sphere trapped in a gradient laser trap is scanned as probe over the surface. The contact forces are adjustable and can be as low as 0.1pN and up to 100pN, complementing the mechanical SFM in the low force range. The fluorophore filled sphere with 100nm radius is held near the Gaussian focus in a laser beam by gradient forces. The fluorophores inside the sphere are excited via two-photon absorption by the trapping laser. The deflection from the resting position is measured by the associated change in fluorescence intensity. The spring constant of the "bead light-beam cantilever" depends on the laser intensity and the size of the sphere. It was mostly adjusted to be $0.5 - 1 \mu N/m$ along the optical axis and $3 - 5 \mu N/m$ laterally. The use of the light beam and the replacement of the mechanical cantilever by a spherical probe allow the imaging of arbitrary three-dimensional samples as long as they are transparent to the infra-red laser light. At such low contact force of about 0.1pN the plasma membrane of fibroblasts and neurons appeared smooth. No elasticity could be measured, indicating that, in contrast to the SFM, the membrane was not indented between the cytoskeletal support and the lipid bilayer was imaged. With the SPFM images of the vertical sides of neurites and the steep slopes of fibroblasts at their nucleus, rising more than 10 micrometers within a few hundred nanometers, were obtained.

Because of the small spring constant of the "bead light-beam cantilever" in the SPFM, the thermal position fluctuations become substantial. For a spring constant of $0.5 \mu N/m$ the fluctuations of the probe are about 90nm at room temperature so that force measurements requiring precise positioning become impossible. By adding a fast three-dimensional sensor for the position of the sphere within the laser trap, we developed the photonic force microscope (PFM), that exploits the thermal position fluctuations to probe the surrounding three-dimensional potentials. Due to the nanometer spatial resolution of the detector at 50kHz bandwidth, the "scanning speed" of the probe is only limited by the autocorrelation time of the movement of the probe, which depends on the potential trapping the probe and the viscous drag. The PFM was applied to measure the reduced diffusion of small particles near surfaces. Using the thermal position noise as probe, the lateral elasticity of the lipid bilayer of the plasma membrane of fibroblasts was measured to be $5 \mu N/m$, underlining the problems observed in the imaging studies using SFM.

By coating the fluorospheres with ligands for specific membrane receptors the PFM was extended to measure the interaction of individual molecules with the environment. Because the three-dimensional analysis of the thermal position fluctuations of the sphere in the PFM has nanometer and microsecond precision, the direct interaction an individual membrane component with its environment became possible. For the first time, parameters such as the interaction potential with other membrane components, local confinements and the local diffusion coefficient, be-

came accessible at the nanometer scale. The diffusion coefficient is related to the size of the diffusing molecule. The local diffusion measurements performed in this thesis proved the existence of glycosphingolipid microdomains ("lipid rafts") in the plasma membrane of living, untreated cells. They also provided the first estimates of their size and temporal stability:

BHK cells were transfected with the GPI-anchored protein placental-alkaline phosphatase (PLAP) and the transmembrane proteins influenza virus hemagglutinin (HA) and the transferrin receptor (TrfR). It is known that the first two associate with the lipid raft domains, while the later one does not. In untreated cells the additional viscous drag on a sphere binding to the TrfR was $1.6 \cdot 10^{-9}\,Pa\,s\,m$, while the raft-associated proteins added about twice as much drag. After cholesterol depletion of the cells, the viscous drag of PLAP decreased to the values lower than TrfR, while the measurement for the TrfR was unchanged. These results demonstrate the existence of lipid microdomains in the plasma membrane of living cells. The domains appear to be stabilized by cholesterol, and to diffuse as one entity over several micrometers on the cellular surface for minutes. Clustering PLAP domains by multivalent spheres, resulted in immobilization of the spheres, indicating binding to the actin cytoskeleton. An event that is expected to happen in the signalling pathway in which the rafts are thought to be involved. Using the measured viscous drags and applying the Saffman-Delbrück theory of protein diffusion in a lipid bilayer, a membrane viscosity of $0.16\,Pa\,s$ and radius of about 26nm for the lipid-microdomains was determined.

Part II

Theory of thermal motion

Theory of thermal motion

This chapter deals with the theory of the intrinsic thermal ‡uctuations in a medium at non-zero temperature. So far, it has been impossible to follow the thermal ‡uctuations of individual molecules in the medium directly at molecular resolution. But an object or unit large enough to average over some of the molecular ‡uctuations, still displays thermal ‡uctuations. Two examples are: the ‡uctuations of a microscopic particle immersed in a water bath and the ‡uctuations of the voltage measured across a resistor due to the thermal motion of the electrons. The observation of the former by Brown has led to the term Brownian motion. The interest in the latter, gave rise to a series of articles in the forties [Chandrasekhar, 1943; Uhlenbeck and Ornstein, 1944 ; Wang and Uhlenbeck, 1945]. The discussion of the Brownian motion in this chapter is based on those publications and the textbook from Reif [1965].

Some general terms of statistical physics are summarized in the introduction. Section 2 describes the motion of a free (sect.2.0.1) and a trapped (sect.2.0.2) Brownian particle based on the equation of motion, the Langevin equation (eq.2.1). To simplify the solution the description is limited to the one-dimensional case far from any boundaries. The e¤ects of close proximity to a surface on the Brownian motion are discussed in sect.2.1.1. Section 2.2 concentrates then on the two-dimensional di¤usion in a lipid bilayer: the Sa¤man-Delbrück theory of protein di¤usion (sect.2.2.1), and the di¤usion of a tracer coupled to a membrane protein (sect.2.2.1). The chapter closes with a discussion on the statistics of a random walk (sect.2.3) and a summary of the results (sect.2.4).

Statistical terms and tools

The following essentials of statistical physics [Reif, 1965] will be used:

- The **equipartition theorem** of classical statistical mechanics states that the mean value of each independent quadratic term in the energy is equal to $\frac{1}{2}k_BT$.

- A statistical process is characterized by the probability distribution w(s) leading from the current position r(t) to the one s-steps ahead: $r(t+s) = w(s)r(t)$. In a **Gaussian process** the w(s) are independent for each step and w(s) falls o¤ rapidly as jsj ! 1 . A **random-walk** is often used as introductory example to a Gaussian processes. A particle undergoing a one-dimensional random walk has at each time point in the one-dimensional case the same probability to do one step of de...ned length in the positive or the negative direction.

- If the number of steps N is su¢ciently large, the probability distribution of any variable r of a Gaussian process is distributed according to the **Gaussian distribution**:

$$P(r) = \boxed{P}\frac{1}{2\frac{1}{4}\frac{3}{4}^2}\exp\left[\, \text{i}\,\frac{(r \text{ i } \mathring{r})^2}{2\frac{3}{4}^2}\,\right]\,; \tag{1.1}$$

where $\mathring{r}$ is the mean of the distribution and ¾ the root-mean-square deviation from $\mathring{r}$. This is the content of the so-called "central limit theorem".

- One special Gaussian process is the **Marko¤ process** in which the probability for a variable to be in a speci...c range depends only on its value a short time before. Free Brownian motion is a Marko¤ process because the motion depends only at the momentum r a very short time before. Because the position r at time t_1 of a Brownian particle in a potential depends on $r(t_0)$ and $r(t_0)$ this is not a Marko¤ process anymore. To solve such a problem, it can often be projected onto two Marko¤ processes with two independent variables. In our example, the time scale on which the particle depends on r is so much shorter than the one on which it depends on r(t) that the separation can be done via the time-scale selected (see sect. 2.0.2).

- The **autocorrelation function** C(s) of a function r(t) is de...ned as

$$C(s) = \frac{\hbar r(t)r(t+s)\text{i}}{\hbar r^2\text{i}} \tag{1.2}$$

with $\hbar r^2\text{i} = \int^{R} r^2(t)dt$. It provides a measure for the speed with which the probability w(s) falls o¤ as jsj ! 1 :

- The relationship between **spectral and spatial analysis** can be summarized in the fact that the normalized correlation function (eq. 1.2) with r(t) =

$\int_{-\infty}^{+\infty} A(\omega)e^{i\omega t}d\omega$ and the normalized spectrum

$$S(\omega) = \frac{G(\omega)}{\int_0^\infty G(\omega)d\omega} \text{ with } G(\omega) = \lim_{T\to\infty} \frac{2}{T}|A(\omega)|^2 \tag{1.3}$$

are each other's Fourier cosine transform.

Diffusion and diffusion coefficient

The concept of diffusion and the diffusion coefficient are classically defined for *self-diffusion*, i.e. solvent and diffusing molecules are identical, but the latter constitute only a small number of labeled molecules which are unevenly distributed. Then, diffusion is driven by the concentration gradient and the diffusion coefficient D is the proportionality factor between the flux J_r, which is the flow of molecules through an area in direction of r, and the concentration gradient of labeled molecules: $J_r = -D\frac{\partial n}{\partial r}$. The diffusion equation

$$\frac{\partial n}{\partial t} = -\frac{\partial J_r}{\partial r} = D\frac{\partial n^2}{\partial r^2} \tag{1.4}$$

relates the change of number n of labeled molecules in a volume with time t to the flux J_r. A single particle with diffusion coefficient D moving randomly in one-dimension will be found after time t in the interval [Reif, 1965]

$$\left\langle r^2(t) \right\rangle = 2Dt, \tag{1.5}$$

and moving in a plane, it will be found after time t in the area

$$\left\langle r^2(t) \right\rangle = 4Dt. \tag{1.6}$$

This mean-square displacement of the particle $\left\langle r^2(t) \right\rangle$ of the positions $r(t)$ is measured in a single-particle tracking experiment to determine the diffusion coefficient D (see chap.3.2 on SPT at p. 29).

Chapter 2

Theory of Brownian motion

2.0.1 Free Brownian particle: continuum theory (1D)

For particles diffusing in a medium consisting of different, smaller solvent molecules, the medium can be treated as continuum. In the *continuum theory* motion is driven by random fluctuations from the solvent molecules and resisted by the frictional forces of the viscous solvent. The equation of motion of a freely diffusing particle outside of any potential as function of its position $r(t)$ is:

$$m\ddot{r} + \gamma\dot{r} = F(t) \ , \tag{2.1}$$

with the viscous drag γ, a particle mass m, $\dot{r} = \frac{dr}{dt}$ and a stochastically fluctuating, uncorrelated thermal force $F(t)$ with a disappearing time-average $\langle F(t) \rangle = 0$. Eq. (2.1) is called *"Langevin equation"*. The stochastically fluctuating thermal force $F(t)$ can be written as

$$\langle F(t)\, F(t') \rangle = 2\gamma k_B T\, \delta\,(t - t') \ , \tag{2.2}$$

because the thermal force is proportional to the thermal energy $k_B T$ and uncorrelated on accessible time-scales. Reif [1965] estimates the correlation time of $F(t)$ to be on the order of 10^{-13} *sec.* in a typical liquid, because it is determined by the ratio of the mean solvent particle separation and speed. Multiplying eq.(2.1) with r, and rewriting $r\frac{d\dot{r}}{dt}$ as $\frac{d}{dt}\left(r\dot{r}\right) - \dot{r}^2$, results in

$$m\left(\frac{d}{dt}\left(r\dot{r}\right) - \dot{r}^2\right) + \gamma r\dot{r} = rF\,(t)\,. \tag{2.3}$$

Applying the *"equipartition theorem"* $\left(\frac{1}{2}m\,\langle\dot{r}^2\rangle = \frac{1}{2}k_B T,\ \text{see p.16}\right)$ the resulting differential equation is

$$\frac{k_B T}{\gamma} = \frac{1}{2}\frac{d}{dt}\,\langle r^2 \rangle + \frac{m}{\gamma}\frac{d}{dt}\left(\frac{1}{2}\frac{d}{dt}\,\langle r^2 \rangle\right)\,. \tag{2.4}$$

The solution of eq. (2.4) is

$$\frac{1}{2}\frac{d}{dt}\left\langle r^2 \right\rangle = \frac{k_B T}{\gamma} + C \exp\left(-\frac{\gamma}{m}t\right) , \qquad (2.5)$$

where C is the integration constant with $C = -\frac{k_B T}{\gamma}$ for the starting condition $r(t = 0) = 0$. The integration over time yields as solution of eq. (2.1) for the mean-square displacement $\langle r^2 \rangle$:

$$\left\langle r^2 \right\rangle = 2k_B T \frac{m}{\gamma}\left[t - \frac{m}{\gamma}\left(1 - \exp\left(-\frac{\gamma}{m}t\right)\right)\right] . \qquad (2.6)$$

The quality of the motion observed is characterized by the time-scale on which it is examined. The resulting mean-square displacement $\langle r^2 \rangle$ in eq.(2.6) in the limits of extremely short or long times is:

$$t \ll \frac{m}{\gamma} \quad : \quad \left\langle r^2 \right\rangle = \frac{k_B T}{m}t^2 \qquad \text{free particle} \qquad (2.7a)$$

$$t \gg \frac{m}{\gamma} \quad : \quad \left\langle r^2 \right\rangle = \frac{2k_B T}{\gamma}t \qquad \text{diffusion} \qquad (2.7b)$$

So, for times t shorter than the *"momentum-autocorrelation time"* $\tau_m = \frac{m}{\gamma}$ the movement is dominated by the momentum of the particle and it moves essentially freely. On time-scales much longer, the particle diffuses randomly. Relating the result for free diffusion to the self-diffusion of a particle in a plain eq.(1.5) yields the Einstein-relation:

$$D = \frac{k_B T}{\gamma}. \qquad (2.8)$$

In water at $20^0 C$ (viscosity $\eta = 10^{-3} Pa\,s$) polystyrene spheres ($\rho = 1.06\,g/cm^3$) of radius $a = 0.5\mu m$ are slowed down by the Stokes viscous drag $\gamma = 6\pi\eta a$, resulting in a momentum-correlation time $\tau_m = \frac{m}{\gamma} = 0.12\ \mu s$. To observe this momentum-correlation a temporal resolution of $0.1\ \mu s$ would be necessary. Then the spatial resolution would not suffice, because a particle with $D \sim 10^{-10}\frac{cm^2}{s}$ would diffuse only in an area of about 10 Å^2 during this time. So the spheres observed do not behave as free particles but diffuse randomly with the diffusion coefficient $D = \frac{k_B T}{\gamma}$. The temporal resolution achieved in this study was 15 μs (chap.8).

2.0.2 Brownian particle in a harmonic potential (1D)

The motion of a Brownian particle trapped in a harmonic potential (chap.8) with spring constant κ through a viscous liquid, is described by:

$$\gamma\dot{r} + \kappa r = F\left(t\right) . \qquad (2.9)$$

20

Inertial forces are ignored because they have an effect only during the inaccessible time-scale of a quasi-free particle ($t \gg \frac{m}{\gamma} = 0.12\,\mu s$ for a $1\,\mu m$-diameter sphere, see above). $F(t)$ represents again the random force of the solvent acting on the particle. The differential equation (2.9) is solved by an exponential function:

$$r(t) = r(0)\exp\left(-\frac{\gamma}{\kappa}t\right) \tag{2.10}$$

To characterize the motion the exponentially decaying position autocorrelation function is computed:

$$\langle r(0) \cdot r(t)\rangle = \overline{r^2}\exp\left(-\frac{\gamma}{\kappa}t\right) = \overline{r^2}\exp\left(-\frac{t}{\tau}\right); \tag{2.11}$$

with the correlation time $\tau = \frac{\gamma}{\kappa}$ and the mean square amplitude $\overline{r^2} = \frac{k_B T}{\kappa}$ due to the equipartition theorem. Therefore, measuring the autocorrelation-time τ and the trap stiffness κ provides a way to determine the local viscous drag γ and the diffusion coefficient $D = \frac{k_B T}{\gamma}$ of a sphere in a harmonic potential (see section 8 on p.60).

2.0.3 Position distribution profiles the potential (1D)

The thermal position fluctuations in a potential are Boltzmann distributed [Reif, 1965]. The probability $P(r)$ to find a thermally excited particle in a potential $V(r)$ in the interval $[r; r + dr]$ is

$$P(r)\,dr = c \cdot \exp\left(-\frac{V(r)}{k_B T}\right) dr\,, \qquad c \text{ chosen to normalize} \int_0^1 P(r)dr = 1: \tag{2.12}$$

The trapping potential can be determined by measuring the position distribution [Florin et al., 1998]:

$$V(r) = -k_B T\,\ln P(r) + k_B T\,\ln c;$$

where c is a potential offset that can neglected.

2.1 Special effects of 3D-Brownian motion

For a Brownian particle moving in the bulk solution in an isotropic environment the three dimensions are independent and identical. The viscous drag γ of a non-compressible isotropic fluid with viscosity η and density ρ at pressure p and an external force F in a velocity field $u(r; t)$ is described by the Navier-Stokes equation:

$$\rho\frac{Du}{Dt} = \rho\left(\frac{\partial u}{\partial t} + (u \cdot \nabla)u\right) = -\nabla p + \eta\nabla^2 u + \rho F: \tag{2.13}$$

Again, the fluid is approximated as continuum, because the scales are much larger than the free path of the liquid molecules. The solution of eq.(2.13) depends on the boundary conditions.

For a slowly moving sphere of radius a far away from any surfaces the solution is the Stokes drag:

$$\gamma = 6\pi\eta a. \tag{2.14}$$

If the fluid is not isotropic because the proximity to a solid surface imposes non-slip boundary conditions, the diffusion is influenced. The special case of a sphere near a planar surface will be discussed next.

2.1.1 Confined Brownian motion near a surface

A partial confinement on a length scale in the order of a sphere's radius results in a increase of the viscous drag. In 1965, Brenner derived formulas for this increase of viscous drag parallel and orthogonal to a flat surface. The correction up to 3rd-order in $\left(\frac{a}{a+z}\right)$ to the viscous drag for a sphere with radius a moving towards a plane is

$$\frac{\gamma_{\perp(z=1)}}{\gamma_{\perp(z)}} = 1 - \frac{9}{8}\left(\frac{a}{a+z}\right) + \frac{1}{2}\left(\frac{a}{a+z}\right)^3; \tag{2.15}$$

where z is the distance between the surface of the sphere and the surface. For movements parallel along a surface the correction up to 5th-order in $\left(\frac{a}{a+z}\right)$ is

$$\frac{\gamma_{\parallel(z=1)}}{\gamma_{\parallel(z)}} = 1 - \frac{9}{16}\left(\frac{a}{a+z}\right) + \frac{1}{8}\left(\frac{a}{a+z}\right)^3 - \frac{45}{256}\left(\frac{a}{a+z}\right)^4 - \frac{1}{16}\left(\frac{a}{a+z}\right)^5. \tag{2.16}$$

This effect has to be taken into account when using spheres as markers for proteins diffusing in a membrane. In section 8 on page 59 the method of thermal noise analysis is applied to measure D as function of the distance z confirming Brenner's result.

2.2 2-dimensional diffusion in lipid bilayers

Following the treatment by Nir and Stein [1971] proposing two modes of diffusion in liquids, the diffusive behavior in bilayers can be also divided into two regimes based on the ratio of the size of the diffusing object to the size of the solvent, i.e. the lipids in the bilayer. The motion of molecules comparable in size to the host phospholipids is described by the free area lattice theory modeling the motion as hopping into a free place. The diffusion of objects large enough, so that the surrounding lipid solvent can be treated as continuum, is described by the continuum theory [Vaz et al., 1984; Saffman, 1975). It is not yet clear how to describe the transition regime of both theories which in lipid bilayers comprises particles with radii of about 0.5nm. The transmembrane proteins and glycosphingolipid rafts studied here are large enough

to be described by the continuum theory [Vaz, 1984].

2.2.1   Sa¤man-Delbrück theory

The continuum treatment from the three dimensional problem was extended by Sa¤man and Delbrück [1975] to di¤usion in thin viscous sheets. The Navier-Stokes equation (eq.2.13) has no solution for a steady translational motion in two dimensions. A ...nite translational mobility $°_i{}^{-1}$ can be obtained by including the inertia of the viscous ‡uid [Lamb, 1932 in Sa¤man and Delbrück, 1975]. The viscous drag on a cylindrical particle with radius r and height h is given by

$$°_i{}^{-1} = \frac{1}{4¼´_m h}\left[\ln\frac{4´_m}{½ur} + \frac{1}{2} \text{ i } ¯\right]; \qquad (2.17)$$

where ½ denotes the density of the ‡uid, u the translational velocity, ¯ the Euler's constant (0:5772) and h the membrane thickness [Sa¤man and Delbrück, 1975]. This description is not independent of velocity and force, so it is not suitable for the Einstein relation (eq.2.8). Therefore, Sa¤man and Delbrück have derived a force-independent form for the special case of di¤usion in a lipid bilayer. In this case the velocity ...eld inside the bilayer is exactly two-dimensional because lipids do not permit shear across the membrane. A no-slip boundary condition is imposed on the surrounding medium, which has to have a ...nite viscosity $´_w$. Then, the di¤usion coe¢cient for a cylindrical particle in a homogenous bilayer becomes [Sa¤man and Delbrück, 1975]:

$$D = \frac{k_B T}{4¼´_m h}\left[\ln\frac{´_m h}{´_w r} \text{ i } 0{:}5772\right]: \qquad (2.18)$$

This approximation is valid for $´_m \text{ À } ´_w$, which is ful...lled for cellular membranes [Peters and Cherry, 1982] . For other ratios of the viscosities Hughes et al. have obtained an exact expression [Hughes, 1981]. The Sa¤man-Delbrück relation (Eq.(2.18)) predicts a weak dependence of the lateral di¤usion coe¢cient D on the radius r. Peters and Cherry [1982] have shown that the Sa¤man-Delbrück relation predicts the di¤usion for bacteriorhodopsin (r = 4:3 § 0:5nm) in arti...cial dimyristolphosphatidylcholine (DMPC) vesicles correctly (for a discussion of di¤usion coe¢cients see section 13.4 on p.106).

Di¤usion of a sphere tracking a membrane protein

In single-particle tracking and local di¤usion measurements by thermal noise analysis, a sphere bound to a membrane component was observed. Thus the viscous drag $°$ in the Langevin equation (2.1) contains a viscous drag component stemming from the sphere $°_s$ in addition to the $°_p$ from the di¤using membrane protein. So the damping $°$ in the equation of motion (2.9) is the sum of $°_s$ and $®°_p$, where $® \text{ 2 } [0; 1]$ represents the coupling strength between membrane protein and sphere.

The di¤usion coe¢cient is then given by

$$D = \frac{k_B T}{°_s + ®°_p} \qquad \text{with} \qquad °_s = 6¼´_w rc ; \qquad (2.19a)$$

$$\text{and} \qquad °_p = \frac{4¼´_m h}{\ln \frac{´_m h}{´_w r} ¡ 0{:}5772} : \qquad (2.19b)$$

The damping $°_s$ of the sphere is corrected by the factor c because of the proximity to the plasma membrane induces additional viscous drag (see section 2.1.1 above).

2.3 Statistics of a random walk

The **probability distribution of the positions** that a particle in a harmonic trap reaches is a Gaussian distribution (section "Statistical terms and tools" on p.16). If a certain displacement has been measured N times, the error in this probability is $\frac{1}{\sqrt{N}}$, if the N measurements are independent. Acquiring more measurements within the autocorrelation time of the process does not increase the information. If n measurements of a process with autocorrelation time $¿ = ® dt$ are taken with a temporal resolution of dt, then the number of independent measurements is only $N = n{=}®$.

The **reliability of the autocorrelation function** can be estimated using a method developed by Bartlett [1946] and summarized by Box and Jenkins [1976]. To assess the standard error of the estimated coe¢cients r_k of the autocorrelation the variance of estimated (r_k) to theoretical $(½_k)$ coe¢cients is calculated. Let $½_k$ be the value of an autocorrelation function at time-lag k and $½_k = Á^{jkj}$ ($¡ 1 < Á < 1$), i.e. the function decays exponentially:
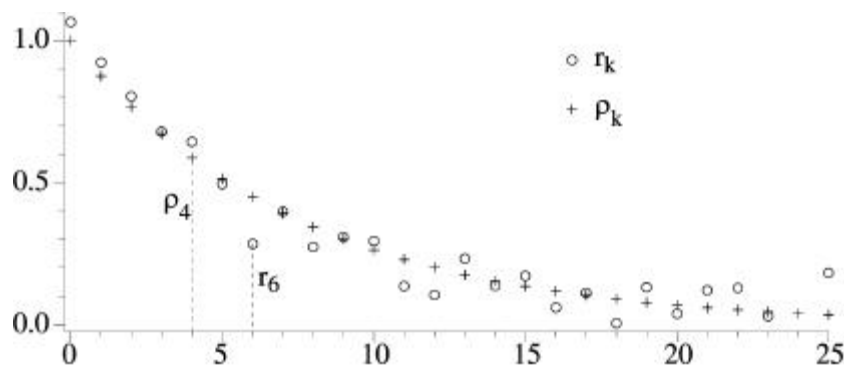
Then the standard error of the autocorrelation estimate r_k as an approximation of $½_k$ is

$$\text{var} [r_{k+1}] ' \frac{1}{N} \left[\frac{(1 + Á^2) \left(1 ¡ Á^{2k} \right)}{1 ¡ Á^2} ¡ 2Á^{2k} \right] ; \qquad (2.20)$$

where N is the number of independent points. The variance of the ...rst coe¢cient is

$$\mathrm{var}\,[r_1] \simeq \frac{1}{N}\left(1 - Á^2\right); \tag{2.21}$$

and in the limit for large k the variance is:

$$\lim_{k!\,1}\mathrm{var}\,[r_k] \simeq \frac{1}{N}\left(\frac{1 + Á^2}{1 - Á^2}\right): \tag{2.22}$$

In the case of a $0:5\,\mu$m-diameter sphere in a laser trap potential of $1:6 \cdot 10^{-5}\frac{N}{m}$ a $Á = 0:92$ has been measured [Pralle et al., 1997; sect.8], so that $\mathrm{var}\,[r_1] \simeq (6:5\,N)^{-1}$ and $\lim_{k!\,1}\mathrm{var}\,[r_k] \simeq 12=N$. Thus, in this case the standard errors were $\frac{3}{4}_1 = (6:5\,N)^{-1=2}$ and $\lim_{k!\,1}\frac{3}{4}_k = 3:5=\sqrt{N}$. To achieve di¤usion coe¢cient measurements with an error smaller than 10% also for large time-lags k the observation interval $¢t$ has to be about 1200 times longer than the autocorrelation-time $¿$, in this example $¢t \,¸\, 0:24$ s.

Therefore the temporal resolution of the viscosity measurement is limited by the spheres motion and not by the bandwidth of the position detection. For reliable di¤usion coe¢cient measurements the observation interval $¢t$ has to be about three orders of magnitude longer than the correlation-time $¿$.

2.4   Summary and discussion

Summarizing this theory section, the following results are important for (localized) di¤usion measurements of membrane proteins:

- The spring constant k of a harmonic trapping potential can be measured directly from the position distribution.

- The viscous drag $°$ on a Brownian particle in a trapping potential is determined as $° = k¿$, with $¿$ being the position autocorrelation time.

- The viscous drag $°_s$ of a sphere near a surface is increased according to the formula of Brenner (eq. (2.16)).

- The viscous drag $°_p$ on a membrane protein is described by the Sa¤man-Delbrück eq. (2.19b).

- To achieve di¤usion coe¢cient measurements with an error smaller than 10% the observation interval $¢t$ has to be about 1200 times longer than the autocorrelation time $¿$:

Further, the following assumptions were made, that were con...rmed by the experiments (chap.13):

- It was assumed that the measured drag of a sphere bound to a membrane protein would be the sum of the drag on the sphere and the drag on the membrane protein: $\gamma_s + \gamma_p$, i. e. the coupling of the protein damping γ_p to the sphere was rigid ($\alpha = 1$ in eq.(2.19a)). The following is a scaled drawing of the experimental situation:
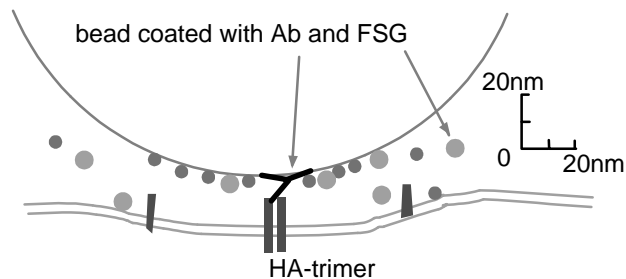
The linker between the sphere and the membrane protein was relatively short ($l \gg 10nm$) and it could be assumed to be under tension and rigid because the space between the membrane and the bead was ...lled with the blocking proteins ...sh-skin gelatin (FSG) and the proteins present in the surrounding cell membrane. Therefore, there was little space for a rotation of the bead-linker complex around its anchor point in the plasma membrane. In contrast, such rotational motion around the anchor point was observed for a sphere linked with kinesin ($l \gg 65nm$) to a microtubule ...xed on a coverslip [Florin et al., submitted 1998]. The experiments con...rmed the assumption of a direct coupling (see section 13.4 on p. 105).

- The three dimensions were assumed to be independent and the analysis was performed on each of them separately. Furthermore, it was assumed that a con...nement along one axis, like the cell surface limits the motion along this axis, but did not couple the motions. The experiments did indeed show that the lateral motion is not in‡uenced by the binding to a mobile membrane proteins.

Part III

Physical methods

Physical methods

This part describes established instruments and methods that were employed for the initial studies of the structure of the plasma membrane and the dynamics of the membrane proteins. The technologies developed on the basis of the experiences with these methods will be discussed in part IV.

In chapter 3, the technique of tracking sub-microscopic particles by video-enhanced microscopy to study the motion of membrane proteins is described. Single-particle tracking (SPT) was implemented and applied to study the membrane dynamics in developing hippocampal neurons. This section summarizes the particularities that need to be considered when applying SPT to neuronal cells: First, neuronal cells are extremely light sensitive cells, so low-light level diﬀerential-interference contrast (DIC) microscopy was used. Second, the neurites are submicrometer structures with high DIC-contrast, so that special tracking algorithms had to be developed. Section 3.2 discusses, how the diﬀusion coeﬃcient is obtained from a SPT-trajectory.

Chapter 4 is an introduction to scanning force microscopy (SFM) in biology and the necessary requirements to apply SFM to image the plasma membrane of intact cells.

To reduce the contact force to minimize deformation during the imaging of the cell membrane the photonic force microscope (PFM, chap. 6) was developed on the basis of the single-laser gradient trap, which is described in chapter 5. The principle of a laser trap and the theory of trapping-force generation on Raleigh particles are summarized in section 5.1. To measure forces with a laser trap, the position displacement of the trap needs to be measured and the trapping potential to be calibrated. Section 5.2 describes various lateral position sensors. A detector developed to determine displacements along the optical axis by measuring the two-photon ﬂuorescence intensity excited in the trapped probe is presented in section 5.2.1. Several calibration methods for the laser trap are presented and compared in section 5.3. A newly developed fast three-dimensional position sensor exploiting the interference of the scattered light is described together with the PFM in chapter 6. The PFM with the fast three-dimensional position sensor is the basis for the thermal noise analysis performed to study the local diﬀusion of membrane proteins and microdomains (see chapters 8 and 13).

Chapter 3

Single-particle tracking by video-enhanced microscopy

3.1   Principle of video-tracking

Single-particle tracking (SPT) based on video microscopy has been inventioned about ten years ago to study the motion of proteins and lipids in cell membranes [Geerts et al. 1987, DeBrabander et al. 1988, Gelles et al. 1988]. The trajectory of a single molecule or a small group of molecules can be visualized by tagging them with either highly ‡uorescent particles [Gosh and Webb 1994] or nanometer-sized gold or polystyrene probes [Geerts et al. 1987, Gelles et al. 1988].
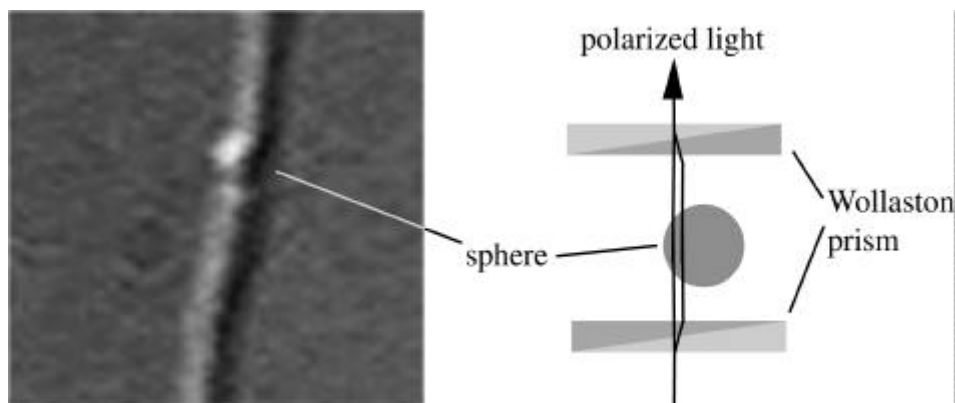
Figure 3-1: (a) DIC image of a 0.2 ¹m-diameter sphere on a small neurite. (b) The polarized DIC illumination light is passed through a Wollaston prism and split into an ordinary and an extraordinary beam. Behind the sample the two are combined in another Wollaston prism and analyzed in a polarizer.

The simplest detection principle for a particle in an image is an intensity threshold. A threshold detection is applicable to ‡uorescent objects or particles large

enough to scatter or absorb signi…cantly more light than their environment. Due to the sensitivity of the hippocampal neurons, only low light levels are applicable, ruling out ‡uorescence detection and limiting the achievable image contrast.

To avoid binding multiple membrane proteins on one sphere and to minimize the viscous drag from the sphere, only very small spheres were used (r ¼ 0:1 ¹m). These sizes require di¤erential-interference contrast (DIC) microscopy to be detected. For DIC, the polarized illumination light is passed through a Wollaston prism to split it in an extraordinary and an ordinary beam. The collected light is again passed through a Wollaston prism and analyzed in a polarizer. This method yields high contrast at edges of refracting objects. Dielectric spheres, as the polystyrene beads used, with diameters smaller than the wavelength appear with one bright and one dark side, the separation being orthogonal to the Wollaston prism. Because the neurites of the hippocampal neurons are cylindrical objects with diameters between 0:2 ¹m and 1 ¹m, they also appear with a bright and a dark side if they are orientated orthogonal to the Wollaston prism, but with very little contrast if orientated parallel to the prism. Therefore, neurites oriented parallel to the prism were selected for the tracking experiments. The detection algorithm is based on selecting an image mask of the sphere manually from one of the images in the series. The centroid of this object is calculated. In the subsequent images the algorithm searches for this object within the vicinity of the centroid comparing areas of the actual image to the image mask by cross-correlation. If a certain level of agreement that has to be determined empirically, is found, the new centroid coordinates are calculated and the image mask is adjusted to represent the actual image better. Is the object not found in one image frame the next one is analyzed. If the particle is detected again in an area reachable by di¤usion, the position at the intermediate image is interpolated, otherwise the trajectory is terminated and a new one is started with the next appearance of the particle (detailed description in Nguyen-Ngoc [1997]).

The trajectory of the centroid coordinates is analyzed to determine whether the tagged protein or lipid was di¤using freely and randomly, and to calculate the di¤usion coe¢cient (see section 4.2).

3.2 Estimating the di¤usion coe¢cient of a particle from its trajectory

Analysis of the trajectory

A …rst approach to analyze SPT data is to plot the recorded trajectories and categorize them according to their shape (see …gure (3-2a)). To analyze the motion more quantitatively the mean-square displacement MSD($¢t$) is computed, which is the area in which the particle is expected to remain after a time interval $¢t$. Plotting the MSD versus time provides a method to distinguish various di¤usional modes (see …gure (3-2b)) and to determine the di¤usion coe¢cient of the tagged protein or
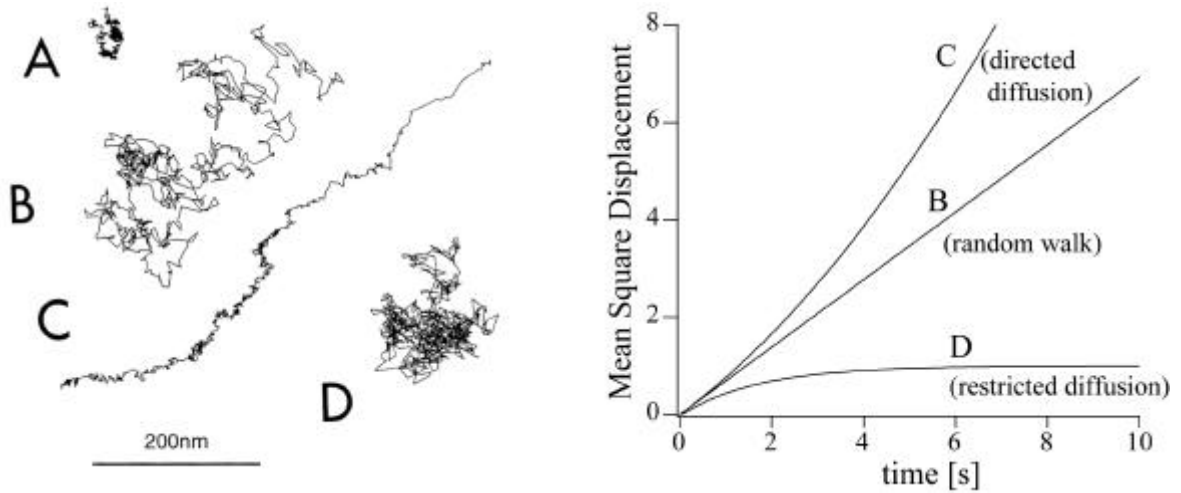
Figure 3-2: Modes of diffusion as 2D-video tracks (a) and the corresponding mean-square displacements (b). Stationary motion (A) results in no displacement. The MSD of a random-walk increases linearly with time (B), while directed diffusion results in a faster increase (C) and confined diffusion in a slower increase (D) [after Kusumi, 1994].

lipid. In one dimension one calculates the MSD as:

$$MSD_x(\Delta t_n) = \frac{1}{N - 1 - n} \sum_{j=1}^{N-1-n} [x(j\delta t + n\delta t) - x(j\delta t)]^2 ;$$ (3.1)

$$\Delta t_n = n\delta t; \qquad \delta t = 40ms \qquad \text{(video frame time)};$$

where $x(j\delta t + n\delta t)$ describes the particle position following a time interval $\Delta t_n = n\delta t$ after the starting position $x(j\delta t)$ and N is the total number of video frames. The procedure is visualized in following figure
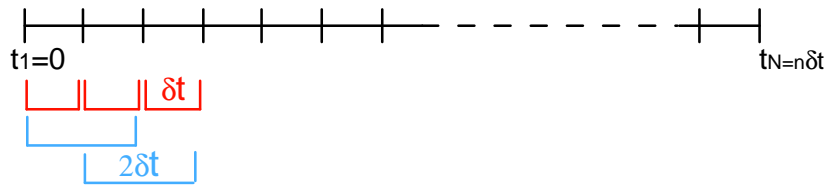
The two-dimensional MSD is the sum of the MSDs in x- and y-direction: $MSD = MSD_x + MSD_y$. For a purely random walk the MSD is expected to increase linearly with time (see eqs. (1.5) and (2.7b)):

$$MSD_x(t) = 2D_x t, \quad \text{and 2 dimensions } MSD(t) = 4D t :$$ (3.2)

31

Deviations hereof are explained by interaction of the di¤using molecule with its surroundings, resulting in various modes of di¤usion.

Modes of motion

Kusumi et al. [Kusumi et al., 1993; Sako and Kusumi 1994 , and 1996] distinguish ...ve types of trajectories: a stationary mode, simple, directed or restricted di¤usion, and obstacle impeded di¤usion. The e¤ect of mobile and immobile obstacles on the di¤usion have been investigated in a series of papers by Saxton [Saxton 1987, 1989, and 1992] in which he studies obstacle concentrations up to the percolation threshold and pining e¤ects. However, the distinction between free di¤usion and obstacle impeded is very di¢cult at the resolution provided by conventional two-dimensional SPT. I will just summarize the basic di¤usional modes, because the question addressed by conventional SPT in my thesis required only a distinction between those.

Stationary   The protein shows little motion in video tracking studies, as example A in ...gure (3-2). Kusumi categorizes here particles with $D < 5 ¢ 10^{i \ 12} cm^2=s$.

Simple di¤usion   Di¤usion with the characteristics of a random walk: a linear dependence of the MSD on the time, as example B in ...gure (3-2).

Directed di¤usion (transport mode)   If a direct motion or drift with velocity v is superimposed on the random di¤usion the MSD increases faster, see example C in ...gure (3-2):

$$MSD(t) = 4D \ t + v^2 t^2$$

Restricted di¤usion   The particle undergoes Brownian di¤usion within a limited area and cannot move out of this area during the observation time, see example D in ...gure (3-2). The motion is equivalent to free Brownian di¤usion within an in...nitely high square well potential. Observing this motion has led Kusumi to propose the membrane skeleton fence model, in which the motion of transmembrane proteins is limited by the interaction with the membrane skeleton. [Sako and Kusumi 1994, and 1995].

Discussion

Many of the uncertainties in the analysis of SPT trajectories arise from the limitation of video microscopy to a planar projection of the three dimensional surface and from the low temporal resolution (usually 25 Hz). Because of the statistical movement the motion has to be averaged over several hundred positions along the trajectory (see sect. 2.3). For video tracking with the limited temporal resolution of 25Hz this corresponds to a trajectory of several seconds duration and a few micrometers

length. Therefore, the result is the average over a larger area of the cell surface and includes e¤ects of collisions with other mobile and immobile membrane proteins.

As an experimental solution to these problems we have developed fast three-dimensional SPT and the con...nement of the probe by a laser trap to measure (see chap.10 on p.75) to perform local measurement of the di¤usion coe¢cient (see chap.8).

Chapter 4

Scanning Force Microscopy in cell biology

Scanning probe microscopy has grown into a broad ...eld of applications since the introduction of the atomic force microscope (AFM) by Binnig and colleagues in 1986, which used the repulsion between a sharp tip and a surface to image the topography of the surface by scanning the tip over it. In the following years, a series of modi...ed AFMs was introduced using various surface-tip interactions, like long-reaching forces as electrostatic and magnetic ones, or contact properties like hydrophobicity. Accounting for the di¤erent interaction forces exploited, these instruments are better summarized as scanning force microscopes (SFM). Besides being used for imaging SFM has been used to measure Pico- to Nanonewton forces locally without scanning the tip.

SFM has been introduced into biology after Hansma and Drake developed and commercialized instruments that could be applied in aqueous environment [Drake et al., 1989], allowing biological samples to be studied under physiological conditions. 1990, Gould and colleagues produced ...rst SFM images of the surface of ...xed red blood cells, bringing SFM into cell biology. In 1992, Häberle et al. achieved the ...rst series of images on individual living cells showing sub–membranous dynamics and the exocytosis of a viral particle. Recently, LeGimellec and colleagues [1998] have imaged the surface of polarized cells in a monolayer and shown that the resolution on these cells is limited by a dense glycocalix. Besides imaging the structure of the cellular surface on living cells, also the mechanical properties [Radmacher et al., 1993] became measurable. The only prerequisite is that the elasticity of the imaged surface is in the range of the force constants of the cantilevers used [see chap. 6.3. and Burnham, 1994]. Macromolecular resolution has been achieved only on proteins adsorbed to a solid surface [Müller et al., 1997a] and in specialized areas on cells, like the gap-junctions [Hoh et al., 1993]. On the single molecule level, conformational changes of molecules adsorbed to surfaces have been imaged [Müller et al., 1997b], intermolecular force measurements between individual proteins [Florin et al., 1994; Moy et al., 1994; Lee et al., 1994] and intramolecular force of one protein [Rief et al., 1997a, 1997b and 1997c] have been measured.

Scanning procedures

Several scanning and imaging modi have been developed in the past decade. The basic characteristic of a scan modus is the contact time between sample and probe, either continuously, or intermittent up to non-contact. To image the cellular surface (section 9.1) "constant contact force microscopy" was applied. This group of modi can be further classi...ed by the response time of the feedback loop including the cantilever:

² In the "constant height mode" the response time of the feedback is adjusted so that the cantilever is guided in contact following the shallow slopes of the sample substratum but not the sample itself while the cantilever's de‡ection is recorded in each point of the scan. An increase of the cantilever de‡ection corresponds to a surface protrusion but also results in an increase of the force exerted onto the specimen by the probe which is not desirable on soft biological samples.

² In the "constant force mode" the cantilever de‡ection is kept constant by a fast feedback loop. Due to the resonance frequency limited response time of the feedback circuit including the driving piezo, a true "constant force mode" is requires extremely slow scan speeds.

² The contact mode mostly used is therefore is the "error mode", a mix of constant height and constant force mode. The feedback loop is set to an intermediate response time and the feedback output as well as the deviation of the cantilever de‡ection from its set-point are recorded as topography and as error signal, respectively. The error signal contains information about the ...ne structure and the feedback signal the calibrated but smoothed topography of the sample.

Besides these "constant contact modi", various "intermittent contact modi" have been developed in which the sample-probe distance is modulated. The decrease in contact time reduces the lateral forces substantially and allows imaging of material properties like elasticity. Examples for this class of modi are the tapping mode[TM1] developed by Hansma et al. [1994] and Putman et al. [1994] as well as the force-curve mapping from Radmacher et al. [1993].

Set-up of the SFM

The scanning force microscope used was developed at EMBL. It has been described in further detail elsewhere [Eckert 1996, Dipl.Thesis].

---

[1]TM - Tapping mode is a registered trade mark of Digital Instruments, Santa Barbara, CA.

Chapter 5

Single Gradient Laser Trap

In 1986, the invention of the single gradient laser, or optical tweezers, by Ashkin [1986, 1987] o¤ered a new way to manipulate small dielectric particles with diameters from several ten nanometers to several micrometer. In combination with a lateral positioning sensor, the optical tweezers are used to apply [Block et al., 1989, 1990] and to measure [Svoboda et al., 1993; Finer et al., 1994] forces in the Piconewton range.

5.1   Forces in a single gradient laser trap

The forces acting on a dielectric particle held in a single gradient laser trap depend on the size of the particle, its relative refractive index and polarizability. To describe the trapping phenomena theoretically, one has to discriminate three regimes according to the ratio of radius r of the trapped bead to the wavelength ¸ of the trapping laser beam (here 1064nm):

² r ¿ ¸; the particle is small in relation to the wavelength used, which is the Rayleigh-scattering regime. Up to r < ¸=2 the forces are described by the electromagnetic theory [Wright et al., 1994; Visscher and Brakenho¤, 1992a]. It applies to the small latex spheres (radius 100nm) used in this study.

² r À ¸, the particle is large relative to the wavelength, at least 2¼r ¸ 100¸ [Bakker-Schut et al., 1991]. This is called Mie regime. Here the geometrical optics model [Ashkin et al.,1986 ; Visscher and Brakenho¤,1992b] is valid, explaining the trapping force as the result of a moment transfer of the light refracted and re‡ected by the trapped sphere (see ...gure 4-1).

² r ¼ ¸; when the particle is about the size of the wavelength, the highest lateral trapping forces are achieved. Therefore, these sphere sizes are often chosen for applications in biology, but this regime is not well described by either theory. In 1996, Wohland et al. have developed a submicroscopic theory based on modi...ed Gaussian beam optics .

36

Figure 4-1:

Single-gradient laser trap: The sphere is trapped behind the geometric focus in the diverging part of the Gaussian beam. In the geometrical optics model the trapping is a result of the momentum transfered from the refracted light onto the trapped bead.
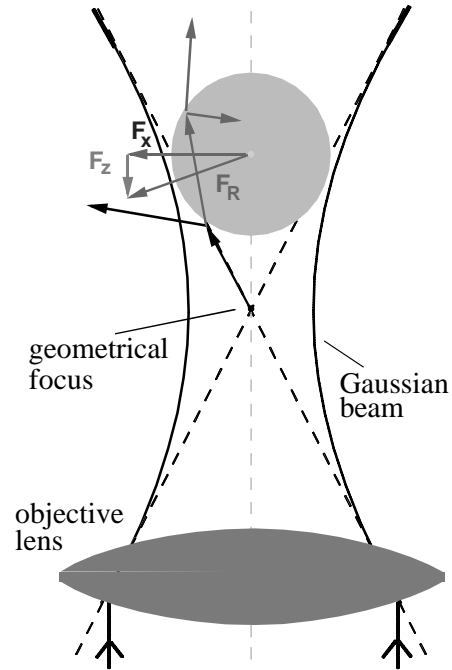
The spheres used in imaging with the PFM and in the diffusion measurements have a radius $r = 0.108 \mu m$ ($\lambda = 1.064 \mu m$). So the theory based on the Rayleigh-scattering is applicable: the scattered light pushes the particle along the optical axis while the interaction of the induced dipoles with the field gradient of the laser light attracts the particle.

The momentum transfer from the scattered light onto the particle is proportional to the light intensity and the scattering cross-section:

$$F_{scatter} = \frac{8}{3}\pi (kr)^4 n_s r^2 \left(\frac{m^2 - 1}{m^2 + 2}\right)^2 \frac{|S|}{c} = \frac{8\pi}{3}\frac{k^4}{n^3}\alpha^2\frac{|S|}{c} \tag{5.1}$$

with the Poynting vector S, the refractive index of the particle n, the solvent n_s and the ratio $m = \frac{n}{n_s}$ thereof, and the light speed c and wave vector k in the solvent. The factor in front of the Poynting vector is the scattering cross-section of the trapped particle.

The lateral force caused by the gradient of the light intensity is proportional to the gradient and acts in its direction [Svoboda and Block,1994]. It is caused by the interaction of the induced electrical dipoles with the field gradient of the laser light:

$$F_{grad} = \frac{n_s^2 r^2}{2}\left(\frac{m^2 - 1}{m^2 + 2}\right) \nabla \left| E^2 \right| = \frac{\alpha}{2r}\nabla \left| E^2 \right| \tag{5.2}$$

The factor in front of the gradient is the polarizability $\alpha = n^2\frac{m^2-1}{m^2+2}r^3$ [Jackson, 1975] of the trapped particle. At $\lambda = 1064nm$, the polarizability of a silica bead (n = 1.45) in aqueous solution ($n_s = 1.33$ [Hale, 1973]) is $\alpha = 0.059r^3$.

37

To trap a particle the gradient force has to counteract the scattering force. This is only possible for particles with refractive indices higher than the surrounding medium (m > 1) and in the divergent part of the beam, just behind the focus. The axial force is mainly determined by the scattering cross-section and light intensity, so it grows monotonously with increasing light intensity and bead radius. The lateral force is determined by the gradient of the beam, so a high numerical aperture is essential for good trapping. The ratio of axial to lateral trapping force has to be taken in account when imaging surfaces with the PFM and also for the studies of the con...ned Brownian motion near surfaces. In the submicroscopic theory Wohland estimated and measured that the axial force grows monotonically with bead size, while the lateral force has a maximum for spheres with radii of about the wavelength. For $r = 0:5^1$m he estimates and measures $F_{axial}=F_{lateral} \gg 0:1$, while the ratio is about $0:5$ for $r = 1^1$m. For the spheres used for imaging ($r = 0:1^1$m) the ratio measured was $F_{axial}=F_{lateral} \gg 0:1$ (see section 10 on p.75).

5.2 Position detectors

To measure forces using the optical trap or to study the Brownian motion in the trapping potential the displacement of the probe from the trapping position must be known precisely. Several detectors have been developed to measure lateral displacements: an interferometer using the polarization of the laser light to measure lateral displacements along one axis [Svoboda et al., 1993] and a quadrant photodiode [QPD] placed in the back-focal plane [BFP] of the condenser [Finer et al., 1994; Svoboda and Block, 1994, Allersma et al., 1998] to measure lateral displacements in two directions in the focal plane. The only measurement of the axial position was done by Denk and Webb using an over...lled photodiode placed behind the condenser [Denk and Webb, 1990; Gishlain et al., 1994]. During the development of the photonic-force microscope (section 7) two new ways to measure the axial position of a sphere held in the laser trap were introduced:

² a confocal device measuring the ‡uorescence intensity emitted by a ‡uorophore containing bead that is excited by the trapping beam via a two-photon process to determine the axial displacement [Florin et al., 1996] and

² a measurement of the total intensity scattered on the trapped bead and detected by a QPD in the BFP to determine the axial position, creating with the lateral signals of the QPD a fast, three-dimensional detector [Pralle et al.,1998b]. (This position signal will be described with the three-dimensional sensor of the PFM (section 6.1 on p.44).)

5.2.1 Axial position sensing by two-photon ‡uorescence

In optical tweezers the light of the trapping IR-laser ($_\circ = 1064$) can be utilized to excite the ‡uorophores inside a polystyrene bead by a two-photon process. The

38

theory of the two-photon process was developed by Göppet-Mayer in the 1930s: two photons of wavelength λ are absorbed simultaneously by a dye with an excitation wavelength $\lambda=2$. Today, two photon excitation is widely used in fluorescence microscopy in biology to avoid the photo-damage caused by the shorter wavelength one photon excitation [for a review see Denk and Svoboda 1997]. While the excitation of free fluorophores requires high intensities only achieved in pulsed lasers, the fluorophores densely packed inside a polystyrene bead are excitable using a few hundred milliwatts continuous-wave (cw) laser intensity [Florin et al. 1996].

The quadratic dependence of the two-photon fluorescence on the intensity of the exciting light can be used to build a displacement sensor for fluorescent spheres. If a force, i.e. the repulsion from a surface, pushes the sphere from its resting position in the trap, the two-photon fluorescence intensity is changed. Figure 5-2 shows the fluorescence intensity of a 0.2 μm-diameter sphere induced by the two-photon absorption process. Part (a) shows the approach of a trapped sphere to a surface (xxx). In the last 2-3 μm near the surface, the fluorescence intensity increases $\gg 10\% = \mu$m, further away from the surface, it is largely distance independent. The second trace (+++) is the recording of a fixed sphere scanned axially through the focus. The point of contact, when the fluorescence intensity drops in the approach trace, is about 300nm behind the point of highest fluorescence intensity, the geometrical focus, showing the fact that the bead is trapped well behind the geometrical focus [Wohland et al., 1996]. From there on, the bead is shifted out of its equilibrium position, which results in a steep intensity drop down to the background level within approximately one micrometer. A linear response (90% decrease $= \mu$m) within the first 500nm of displacement can be assumed. Laterally the sphere's resting position is on the optical axis (b). Therefore, for small displacements the two-photon fluorescence intensity is only weakly dependent on the lateral position. This offers a relative simple scanning and calibration procedure using the fluorescence signal a axial position signal to image with the scanning photonic force microscope.

The fluorescence intensity profile along the optical axis is a convolution of the fluorophore distribution and the point spread function (PSF) of the laser focus, but is disturbed by optical effects such as spherical aberration. For 200nm beads, the intensity depends weakly on the bead size, which can be numerical simulated assuming a homogeneous distribution of dye in the bead [Lindek, Florin private communication]. This explains the well reproducible position sensitivity and allows us to use the position sensitivity from independent measurements. For the small 0.2 μm latex beads used in the PFM-imaging the two-photon fluorescence signal contains mainly information about axial displacement because the ratio of the axial to the lateral spring constant of the laser trap is about 1 : 9 [see chapter 13.0.2; Wohland et al., 1996]. The resolution is limited by the photon statistics and depends on the used sphere size, laser intensity and integration time of the photon counter. For the spheres and laser intensities used for imaging only integration times larger than 1ms resulted in a reasonable signal to noise ratio limiting the image acquisition speed.
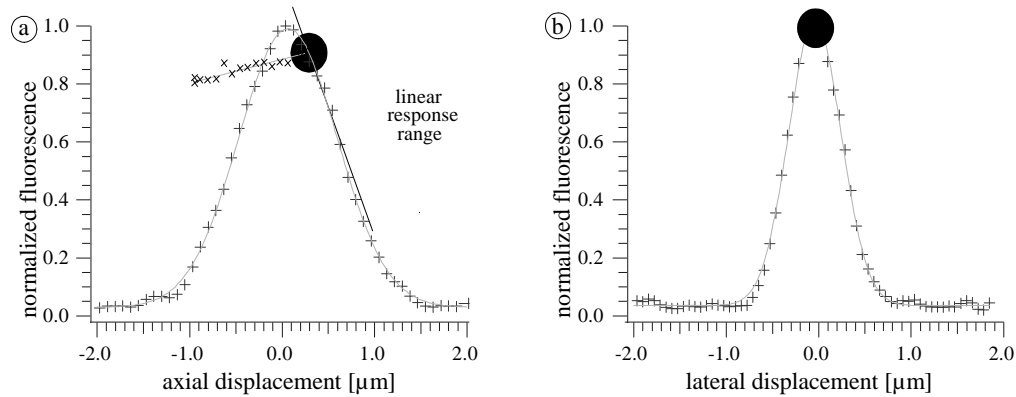
Figure 5-2: The normalized two-photon ‡uorescence intensity (+ + +) while moving a ...xed 0.2 ¹m-diameter sphere along the optical axis in the direction of the laser light (a) and laterally in the focal plane across the laser beam (b). The approach-trace (xxx) in (a) is recorded while moving a sphere held in the trap towards the surface of the bottom coverslip of the sample chamber until it is displaced from the trapping region (increasing axial displacements). The sphere drawn represents the resting position in the trap.

5.3   Laser trap force calibration methods

The force acting on a trapped sphere depends on the sphere's size, the laser intensity and the gradient of the ...eld (see section 5.1 on p. 35). Therefore, the laser trap has to be calibrated for each experiment, ideally at the position of the sample in the chamber where the experiment is performed with the sphere used for the experiment. Experimental methods to calibrate the force ...eld of optical tweezers can be divided in two categories: First, calibration against a known force or resistance (e.g. gravitation or Stoke's friction) and second, the analysis of thermal ‡uctuations. Conventional calibration methods based on thermal noise analysis have to assume a harmonic potential and must know parameters such as the viscosity of the medium [Gishlain et al. 1994]. These methods can only be applied in the bulk solution because near the surface the stokes drag changes due to the con...nement. But most force measurements are performed near a surface.

Therefore, we have developed a calibration method based on the Boltzmann statistics of the thermally activated position ‡uctuations of the trapped particle, this calibration and pro...ling of the laser trap potential needs no prior knowledge, but the temperature T (for details see the section 2.0.3, p.20)

5.3.1   Classical methods

Classical methods relying on actively moving the bead or spectrum analysis of a thermally excited bead are the following:

Stokes drag

To move a sphere of radius r through a medium of viscosity η, with speed v, the force $\mathbf{F}_{Stokes}$ caused by the Stoke's drag $\gamma = 6\pi\eta r$, has to be overcome:

$$\mathbf{F}_{Stokes} = -6\pi\eta r \cdot \mathbf{v}$$

Applying it to a laser trap offers two configurations: either the bead is accelerated until it drops out of the trap, such measuring the maximum holding force, or the bead is moved at a constant speed and the displacement from the trap center is measured, making a spring-constant measurement in the form of a force-displacement relationship. In both methods, the laser focus is scanned laterally by the scanning mirrors. In the later case a position detector is necessary. Errors in this method are caused by uncertainties of the viscosity of the medium that is temperature dependent, the variation of the bead radius and the movement of the scanning mirrors. When using a position detector another potential error source is introduced.

Root-mean square (RMS) amplitude

Using a fast position sensor the position fluctuations of a thermally excited trapped bead can be measured as time-series. Assuming the trapping potential being harmonic, the equipartition theorem is applied to yield:

$$\begin{aligned}
\frac{1}{2}\kappa \left\langle x^2 \right\rangle &= \frac{1}{2}k_B T \\
\kappa &= \frac{k_B T}{\left\langle x^2 \right\rangle}
\end{aligned}$$

with the spring constant κ, the displacement of the bead from the focus x and the thermal energy $k_B T$.

Corner frequency

The spectrum of the thermal position fluctuations of a sphere in the trap can be described as an overdamped harmonic oscillator which is characterized by the Lorentz-spectral density [Reif, 1965]:

$$A^2(\omega) = \frac{A_0^2}{1 + \left(\frac{\omega}{\omega_c}\right)^2} \qquad \text{whereby } \omega_c = \frac{\kappa}{\gamma} = \frac{\kappa}{6\pi\eta r \cdot \mathbf{v}}$$

with the displacement amplitude A for a frequency $\omega = 2\pi f$, corner frequency $\omega_c = 2\pi f_c$, the spring constant κ and the Stokes drag γ.

5.3.2 Potential profiling by thermal position fluctuation

Analyzing the Boltzmann statistics of the thermally activated position fluctuations of the trapped particle allows to profile the trapping potential even below the thermal energy with a temporal and spatial resolution given by the strength of the potential and the bead size. Interestingly, since this calibration method depends only on the temperature, it allows us to measure other parameters such as the local viscosity by combining it with viscosity dependent calibration methods. Analyzing the Boltzmann distribution overcomes the restriction of harmonic potentials and requires only minimum knowledge about the system, i.e. only the temperature is needed. The diameter of the particle used and therefore, the spatial resolution is only restricted by the ability of the optical trap to generate a potential well with a depth of about ten times the thermal energy $k_B T$ and by the sensitivity of the position detectors. (for theory chapter, sect. 2.0.3).

5.3.3 Comparison of the calibration methods

To compare the various methods a series of measurements was done with $0.2\,\mu m$ sized beads ($r = 108\,nm \pm 3.8\%$). All the measurements were done in distilled water about $5.5\,\mu m$ above the coverslip surface to eliminate hydrodynamic interactions with the surface. The laser power was set to roughly 40mW, the temperature kept at $T = 29.5^0 C$, then the viscosity of water is $\eta = 8 \cdot 10^{-4}\, Pa\,s$. The resulting lateral spring constants with errors are summarized in the following table:

	κ [N/m]	E_{tot}	$\pm r$	$\pm T$	$\eta(\pm T)$	$\pm x$	$\pm S$	»
Stokes drag	$1.39 \pm 0.29 \cdot 10^{-5}$	21%	3.8%	—	4.2%	1.3%	3%	9%
corner freq.	$1.36 \pm 0.15 \cdot 10^{-5}$	11%	3.8%	—	4.2%	—	3%	3%
rms-noise	$1.50 \pm 0.10 \cdot 10^{-5}$	6.7%	—	2%	—	—	3%	—
Boltzmann	$1.45 \pm 0.10 \cdot 10^{-5}$	6.7%	—	2%	—	—	3%	—

Table 5.1: Determination of the lateral spring constant κ of a $0.2\,\mu m$-sphere in the laser trap by various methods.

The methods relying on the viscous damping have higher total errors E_{tot} because they depend on the spheres radius r and the highly temperature sensitive viscosity $\eta(T)$ as well as on the position detectors's sensitivity κ. The calibration using the Stokes drag by actively moving the sphere through the medium is the most error prone because it also includes uncertainties due to the hysteresis of the scanning mirrors $\pm x$ as well as statistical errors ». Statistical methods, like 'rms-noise' and 'Boltzmann', are only sensitive to inaccuracies in the position detector sensitivity s and linearly dependent on temperature changes, so they have the smallest error. Visualizing the potential by profiling the thermal position fluctuations provides in addition a measure for local deviations form a harmonic potential, so it is our method of choice.

Part IV

Physical methods developed

Physical methods developed

On the basis of the existing instruments described in the previous part (III), the following methods were developed: 3D-SPT in the laser trap with a fast 3D position sensor based on the interference of the scattered with the unscattered laser light (section 6) and a scanning photonic force microscope (SPFM) using the two-photon ‡uorescence as position signal (chapter 7). The 3D-SPT allows to pro...le the three-dimensional trapping potential of the laser trap and changes due to external potentials and is applied to visualize the di¤usion of a membrane protein around the 3D cell surface. The SPFM is used to image the cell membrane with sub-Piconewton contact force (see chap. 9.2 on p.69).

Section 6.1 describes the principle of the 3D position measurement using the forward scattered light. The interference signal of a Raleigh scatterer near the focus of a Gaussian beam is calculated in section 6.2 and compared to the measured detector response. Section 6.3 provides a methods to calibrate the detector response near the point of the measurement and with the sphere to be used for the experiment by exploiting the thermal position ‡uctuations. Chapter 7 summarizes the design (sect. 7.1, p. 54) and scanning modes (sect. 7.2, p.55) of the SPFM. Chapter 8 discusses the applications of the 3D-SPT to pro...le the trapping potential and to measure the local viscous drag near a surface. The results obtained are compared to the theory by Brenner [1965] (see sect. 2.1.1).

Chapter 6

3D single-particle tracking and photonic force microscopy

To study the potential and dynamics at the molecular level the position of the marker bead needs to be determine in three-dimensions at high temporal and spatial resolution. Because of the thermal noise, it is not possible to con...ne the motion into one or two dimension. Also would this alter the response of the natural system, which is governed by a three-dimensional potential. Therefore, we have developed a fast three-dimensional position detector, capable of nanometer spatial and microsecond temporal resolution by using the forward scattered laser light and detecting the interference pattern with a quadrant photodiode (QPD).

6.1   3D-position sensing using forward scattered light

Detection of the forward scattered light by a position sensitive device such as a QPD has been used to measure the lateral position of a trapped sphere along one axis [Finer et al., 1994] and by Allersma et al. [1998] to perform two-dimensional in-plane single-particle tracking (SPT). We have shown, that using a QPD in the BFP and measuring the total intensity of the forward scattered light provides in addition to the lateral signals a sensor for axial displacements.

The mechanism of the position sensitivity of a QPD in the BFP had been unclear until, recently, a one-dimensional theoretical description for the lateral displacement in the focal plane was given by Gittes and Schmidt [1998]. The measured intensity changes are described as interference of the light scattered on the sphere with the non-interacting transmitted light. In the following the theoretical description is performed for the general three-dimensional case.
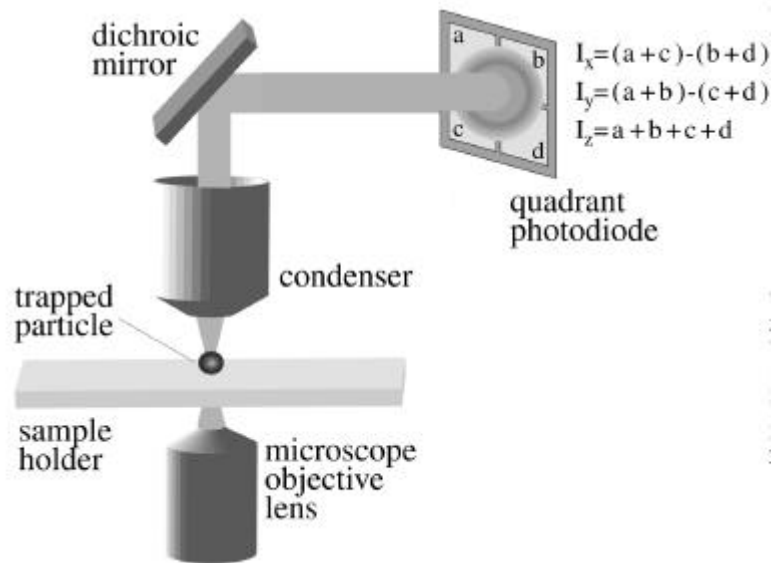
Figure 6-1: Arrangement of QPD in BFP of condenser to measure forward scattered light for 3D position sensing. Part of the trapping laser light is scattered by the trap particle and interferes with the light passing unscattered. The interference pattern is detected by the QPD.

6.2 Theoretical description of the 3D-position sensor signal

The developed model for the general case of an arbitrary but small displacement of the trapped bead in three dimensions, assumes that the trapped sphere can be described as a Rayleigh scatterer (i.e. a dielectric sphere with a radius r much smaller than the wavelength λ). In the Born approximation [Born and Wolf, 1989], the finite size of the sphere is accounted for by assuming a polarizability $\alpha = n^2 \frac{m^2-1}{m^2+2} r^3$, $m = \frac{n}{n_s}$ (see p. 36): The QPD detects the light scattered forward only in a small angle. The scattering cross-section is then independent of the polarization of the light [Jackson, 1975]. The bead position s' is given in cylindrical coordinates (z', $\rho'^2 = x'^2 + y'^2$, $\varphi' = \arctan \frac{y'}{x'}$), while the interference of scattered and unscattered light is observed at point s in the spherical coordinates $s; \vartheta; \varphi$ around the optical axis (see fig. ??). The propagating field is described as a Gaussian beam with the scalar wavenumber $k = |k| = \frac{2\pi n}{\lambda}$, the radius of the Gaussian beam $R(z) = z \left[1 + \left(\frac{z_0}{z} \right)^2 \right]$, the beam-waist radius in the focal plane $w_0 = \sqrt{\frac{\lambda z_0}{\pi}}$ and its variation along the optical axis $w(z) = w_0 \sqrt{1 + \left(\frac{z}{z_0} \right)^2}$, the Rayleigh length of the focus $z_0 = \frac{\pi w_0^2}{\lambda}$, and the phase $\zeta(z) = \arctan(\frac{z}{z_0})$ [Saleh and Teich, 1991]. Passing the focus the field undergoes the Gouy-phase jump, resulting in a 90° phase shift between scattered and unscattered
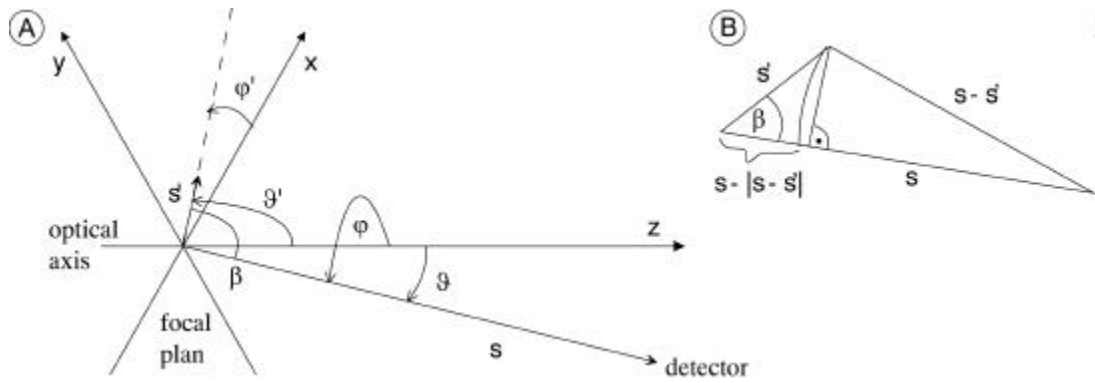
Figure 6-2: Coordinates and angles used for the calculation. (A) The laser beam is passing from the left, the bead placed at s^0 near the focus and the detector at s to the right. (B) Relationship of $\bar{}$ to s and s^0, needed for eq.(6.6).

light in the far field. The Gaussian field becomes [Saleh and Teich, 1991]

$$E(s) = E_0 \frac{w_0}{w(z)} \exp\left[-\frac{\%^2}{w^2(z)}\right]^{1/2} \exp\left[-ikz - ik\frac{\%^2}{2R(z)} + i\vartheta(z)\right]^{3/4} : \qquad (6.1)$$

In the detection plane far from the focus ($s \gg z_0$) with the approximations $\vartheta(z) = \arctan\frac{z}{z_0} \approx \frac{\pi}{2}$, $w(z) \approx \frac{w_0}{z_0}z$, $\sin\# \approx \#$, $z \approx s$, and $R(z) \approx 1$ the unscattered field is

$$E_u(s) \approx iE_0 \frac{kw_0}{2s} \exp\left[-iks - \frac{1}{4}k^2w_0^2\#^2\right] ; \qquad (s \gg z_0) \qquad (6.2)$$

normalized by $E_0 = 2=(w_0 \sqrt{\frac{\pi}{4}\epsilon_s c_s})$ onto total intensity $I_{tot} = 1$, with c_s the speed of light in the solvent. If a particle with polarizability $\circledR$ is placed at a lateral position s^0 near the geometric focus, the Rayleigh approximation for the scattered field at large s ($|s| \gg z_0$) is

$$E_s(s; s^0) \approx \frac{k^2 \circledR}{s} E(s^0) \exp[ik|s - s^0|] : \qquad (6.3)$$

The non-interfering light $|E_u(s)|^2$ subtracted as the background from the time-averaged intensity I of interference between laser beam and scattered light. The relative change of the intensity I is

$$\pm I = \frac{\epsilon_s c_s}{2} \left\{ |E_u(s) + E_s(s^0)|^2 - |E(s)|^2 \right\} \approx \epsilon_s c_s \, \text{Re}\langle E_u(s)E_s^\pi(s^0)\rangle ; \qquad (6.4)$$

$\frac{1}{2}|E(s) + E(s^0)|^2$ is the time-averaged squared real part of the sum $(E(s) + E(s^0)) e^{i\omega t}$, and $|E(s^0)|^2 \to 0$, ignoring any higher order interference. Using eqs. (??) and (6.2) the intensity change in the BFP for a displacement s^0 of the bead from the focus

47

with $s = |s|$, $s' = |s'|$ becomes

$$\frac{\pm I \, (s; s')}{I_{tot}} = J \, (s; s') \sin \left[k \left(|s_{\parallel} - s'| - z' \left(\frac{\%'^2}{2R \, (z')} + \frac{3 \, (z')}{k} \right) \right) \right] ; \quad (6.5)$$

$$\text{with } J \, (s; s') = \frac{2k^{3}}{\frac{1}{4}s^2} \left[1 + \left(\frac{z'}{z_0} \right)^2 \right]^{-\frac{1}{2}} \exp \left(-\frac{\%'^2}{w^2(z')} \right) e^{-\frac{1}{4}k^2 w_0^2 \#^2} : \quad (6.6)$$

The angle $\bar{}$ between s and s' is given by [see …g. ??(b) together with Bronstein and Semendjajew, 1991]

$$\cos \bar{} = \frac{s \cdot s'}{|s| |s'|}$$
$$= \sin \# \sin \#' \cos ' \cos ' ' + \sin \# \sin \#' \sin ' \sin ' ' + \cos \# \cos \#' : \quad (6.7)$$

Because for small displacements $s' \sin \bar{} \ll s$, we substitute $s_{\parallel} - |s| - s'| \approx s' \cos \bar{}$. The relative change in the time-averaged light intensity I due to interference from Eq. (6.4), simpli…ed with $\tilde{A}' = \arctan(z'/\%') = \frac{1}{4} = 2 - \#'$, $\hat{A} = ' ' - '$ and $\cos \# \approx 1$, becomes then

$$\frac{\pm I \, (s; s')}{I_{tot}} = J \, (s; s') \sin \left[k \left(s' \cos \tilde{A}' \sin \# \cos \hat{A} + s' \sin \tilde{A}' - z' \left(\frac{\%'^2}{2R \, (z')} + \frac{3 \, (z')}{k} \right) \right) \right] : \quad (6.8)$$

The interference pattern is observed by a QPD, so for all signals the change in intensity $\frac{\pm I}{I}$ is integrated over the sector in space spread by the angles $\#$ and $'$. The angle $\#$ runs from 0 to $\#_{max}$, where $\#_{max}$ can be set to in…nity since $\frac{\pm I}{I}$ decays exponentially in $\#$. The z-signal is the total intensity, so $\hat{A}$ covers all angles:

$$\frac{I_z}{I} = \int_0^{\frac{1}{4}} d\hat{A} \int_0^{\#_{max}} d\# \, s^2 \sin \# \, \frac{\pm I \, (s; s')}{I_{tot}} : \quad (6.9)$$

The lateral signal is a result of the di¤erence signal between any two halves. Because of $\pm I_+ = - \pm I_-$ it is su¢cient to integrate the left half-space and the top half-space ($-\frac{1}{4}_2 < \hat{A} < \frac{1}{4}_2$ and $0 < \hat{A} < \frac{1}{4}$) for the x- and the y-signal, respectively. The integrations are performed analytically with the small angle approximation ($\sin \# \approx \#$). Then the lateral (x)-signal for a sphere at $s' = \{x'; y'; z'\} = \{\%'; ' '; z'\}$ is

$$\frac{I_x}{I} \, (s') = I \, (z') \left[A s' \cos \tilde{A}' \cos ' ' + B \left(s' \sin \tilde{A}' - z' \left(\frac{\%'^2}{2R \, (z')} + \frac{3 \, (z')}{k} \right) \right) \right] ; \quad (6.10)$$

with $I \, (z') = \frac{4k^{4}}{\frac{1}{4}} \left[1 + \left(\frac{z'}{z_0} \right)^2 \right]^{-\frac{1}{2}} \exp \left(-\frac{\%'^2}{w^2(z')} \right)$, $A = \frac{4P_{\frac{1}{4}}}{k^3 w_0^3}$ and $B = \frac{2\frac{1}{4}}{k^2 w_0^2}$. For the y-signal $\cos ' '$ is replaced by $\sin ' '$. The axial z-signal for an arbitrary displacement

s' is

$$\frac{I_z}{I}(s') = \frac{2\mu}{k^2 w_0^2} I(z') \left[s' \sin\tilde{A}' \mp z' \mp \left(\frac{\%^2}{2R(z')} + \frac{3(z')}{k} \right) \right] :\qquad (6.11)$$

This general three-dimensional description is reduced for a purely lateral displacement in one direction ($y' = z' = 0$) to the one-dimensional result of Gittes (Gittes and Schmidt, 1998)

$$\frac{I_x}{I}(x') = P\frac{16k^{\circledR}}{\mu w_0^2} \left(\frac{x'}{w_0} \right) \exp\left[\mp \left(\frac{x'}{w_0} \right)^2 \right] :\qquad (6.12)$$

In the two-dimensional case, for a displacement $\%'$ in the focal plane at an angle $'{}'$, the lateral x-signal is

$$\frac{I_x}{I}(\%'; '{}') = P\frac{16k^{\circledR}}{\mu w_0^2} \cos'{}' \left(\frac{\%'}{w_0} \right) \exp\left[\mp \left(\frac{\%'}{w_0} \right)^2 \right] :\qquad (6.13)$$

The axial signal is described on the optical axis ($x' = y' = 0$, $\cos\# \approx 1$) more exactly, if the sine-function is not approximated:

$$\frac{I_z}{I}(z') = \frac{8k^{\circledR}}{\mu w_0^2} \left[1 + \left(\frac{z'}{z_0} \right)^2 \right]^{\mp\frac{1}{2}} \sin\left(\arctan\frac{z'}{z_0} \right) \qquad (6.14)$$

Crosstalk of the three position signals

Using these calculations the crosstalk between the signals can be estimated. The lateral x-signal depends near the optical axis ($\frac{1}{2}' ' 0$) on any axial displacement z'

$$\frac{@}{@z}\left(\frac{I_x}{I}(s') \right)_{\frac{1}{2}' 0} \sim \left[1 + \left(\frac{z'}{z_0} \right)^2 \right]^{\mp\frac{1}{2}} :\qquad (6.15)$$

Using the value at $z' = 0$ for displacements of up to e.g. $z' = 150$ nm this results in an underestimation of the x-displacement by less than 10%. The crosstalk of the two lateral signals x and y in the focal plane ($z' = 0$) is determined by their ratio $q = \frac{y}{x}$ and the absolute value in x

$$\frac{@}{@y}\left(\frac{I_x}{I}(s') \right)_{z'=0} \sim \frac{q^2}{q^2 + 1} \exp\left[\mp \frac{(1 + q^2)q^2}{w_0^2} \right] :\qquad (6.16)$$

If a maximum underestimation of the displacement measurement of 10% is accepted, the detector response can be assumed to be linear up to lateral displacements of about x = 100nm, as long as the y-displacement is smaller than 60nm.

Measured detector response

The measured position signals of the QPD for a sphere, 0:3 ¹m in radius, are shown in ...gure 6-3. Part (a) and part (c) display plots of the x-position signal (as xy-image) and the z-position signal (as zx-image), respectively. Superimposed are the contours of the ...ts using the 3D-function in eq.(6.9) with z=0 and y=0, respectively. The theory describes the signal well up to displacements in the order of the focal dimension. The following ...t parameters were obtained from the x- and y-signals (data not shown): the beam-waist radius w_0 along the x-axis $w_{0x} = 0:33$ ¹m and along the y-axis $w_{0y} = 0:39$ ¹m. The z-position signal is ...tted best using $w_0 = 0:46$ ¹m and the Rayleigh length $z_0 = 0:73$ ¹m. Panel (d) displays a pro...le of the data and the 3D-...t taken at zero displacement along the optical-axis. In addition the 1D-...t obtained by eq.(6.13) is plotted. The 3D-function describes the detector response up to displacements smaller than the focal dimension well. The small angle-approximation which is necessary to perform the 3D-integration induces discrepancies between the theory and the measurement for larger displacements. These are better explained by the 1D-function which was calculated without the small angle-approximation.

Using beads ...lled with ‡uorophores, that are excited by the infrared trapping beam via a two-photon process, and measuring the intensity of the two-photon ‡uorescence simultaneously to the signal on the QPD, provides additional information about the beam focus. From the normalized linescans of the two-photon ‡uorescence intensities (as in ...g. 5-2 on p. 39) the focal dimensions are obtained as $w_{0f} = 0:57$ ¹m and $z_{0f} = 0:64$ ¹m.

Discussion of the position signal

The theory describes the detected signals for small three-dimensional displacements of a trapped sphere within a few percent. The sphere is approximated by a point-like Rayleigh scatterer and only ...rst-order interference is required to explain the measurements for displacements up to the focal dimensions w_0 and z_0 (see ...g. 3 and 4).

The model results in beam-waist radius w_0 and Rayleigh length z_0 corresponding to the values expected for the used objective. For our objective lens with NA 1.3 one calculates a beam-waist radius $w_0 = 0:32$ ¹m and a Rayleigh length $z_0 = 0:55$ ¹m (S. Grill, private communication). Convoluting the expected focus with a sphere of 300 nm radius the model predicts $w_{0f} = 0:48$ ¹m and $z_{0f} = 0:64$ ¹m. The agreement of the focal dimensions obtained from the scattering ($w_0 = 0:46$ ¹m and $z_0 = 0:73$ ¹m) and the two-photon ‡uorescence measurement ($w_{0f} = 0:57$ ¹m and $z_{0f} = 0:64$ ¹m) with these predictions supports the theory.

The detector is more sensitive to lateral displacements than to axial displacements. The lateral signal scales with the ratio of displacement to beam-waist radius: $\frac{\%}{w_0}$, while the axial signal depends on the ratio of displacement to Rayleigh length: $\frac{z}{z_0}$. Even though both are in the range of the wavelength the beam-waist radius is about two- to three times smaller than the Rayleigh length. Therefore, the lateral
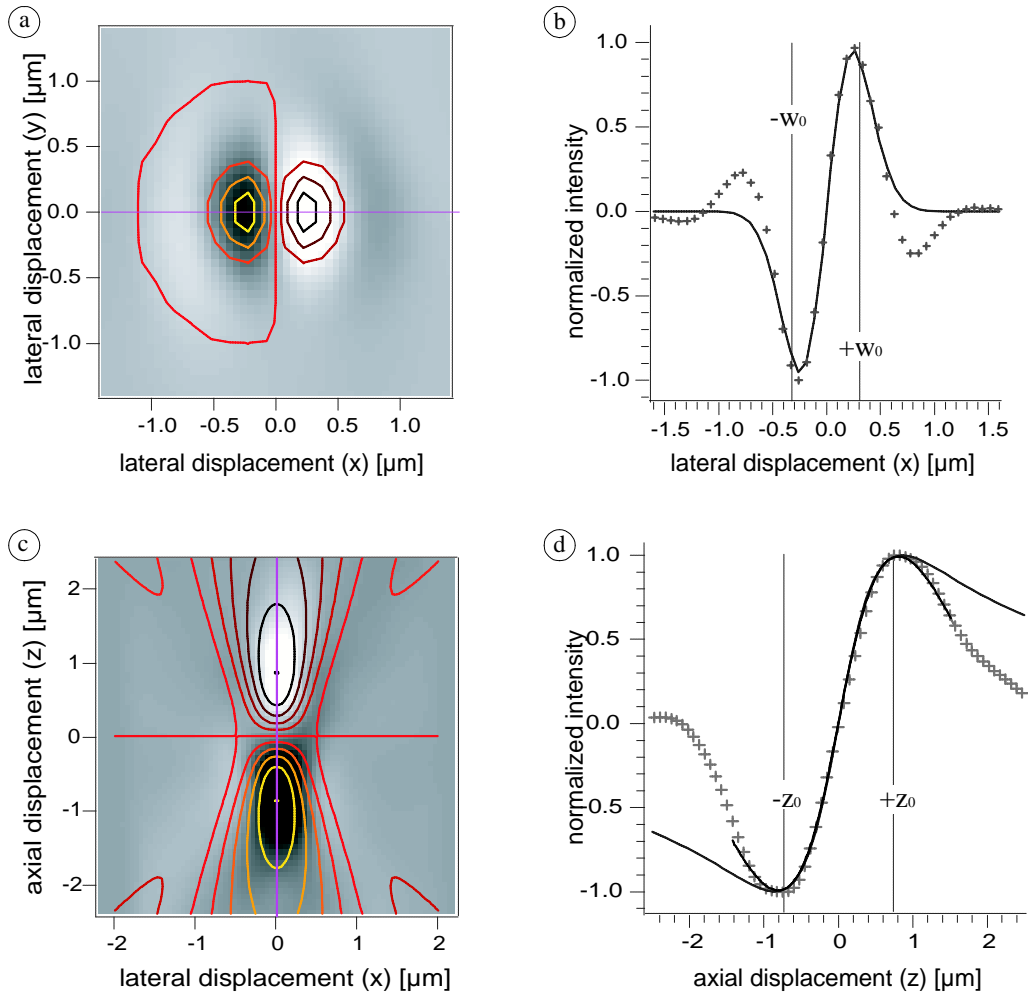
Figure 6-3: The measured response of the QPD when scanning the laser across a sphere (r = 0:3¹m) ...xed to the coverslip. (a) xy-image-plot of the intensities measured in the focal plane. Superimposed are the contours of the ...t obtained using the 3D-function eq.(5.10). (b) Pro...le of the data (+ + +) and the 3D-...t (- - -) taken at zero y-displacement (...t: w_{0x} = 0:33 ¹m). (c) zx-image-plot of the measured intensities. The contours of the ...t obtained using the 3D-function eq.(5.10) for y = 0 are superimposed (...t: w_0 = 0:46 ¹m and z_0 = 0:73 ¹m). (d) Pro...le of the data (+ + +), the 3D-...t (- - -) taken at zero displacement along the optical-axis and the 1D-...t obtained by eq.(5.14) (——).

sensitivity is about three-fold higher than the axial sensitivity. As long as the axial displacement is small compared to the Rayleigh length (z · 150nm) the lateral sensitivity can be assumed to be independent of the axial position, as the resulting underestimation would be smaller than 10%, according to eq.(6.14). The cross-talk between the two lateral directions is larger, according to eq.(6.15). It may be ne-

glected for displacements predominately along one of the axes, but for displacements at 45^0 to the axes the underestimation of the position can reach 30%, if a linear sensitivity is assumed. For larger displacements, the cross-talk and the non-linearities have to be corrected using either this theory or the previously measured detector response. The detector response has to be determined for each particle-size and trapping laser intensity used.

For ideal optics, the sensitivity and characteristics of the detector would be independent of the distance to the coverslip surface. But due to spherical aberrations of the trapping laser beam, the sensitivity of the detector has to be calibrated near the point where it is used. Using the trapping laser as the source for the light scattering provides the advantage that the area of highest sensitivity of the detector is automatically aligned with resting position of the sphere in the trapping potential. The trapping laser provides enough intensity that low-noise detection and ampli...cation is possible. But for small spheres the amount of unscattered light becomes very large. This o¤set has to be subtracted from the signal (eq.(6.3)). In the lateral signal the unscattered light is cancelled out by subtracting the signal of one half of the QPD from the other half. But the o¤set contributes a large part to the total intensity measured as axial position signal. Therefore, the axial position signal is prone to errors induced by laser power ‡uctuations and spherical aberration e¤ects. The quality of the o¤set laser intensity is especially important for small spheres. Because the polarizability and such the scattering cross-section and measured signal depend on the volume of the sphere, the ratio of the signal to the o¤set of non-scattered light decreases with decreasing radius r with r^3.

6.3   Detector calibration

To obtain the positions from the QPD signal, the detector response has to be calibrated. One way is to scan the trapping laser over a ...xed sphere (as done in section 6.2) Because of variations of the size of the spheres and of the laser focus in di¤erent places of the sample chamber, it is desirable to calibrate the detector with the sphere use for an experiment as near as possible to the actual measurement. Measuring in a medium of known viscosity allows to utilize the viscous drag ° to calibrate the detector sensitivity ¯. Assuming a linear detector response for small displacements, Allersma et al. [Allersma et al., 1998] have proposed to use the high-frequency decay of the power spectral density of a Brownian particle in an harmonic potential. The power spectral density A(f) (in units m^2=Hz) is a Lorentz curve whose amplitude decrease for frequencies higher than the corner frequency f_c as 1=f^2 (see sections 5.3.3 and 2, [Reif, 1965]). The sensitivity ¯ (in V olt=m) for a sphere of radius r in a medium of viscosity ´ can be obtained from the voltage spectrum $A^u(f) = ^{-2}A(f)$ (in V olt^2=Hz), without knowledge of the spring constant of the laser trap. The voltage spectrum $A^u(f)$ multiplied by f^2 reaches for f À f_c a plateau P given by

$$P = {}^{-2}\frac{kT}{6\pi^3 \acute{} r}:$$ (6.17)

52

Instead of using the frequency spectrum, it is possible to use the Boltzmann distribution of the positions recorded to determine "voltage" spring-constant κ_v (in units $Nm=Volt^2$ instead of $N=m$) (see section 2.0.3 on p.20) for the position distribution in Volts and the autocorrelation time of the position movements τ. The calibrated trapping potential κ depends on β^{-2}. Because $\gamma = \kappa \tau$ (see section 2 on p.18) and $\kappa = \kappa_v \beta^{-2}$, the sensitivity β is estimated as:

$$\beta^{-2} = \frac{6 \pi \eta r}{\kappa_v \tau}:$$ (6.18)

This is valid for the common case of a sphere in a harmonic potential. As long as the position fluctuations remain within the linear response range of the detector and the viscous drag is not influenced by any surface, it provides a fast in-situ calibration of the detector sensitivity.

Allersma et al. report a discrepancy of 20% between β-values obtained by scanning the laser across a bead on the surface and by analyzing the spectrum according to eq. (6.16). This large discrepancy is most likely caused by the fact, that the trapping position is several hundred nanometers behind the focus, and the sensitivity there is lower. We [Prummer, 1998] have found that the discrepancy is smaller than 8%, if during the measurement on the surface, the laser focus is scanned below the surface, so that the bead is near the trapping position. The position was monitored by the two-photon fluorescence intensity to correspond to the trapping position. A shift of the bead from the geometric focus by about 250nm along the optical axis into the trapping position (see 2-photon signal in fig. 5-2 on p. 39), results in a decrease of the lateral detector sensitivity of 10% − 15% (see eq. 6.14 on p. 47).

Chapter 7

Scanning Photonic Force Microscopy

SFM using a laser trap as force transducer: The single gradient laser trap (section 5 on p. 35) o¤ers a radically di¤erent type of cantilever to build a scanning microscope: a submicrometer sized dielectric particle held by the gradient forces of a highly focused laser beam. A comparison to the classical mechanical cantilever is drawn to scale at the bottom of this page. Such a scanning microscope, introduced into the literature as Photonic Force Microscope (PFM) [Florin et al., 1997], o¤ers several advantages over classical SFM with a mechanical cantilever: First the forces accessible are much smaller, down to Piconewton and below. Second, it is possible to follow vertical slopes fast because of the very small spring constant of the cantilever and its virtually diminishing mass. And third, it allows to image deep narrow trenches and even the inside of translucent three-dimensional objects like cells because the mechanical cantilever arm is replaced by the laser light beam and the pyramidal tip by a sphere. Despite those advantages only little work has been done in this area. In 1993, Gishlain and Webb reported a scanning microscope based on optical tweezers. They scanned several lines on baked photoresist with a trapped, elongated glass particle and reported a lateral resolution of 20nm. Forward scattered laser light provided information about the displacement form the resting position. The resulting contrast is a mix of lateral, axial and rotational signals which complicates the interpretation.

The scanning PFM developed at EMBL to study three-dimensional structures of soft biological materials uses submicrometer ‡uorophore ...lled latex spheres as
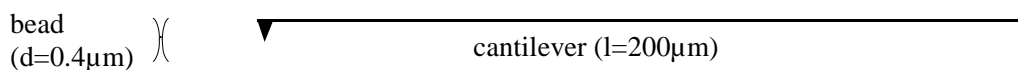
bead (d=0.4μm)   cantilever (l=200μm)

Figure 7-1: Comparison of the scales of the sphere used as probe in the PFM to the typical SFM probe.
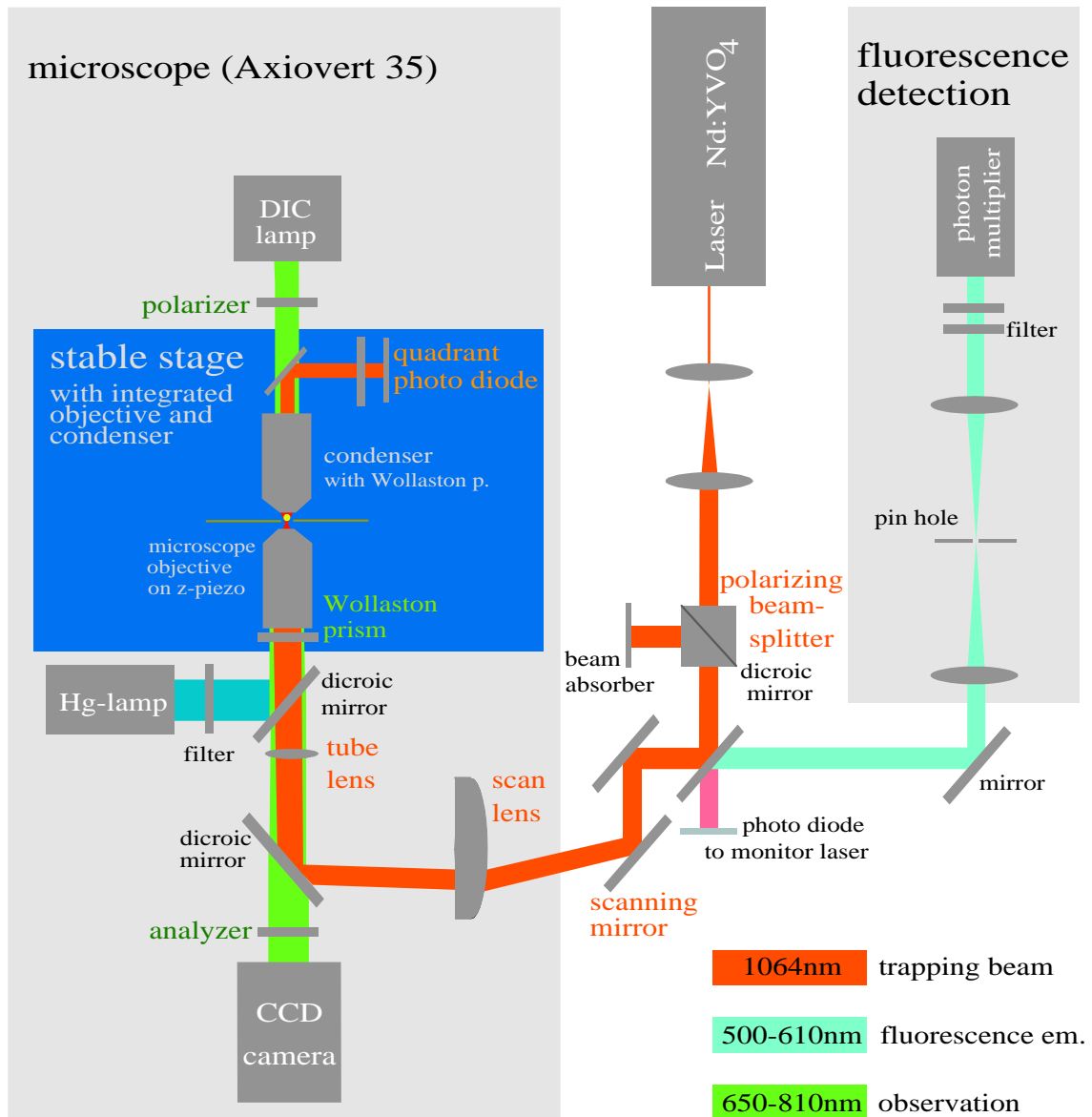
Figure 7-2: Light paths of the PFM built around an inverted microscope with DIC equipment. The expanded IR-laser trapping beam is directed through a polarizing beam splitter via a scanning optic into the backaperture of a oil-immersion objective lens with a high numerical aperture (NA=1.3) mounted on a piezo. The backaperture is over...lled to ensure high trapping e¢ciency. The objective lens generates a di¤raction limited spot in the medium ...lled sample chamber. The dichroic mirrors designed to de‡ect the laser light and a broad spectral range of ‡uorescence accessible by two-photon excitation, is transparent to the DIC illumination (>650 nm), which is chosen to be outside the spectral range of the ‡uorophore and to cause minimal damage to cells. A CCD camera provides a view of the probe as it is moved inside the chamber, and a photomultiplier detects the ‡uorescence emission.

probes and the two-photon ‡uorescence excited in the sphere by the trapping laser as position signal (see section 5.2.1 on p.37). The membrane surfaces of cultured neurons and ...broblasts have been imaged (see section 9.2 on p.69), the elasticity of the plasma membrane measured and the di¤usion and size of membrane proteins in the plasma membrane determined (see section 13 on p.89).

7.1 Design

7.1.1 Optical set-up

The PFM developed at EMBL is based on a laser trap built into an inverted optical microscope complemented with piezo-driven manipulators for the laser beam and the sample stage as well as a three-dimensional detector for the sphere's relative displacement from the trap (details in [Noll, 1997 and Prummer, 1998], photos and details about the materials in the appendix on p. 119). A schematics of the optical set-up of the laser trap as well as the detection systems is outlined in ...gure 7-2. Mechanical units are marked as color blocks.
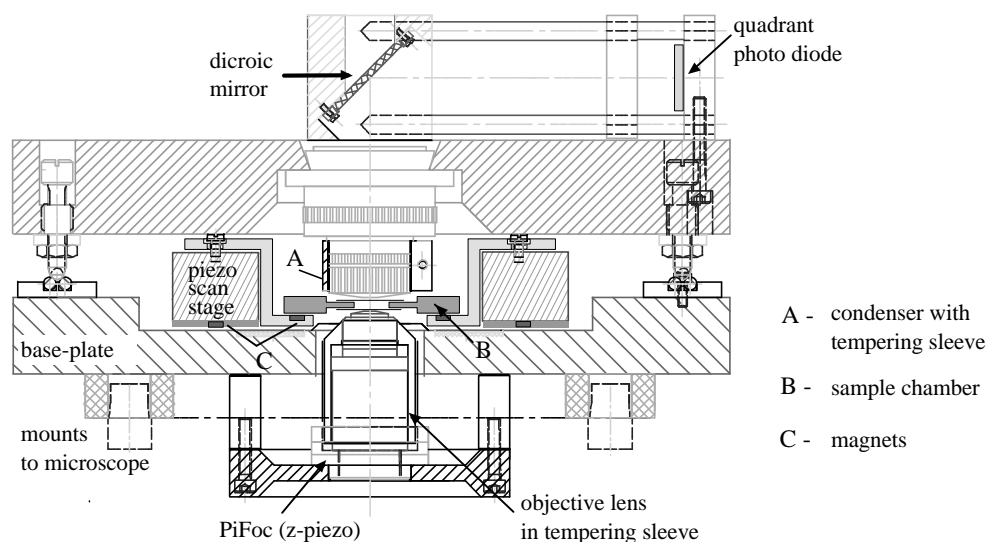

Figure 7-3: Mechanical stable stage integrating the objective lens, sample chamber and position detector (QPD) on one base-plate. The objective lens is moved axially by a piezo (PiFoc, Physik Instrumente, Germany). It is tempered by a coper sleeve. A 100¹m ¤ 100¹m piezo scan stage with capacitive position sensors and digital feed-back (Queensgate, N.Y., USA) rests on the base-plate, held by magnets (C). The aluminum sample chamber (B) whose bottom and top are formed by two coverslips is held in the piezo scan stage by further magnets (C). The condenser lens (A), the dichroic mirror re‡ecting the forward scattered light onto the QPD and the QPF part of the top-plate stitting on a three-point ...t on the base-plate.

7.1.2 Mechanical stability

Measurements of small forces and thermal noise analyses are limited by instrumental noise, mainly mechanical vibrations. Therefore, a considerable e¤ort was taken to create a stable instrument. Originally the laser trap used the microscope's sample stage, but it turned out the this con...guration is not stable enough. A sphere attached to the coverslip on the original microscope stage would show position ‡uctuations of $\hbar xi$ ¼ 15nm. Therefore, a new microscope stage was developed at EMBL. The philosophy is to attach the laser beam focusing objective lens, the sample chamber and the condenser lens with the position detector to one thick main plate minimizing the relative motion of the components (see ...gure 7-3 and photos on p. 119). With this improved stage the position noise is reduced below 1nm (peak-to-peak) and sinusoidal movements of 2nm amplitude of a sphere ...xed to the bottom coverslip are clearly resolved by the QPD in the BFP [data see Prummer, 1998].

7.2 Scanning modes

The scanning modes of the PFM are designed analog to the SFM with some modi...-cations due the speci...c nature of the laser trap: The axial trapping range is limited to about 1^{1}m, but this is o¤set by the ease with which the focus of the laser tweezers can be positioned in space. The ratio of axial to lateral spring constants is less distinct than for Mechanical cantilevers used in SFM have a much weaker axial than lateral spring constant ($k_z : k_x \gg 1 : 100$). In the PFM both spring constants are in the same order of magnitude ($k_z : k_x \gg 1 : 5$) which provides the advantage of less damage to the sample (see section 9.2 on p.69), but also requires a lateral position sensor to be used.

7.2.1 Contact mode

The basic mode is a constant height contact-mode: a sphere is "rolled" over the surface. The sphere trapped in solution away from the surface, is approached to the surface by moving the piezo-mounted microscope objective out o¤ the sample chamber, i.e. downwards (-z). The contact with the surface is monitored by the drop in the measured two-photon ‡uorescence intensity. A pair of scanning mirrors is used to scan the laser and the trapped bead across the surface. Due to the extremely weak axial spring constant of the trap, a protrusion of the surface displaces the bead predominantly along the optical axis, i.e. vertically (+z) away from the surface. The displacement results in a further decrease of the two-photon ‡uorescence intensity. By recording the ‡uorescence intensity an image of the surface topography is acquired. If the bead is displaced too far away from the focus, it escapes the trapping potential. Therefore, the height of the object has to be smaller than the trapping range of the optical tweezer, which is about 1^{1}m. This limitation can be overcome by using a feedback circuit that drives the piezo-mounted objective lens to keep
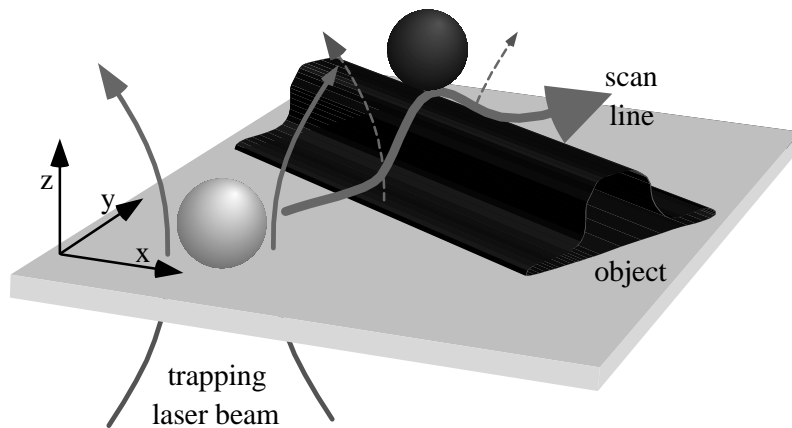
Figure 7-4: In the `constant-height mode`, the sphere trapped by the laser beam is brought into contact with the surface and then "rolled" over the surface along an area of scan lines. The two-photon intensity is recorded detect the axial displacement of the sphere out of the trapping region and measure so the topography of the surface.

the ‡uorescence intensity constant, creating a constant force mode. Because of the large mass of the objective lens and the oil ...lm between objective lens and sample chamber, the applicability of such a feedback is limited. (For acquired images and a discussion see chapter 9.2 on p.69.)

7.2.2 Tapping mode

The tapping mode for the PFM is similar to the force-scan volumes acquired by some SFM researchers [Radmacher et al. 1993]: the laser with the trapped bead is scanned laterally at a distance from the surface. In each image point the surface is approached while recording the two-photon ‡uorescence intensity. When the ‡uorescence intensity decreases below a previously set fraction of the intensity measured for the free sphere, the sphere is retracted again. The tapping mode enables the measurement of virtually vertical slopes as high as the piezo range of the driving piezo, i.e. 100^{1}m. Because the contact times and forces are reduced the spheres are less often lost to non-speci...c adhesion to the cell surface.

The process is controlled via the transputer board by the computer that also displays the image and individual force scans using a Visual Basic program written by Thomas Stefany. The reference ‡uorescence intensity for the free sphere is measured in each point, avoiding image distortion due to bleaching of the sphere and laser intensity variations in the sample plane. The height of the endpoint of each force scan above the coverslip is not constant but depends rather on the imaged topography. The probe is retracted a constant distances from the last contact with the surface, enabling the PFM to climb up extremely steep edge, without the need for extremely long and time-consuming force-scans. The elasticity of the surface is computed from the slope of the two-photon ‡uorescence intensity decrease. Using
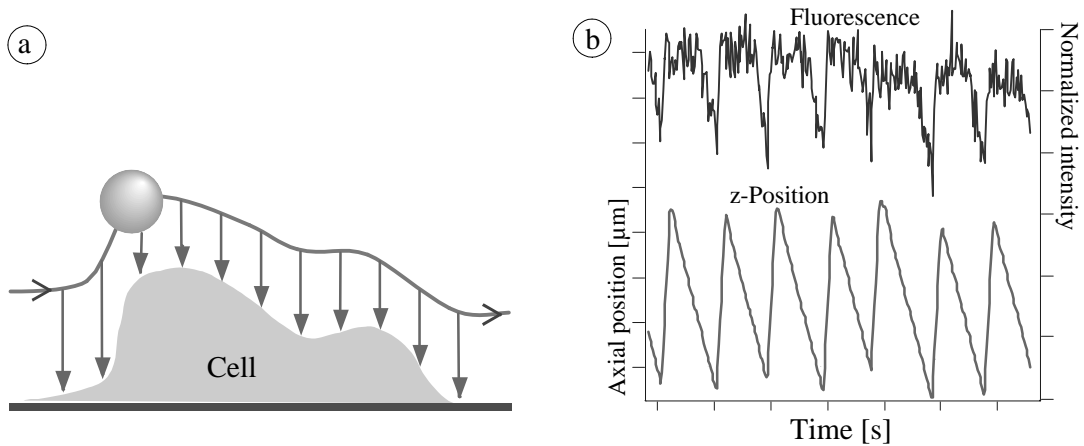
Figure 7-5: In the tapping mode, the sphere trapped by the laser beam is brought repeatedly into contact with the surface. (a) An approach is performed in each image point, then the sphere is retracted a ...xed distance and move to the next image point. (b) The lower trace displays the axial position of the laser focus over time. The upper trace shows the simultaneously recorder two-photon ‡uorescence signal.

the QPD to detect the forward scattered light the lateral displacement of the sphere upon contact can be recorded (Results, see chapter 9.2.2 on p.70).
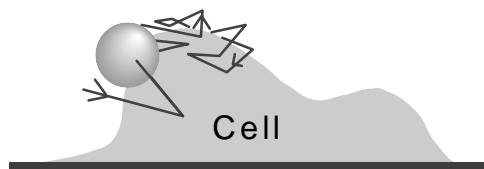
7.2.3   Thermal noise ″scanning″

Figure 7-6: A sphere held in a weak trapping potential samples the volume of the potential randomly through its Brownian motion. Potentials deforming the trapping potential, like repulsive or attractive surfaces, in‡uence the volume sampled. In the case of a repulsive obstruction, the volume not sampled, represents the topography.

Due to thermal excitement a sphere in the weak trapping potential ‡uctuates substantially around its resting position: the RMS thermal position noise in a trapping potential of $2^1 N{=}m$ is 45nm (see section 4.1 on Brownian motion). Any conventional scanning force microscope is limited by the thermal noise because it is impossible to control the position and force of the probe more precisely. Measuring this motion precisely using the forward scattered light a thermal noise ″scanning″ mode can be created: the laser is kept ...xed and the thermal position ‡uctuations of the trapped sphere are recorded. So the free trapping potential is plotted (s chapter 10 on p.75).

Any deviations thereof are due to other interacting potentials or obstructions, like i.e. a surface. An application is the three dimensional particle tracking: a protein in the cellular membrane is tagged with a sphere and its Brownian motion recorded, leaving a "hole" in the volume of the cell, showing points that were never reached by the sphere. (see chapter 10 on p.77)

Chapter 8

Localized diffusion coefficient measurement

The thermal position fluctuations of a sphere trapped in the laser trap can be used to measure the viscosity of the surrounding medium locally (see theory chap. 2). At room temperature a particle trapped with stiffness of $10^{-5}\frac{N}{m}$ to $10^{-6}\frac{N}{m}$ fluctuates with root mean square amplitudes between 20nm to 200nm; respectively. In chap. 13, we have analyzed the thermal position noise to the measure the local diffusion coefficient of membrane proteins. This section covers some of the method and problems encountered on the simpler example of the reduction of the diffusion coefficient due to a spatial confinement.

As discussed already in the theory section (sect. 2.1.1 on p. 21) the viscous drag γ of a sphere near a surface depends on the confinement by the surface and such the distance. Brenner [1965] produced a formula (eq.2.16) to calculate the effective increase of the lateral viscous drag $\gamma_q(z)$:

$$\frac{\gamma_q(z=1)}{\gamma_q(z)} = 1 - \frac{9}{16}\left(\frac{a}{a+z}\right) + \frac{1}{8}\left(\frac{a}{a+z}\right)^3 - \frac{45}{256}\left(\frac{a}{a+z}\right)^4 - \frac{1}{16}\left(\frac{a}{a+z}\right)^5 ; \quad (8.1)$$

but no measurements of the local diffusion coefficient over a range of distances on various surfaces had been done so far. The existing experiments had no three-dimensional control of the probe volume and were often limited to video rate data acquisition (Prieve et al., 1990; Rädler et al. 1992). In those experiments changes in the salt conditions were used to adjust the position of a particle close to a surface. Therefore we have measured the damping of the lateral viscous drag $\gamma_q(z)$ for a sphere while continuously approaching the coverslip surface.

From the theory of Brownian motion in a trapping potential (sect. 2.0.2), the following results and assumptions are used:

- The spring constant k of a harmonic trapping potential $V(r)$ can be measured directly from the position distribution $P(r)$. Because the motion in the trap

is a Gaussian process the position distribution $P(r)$ is Gaussian:

$$P(r) = c \cdot \exp\left[\frac{V(r)}{k_B T}\right], \qquad \text{normalized by } c^{-1} = \frac{1}{r}\int^Z P(r)dr \qquad (8.2)$$

with $P(r)$ being the probability for ...nding the particle at a position in the interval dr. In one dimension, the potential is then

$$V(r) = -kT \, \ln[P(r)]: \qquad (8.3)$$

For a harmonic potential $V(r) = -\frac{1}{2}kr^2$ can determine the spring constant k of the trap.

- The viscous drag $^\circ$ on a Brownian particle in a trapping potential is determined as $^\circ = k_¿$, with $¿$ being the position autocorrelation time.

- To achieve di¤usion coe¢cient measurements with an error smaller than 10% the observation interval $¢t$ has to be about 1200times longer than the auto-correlation time $¿$ (chap. 2.3). Therefore, time intervals of 0:4sec were chosen.

Potential pro...ling and local di¤usion measurement near a surface

Figure 8-1 shows the time-series of the position ‡uctuations of a 0:5¹m-diameter sphere in a trap of sti¤ness $k = 1:6 \cdot 10^{-5}\frac{N}{m}$ about 6¹m away from the coverslip. A magni...cation of the ...rst 2:5ms shows that the measurement frequency lies well under the autocorrelation time, allowing the determination of the autocorrelation time $¿$.

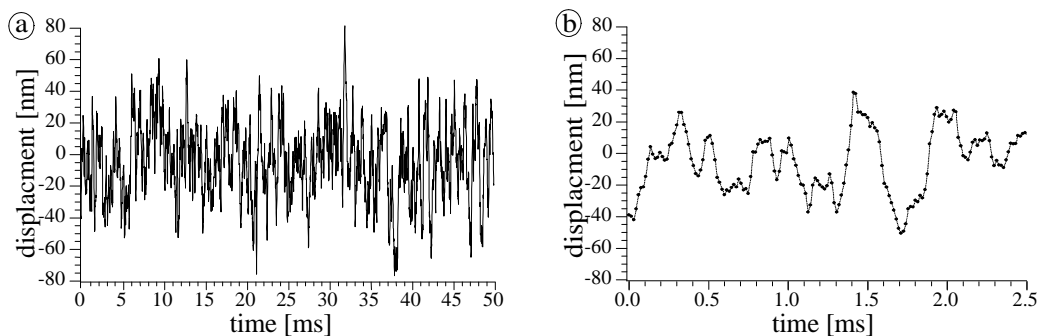Figure 8-1: Time-series of the lateral position ‡uctuations of a 0:5¹m diameter sphere in the trapping potential $k = 16¹N\text{=}m$. (b) The magni...cation of the ...rst 2:5ms of the same time-series shows that the measurement frequency of 40kHz lies well under the autocorrelation time of $¿ = 0:18ms$.

Measuring the autocorrelation-time $¿$ in addition to the trap sti¤ness $\cdot$ provides a way to determine the local viscosity $´$ or di¤usion coe¢cient $D = \frac{k_B T}{^\circ}$ of a sphere
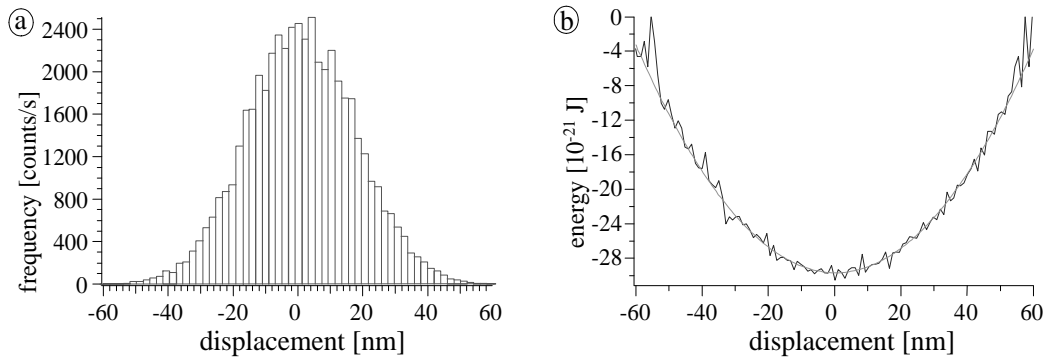
Figure 8-2: Potential pro...ling: (a) probability distribution of the positions of the time series in ...g.7-1. Potential pro...ling: (a) probability distribution of the positions during a 0:4s time interval, (b) energy pro...le of the trapping potential calculated according to eq.(7.3).

in a harmonic potential. The bead in the example in ...gure 8-1 had a spring constant $\cdot$ of $1:6 \cdot 10^{i \, 5} \frac{N}{m}$ and an autocorrelation-time of $\iota = 180^{1}$s, resulting in a viscous drag $^{\circ} = \cdot \iota = 2:9 \cdot 10^{i \, 9} \frac{Ns}{m}$: For a radius $r = 216$nm the viscosity $´ = 0:71$mPas is obtained, which agrees well with the known value for water at room temperature.

The Brownian motion of $0:5^{1}$m polystyrene spheres is recorded at various distances from a surface with nanometer spatial and 25^{1}s temporal resolution. Analyzing time-windows of $0:4$s of the Brownian motion the di¤usion constant and local viscosity are determined. Using $0:5^{1}$m spheres the viscosity can be measured in volumes as small as 1^{1}m^3 with §15% precision within $0:4$s. The autocorrelation-time ι of a $0:5^{1}$m-diameter sphere increases about 27% when it is moved from a sphere-surface distances of about four times its radius to roughly half of its radius. Figure 8-3 displays the corresponding normalized autocorrelation function. The measured positions are 15s apart, so the ...rst two points show distortions due to the limited bandwidth (50kHz) of the analog ampli...er, but otherwise the function falls o¤ smoothly.

In ...gure 8-4 the di¤usion constant of a 1^{1}m-sphere is shown as a function of sphere-surface distance. The decrease of the di¤usion coe¢cient due to the partial con...nement near a surface is measured continuously over sphere-surface separations from 3^{1}m down to 200nm. It is found to agree with Brenner's analytical result. The di¤usion coe¢cient normalized to its bulk value $D_0 = 6:9 \cdot 10^{i \, 13} \frac{m}{s^2}$ remains constant until the distance is in the order of the radius of the sphere. This remains true independent of the diameter of the sphere or the trapping potential, at least for diameters of $0:2^{1}$m $_i$ 1^{1}m and spring constants of $10^{i \, 5} \frac{N}{m}$ $_i$ $10^{i \, 4} \frac{N}{m}$.

63
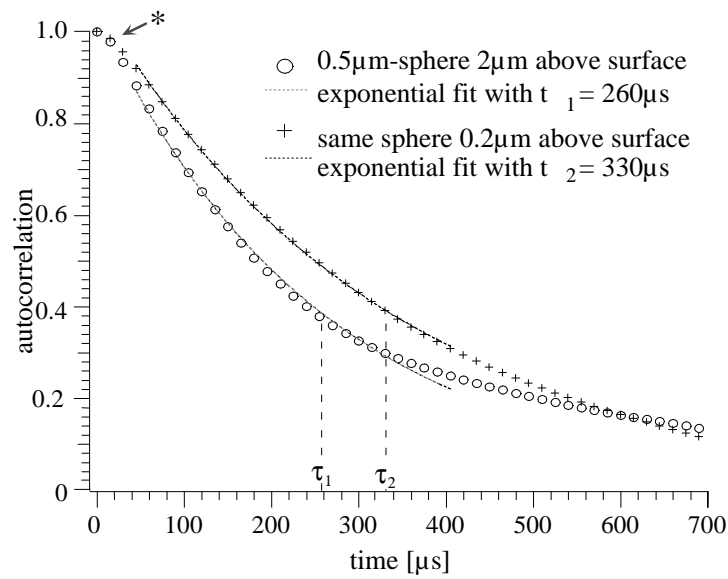
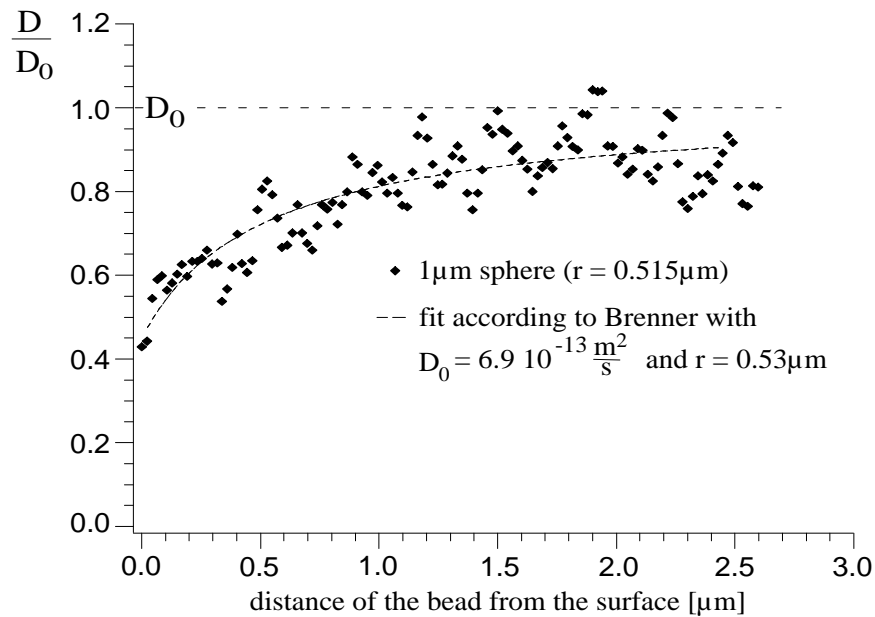Figure 8-3: The autocorrelation functions of a sphere (r=216nm) about 10¢r and r away from a surface.

Figure 8-4: The change in the di¤usion coe₵cient D of a 1-¹m sphere for continuously increasing sphere-surface separation. Each point represents a measurement interval of 0:4s.

Discussion

The measurements performed on glass coverslip surfaces agree with the calculation according to the formula by Brenner [1965]. No difference could be observed for coverslips just rinsed in distilled water or clean with acetone and ethanol. These measurements were performed in distilled water. Studies in buffer containing ions, like phosphate buffered saline (PBS), showed a similar decrease, but the spheres would stick to the surface due to the reduced electrostatic repulsion. Therefore, it was impossible to determine diffusion in the limit of zero separation. Experiments done on BHK-fibroblast and neuronal cells as well as on protein (i.e. fish skin gelatin, FSG) coated coverslips, yielded essentially the same decrease in the diffusion coefficient (data for FSG not shown, for cells see chap. 13). The decrease is independent of the surface approached. Even, the diffusion measured in the limit of contact as monitored by the decrease in two-photon fluorescence varied little: The prediction from Brenner would be 0.33 for z=0. We measured on a clean glass surface a decrease to 0.44, and cells decreases between 0.4 to 0.6. The separation achievable at these distances is determined by electrostatic and other interactions between the sphere and the surface. Therefore, the measured values are larger that the theoretical limit.

Exerting a force onto the sphere normal to the surface increases the measured viscous drag further, indicating the friction between the sphere and the surface that depends on the surface coating and free proteins in the medium. On a clean glass surface the diffusion decreases suddenly, while on protein coated surface a slower decrease is observed. Some results of a study for the case of FSG coated surfaces can be found in the diploma thesis of Prummer (Prummer, 1998). FSG was adsorbed onto the sphere and the coverslip and dissolved in the medium at a concentration of 10mg/ml FSG, a concentration that was used in most measurements on the cells. Applying a force of 16 pN increased the viscous drag about 50%. The effect viscous drag can be expressed as

$$\gamma_{eff} = \gamma + \eta F_N;$$

with the friction coefficient $\eta = 550$ s/m^2. During the measurements of the local diffusion on the cells the force F_N is kept below $0.1pN$, assuming similar values for the friction constant η would lead to a correction of the viscous drag γ smaller than 0.5% which can be ignored.

Part V

Investigation of the Plasma membrane structure

Investigation of the Plasma membrane structure

This part summarizes the information about the cellular membrane obtained with several of the previously described methods.

In chapter 9 imaging studies on the plasma membrane using the SFM and the SPFM are described. The relatively large contact forces in SFM (0.1-0.5nN) made the resolution of the membrane skeleton of living cells possible (sect.9.1). SPFM, due to the considerable lower contact forces ($\gg$0.1pN) allowed to image the bilayer of plasma membrane (sect.9.2). Using the SPFM in tapping mode the virtually vertical sides of living cells could be resolved (sect.9.2.2). Chapter 9 closes with a discussion of the limitations of mechanical scanning microscopy.

A chance to overcome the limitation of mechanical scanning microscopy by the thermal noise is to used the thermal position noise itself as signal. The possibilities of thermal noise scanning and 3D-SPT are presented in chapter 10.

The mechanics of tethering the plasma membrane is described in chapter 11. Variations of the mechanical properties of the membrane in dependence of the location on a hippocampal neuron (sect.11.1.1) and in dependence of the cell type were observed (sect.11.1.2).

Chapter 12 focuses on the dynamics of membrane components in developing neurons using SPT based on video-microscopy. In developing neurons a retrograde ‡ow from the growing neurites onto the cell body could be observed (sect.12.1). In mature neurons, a di¤usion barrier was proposed to exist between the axonal membrane and the cell body. Some di¤usion barriers along the axonal process were found (sect.12.1) but no conclusion could be drawn on the expected barrier between the axon and the cell body.

In chapter 13, the analysis of the thermal position noise of a bead in the PFM was applied to measure the elasticity of the membrane bilayer (sect.13.1) and the local di¤usion coe¢cient of membrane proteins (sect.13.3). The results were used to determine the local viscosity of the lipid bilayer and to show the existence of microdomains as well as to estimate their size (sect.13.3.3).

Chapter 9

Imaging membrane structures

Most of the knowledge about the structure of the membrane skeleton supporting the plasma membrane is based on electron microscopy (EM) performed on ...xed cells [Nicolson et al., 1971; Tsukita and Ishikawa, 1980; Cohen et al., 1980]. In recent years, scanning force microscopy (SFM) has added information on living cells. Due to the relatively large contact forces and the sharp probe used, SFM allows to image submembrane features and to measure elastic properties [Kusumi et al., 1998]. Several studies have applied SFM to investigate the submembrane skeleton of individual cells: cell surface viscosity [Radmacher et al., 1992], cytoskeleton dynamic [Henderson et al., 1992] and virus exocytosis on isolated cells [Häberle et al., 1992] were observed.

These studies have investigated the membrane of individual cells, mostly Erythrocytes. The key component of the membrane skeleton of red blood cells is spectrin, a dimer-forming protein. The meshsize of the spectrin network is de...ned by the size of this dimer as two dimers form the side of a single mesh. It is not clear if this structure is general to all cell types. Evidence has been gathered, that in most cell types the network consists mainly of actin-...laments and proteins that bind actin and regulate actin polymerization.

In order to investigate the membrane skeleton of di¤erentiated and polarized cells, we applied scanning force microscopy to image the apical membrane of Madin-Darby Canine Kidney (MDCK) strain II grown and developing neuronal cells. MDCK cells, a cell line derived from dog kidney, form a epithelial monolayer with structural characteristics and biochemical and biophysical proprieties close to those of epithelia in situ [Rindler et al., 1979]. Investigations on MDCK cells were recently also reported by LeGrimellec and colleagues [1994 and 1998]. Hippocampal neurons are well suited to study the changes to the membrane skeleton during the process of polarization because they can be plated unpolarized into culture and be maintained and studied during the development.
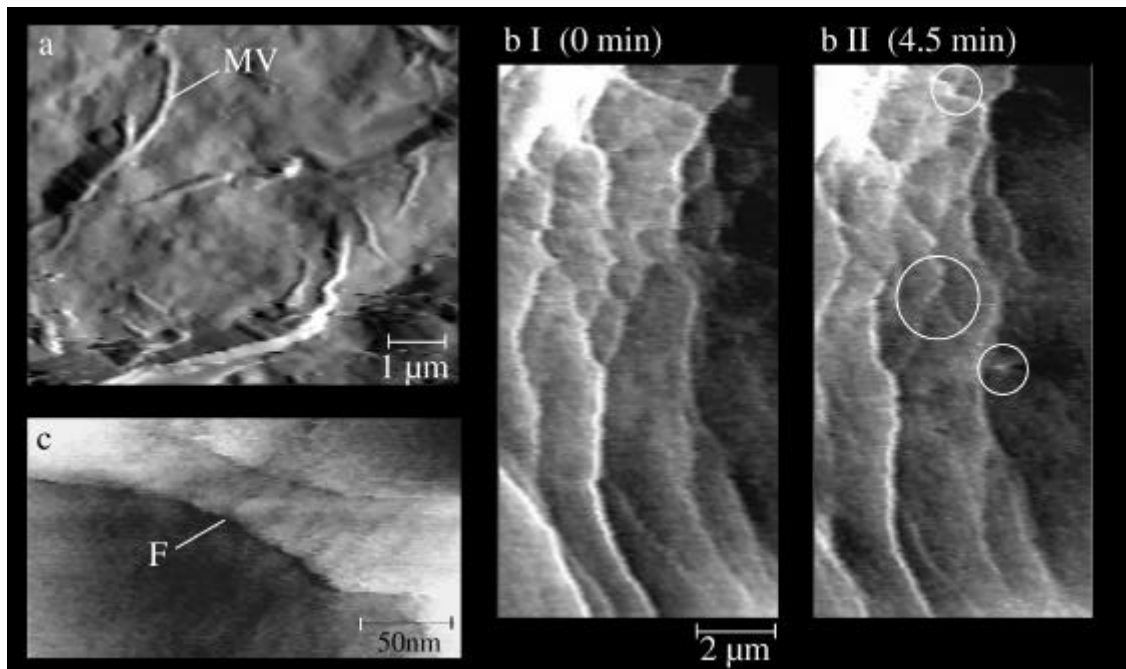
Figure 9-1: SFM scans of the apical plasma membrane of living and ...xed MDCK cells (error signals (chap.3), scan speeds » 10 ¹m/s). (a): Cells prepared in the same way as for EM (...xed in Glutaraldehyde (0.25%), dried and reimmerged in bu¤er (PBS)): collapsed microvilli (MV) are lying on a fairly smooth membrane. (b) and (c): Applying forces between 0.1nN and 1nN a sub-membrane ...lament network is imaged on living cells imaged in culture medium. Increasing the force from 0.1nN to 1nN increases the contrast and number of ...laments visible (not shown). (b) Changes in the ...lament arrangement are observed over 4.5 min. from I to II [» 1nN, 7 ¹m £ 14 ¹m, circles mark some areas of interest]. (c) In some area higher resolution is achieved. This scan shows two parallel and apparently cross-linked ...laments (F) [» 0.2nN, 480nm £ 260nm].

9.1 Examples of SFM on MDCK II and hippocampal neurons

MDCK II cells

Figure 9-1 displays several SFM images obtained of the apical plasma membrane of MDCK cells grown to form a con‡uent monolayer on a glass coverslip. When the cells are prepared in the same way as for EM, i.e. ...xed with Glutaraldehyde (0.25%), dried and then reimmerged in bu¤er (PBS), the SFM images are similar to EM images (...g.9-1(a)): the microvilli, tubular actin-rich cell extensions, collapse on the membrane resulting in a smooth surface with corrugations of a few nanometer. In contrast, on living cells the membrane does not appear smooth but indented between the network of micro...laments (...g.9-1(b) and (c)). In (b) a network of
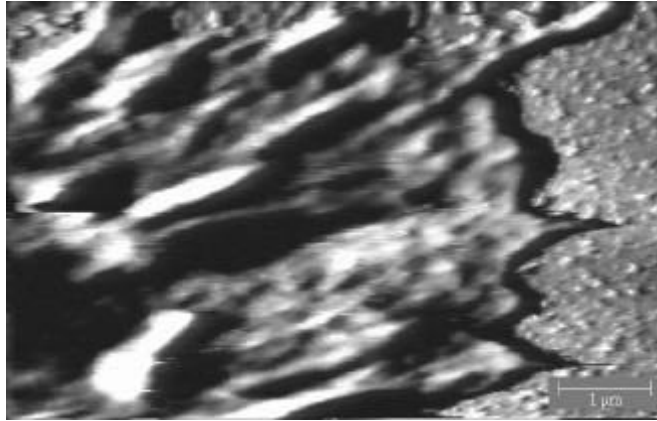
Figure 9-2: SFM image of a growth cone of a hippocampal neuron (4 ¹m£8 ¹m, force. 0.1nN, Glutaraldehyde (0.25%) ...xed, age: 4 d in culture, imaged in PBS).

...laments is visible. Increasing the contact force (0.1nN-1nN) improves the contrast and raises the number of visible ...laments (not shown). The slow changes of the network over time are shown in (bI) and (bII) (¢t=4.5min). Figure 9-1(c) is an example of small area scan with a resolution down to several ten nanometers. In this image, two ...laments appear to run parallel for about 150nm and to be cross linked in regular spaces.

This resolution is the exception. Images of living cells are mostly cloudy and the resolution is not better than about hundred nanometers (data not shown). The limitation is most likely caused by a dense glycocalyx, i.e. oligosaccharides on the extracellular side of the membrane. Digesting the sugar coat by various enzymes like neuroamidase and hyaluronase have resulted only small improvements because of the broad variety of sugars involved [LeGrimellec, private com. and 1998]. The microvilli imaged on the ...xed cells, are invisible on living cells because they are pushed aside by the SFM stylus as their lateral sti¤ness is smaller than the one of the cantilever. Their elasticity should be similar to the elasticity of the stereocilia of hair cells in the inner ear (0.5-5mN/m for guinea pig [Langer, 1998]).

The dimensions of the network of micro...laments in ...g.9-1(b) agree with the spacing between the "fences" proposed by Kusumi in the "membrane-fence model" [see introduction on p. 1.2; Kusumi et al., 1993; Sako and Kusumi, 1995]. The dimensions of the structure in ...g.9-1(c) are compatible with a model of two actin ...laments cross-bridged by ®-actinin [Alberts et al., 1994]. These examples show the potential of SFM to image sub-membrane structures and dynamics.

The growth cone of a hippocampal neuron

The growth cone is situated at the distal end of each neurite of a hippocampal neuron. In light microscopic images it appears ‡at with a number of radial ...laments, that immuno‡uorescence microscopy has shown to contain actin. It is a very

dynamic structure. Studies with ‡uorescently labelled vesicles from the Golgi have shown that newly synthesized membrane is transported speci...cally to the growth cones (sect. 1.2).

SFM imaging of a growth cone (...g. 9-2) was only possible at lowest contact forces (. 0.1nN). Scanning with higher force destroyed the structure or removed the cells from the coverslip. The growth cone surface appears ‡at, except for some radial streaks. Large image distortions along the scan direction are visible at the edge of the structure: the mechanical cantilever with the pyramidal tip is not able to follow the topography.

These images are examples for the possibilities and limits of SFM. In the ideal situation, if the surface is not obscured by a dense glycocalyx, information about the structure of the submembrane ...laments can be obtained at a resolution of 20nm. But, structures with steep edge cause large image distortion. Also the membrane itself is not imaged, but pressed on the submembrane structures. This is deduced from the fact, that increasing the contact force increases the contrast and number of ...laments visible.

Therefore, to image the lipid membrane itself, the scanning photonic force microscope was developed: a polystyrene bead trapped in laser tweezers. It has an adjustable vertical spring constant from 0:1pN/m to 5pN/m. In addition the lateral spring constant is only about 3- to 5-fold the vertical spring constant, which reduces the damage done during scanning. With the proper manipulation device it is possible to image surfaces at any angle in space, i.e. vertical and highly curved surfaces, and in principle any transparent 3D structure.

9.2 Photonic force microscopy on hippocampal neurons and BHK cells

9.2.1 Contact mode topography of neurites

Here it is shown, that the photonic force microscope using a trapped polystyrene sphere provides a method to image the "soft" plasma membrane bilayer and the steep edges of axonal processes. A bead trapped by the laser tweezers is "rolled" in contact over the glass surface while the ‡uorescence intensity is recorded (for the various scan-modes see section 7.2 on p. 55).

Figure 9-3 shows the branching processes in a culture of 3 day old rat hippocampal neurons. Part (a) displays a di¤erential interference contrast (DIC) overview (42¹m £ 42¹m).The faster growing major process (M) of the neuron that will eventually become the axon contains several branching points (B). Especially near the branching points are numerous small neurites (N) that are potential starting points of new neurite branches. Figure 9-3(b) displays a zoomed DIC image (7¹m £ 7¹m) of this area. The scanned area is indicated in Fig. 9-3(b) by a white frame. Scanning probe images Figure 9-3(c) shows the surface recorded with the PFM. The

small neurite, barely visible in the DIC image, can be easily seen in the scanning probe image (the signal to noise ratio is at least one order of magnitude higher) and in addition the scanning probe image shows an actual height contrast. The small neurite is of constant width and height across the whole scanning range.

The height pro...le shown in Fig. 9-3(d) is a convolution of the topology of the neurite and the geometry of the bead. The height calculated as the di¤erence between the baseline and the maximum is 400nm. Measuring the width of the object is complicated by the width of the bead, as long as the height of the object is larger than radius of the bead. We can estimate the minimal width of the small neurite from the ‡at plateau on top (94 nm, see A in Fig. 9-3(d)). This width together with the bead diameter (216 nm) add up to 310 nm, which is the minimal width we should measure at the baseline. This agrees very well with the measured value of 405 nm (see B in Fig. 9-3(d)). If we neglect other contributions to the image formation process (e.g. crosstalk between the lateral and the axial position signal), the data ...ts to a simple geometrical model of a trapezoid with 94 nm width on top and 189 nm at the base.

The height of the small neurite is therefore about three times larger than its width. In a SFM image one would expect for such a structure major distortions of the height pro...le in Fig. 9-3(d), due to the steep increase to the top within about 40 nm on both sides. Such distortions should depend on the scanning direction and the scanning speed. From the symmetric height pro...les along the small neurite we conclude, that the PFM allows to resolve the true structure of such steep objects.

The peak to peak roughness at the baseline is approximately 40 nm, which is in good agreement with the resolution calculated from photon statistics.

The small neurites are at the beginning of potentially new neuritic branches. They contain microtubule bundles and cortical actin. Although there is only little data about these neurites, it was observed, that they often grow on top of each other for longer distances (Bradke, personal com.). This observation together with the mechanical sti¤ness of the cytoskeleton (microtubules and actin) of the neurites explains the threefold higher vertical extension observed. We calculate the sti¤ness of our optical trap to be about $5\,^1N{=}m$, resulting in a maximal force applied to the neurite of $5\,pN$. Because this force is very small compared to e.g. speci...c interaction between ligands and receptors and also compared to unspeci...c interaction , even faintest adhesion forces cause the bead to adhere to the interacting surface. Two of these events actually occurred during the image recording process and are very well visible as singular events in the surface plot.

9.2.2   PFM tapping mode topography imaging of BHK cells

To overcome the limited dynamic range along the optical axis and to reduce the reaction from the cell by reducing the contact time, a tapping mode (TM) for the PFM was developed. In each point of the image, the reference ‡uorescence intensity of a free bead is measured. The bead is then brought into contact with the surface until the ‡uorescence intensity has decreased a preset fraction (chap. 7.2).
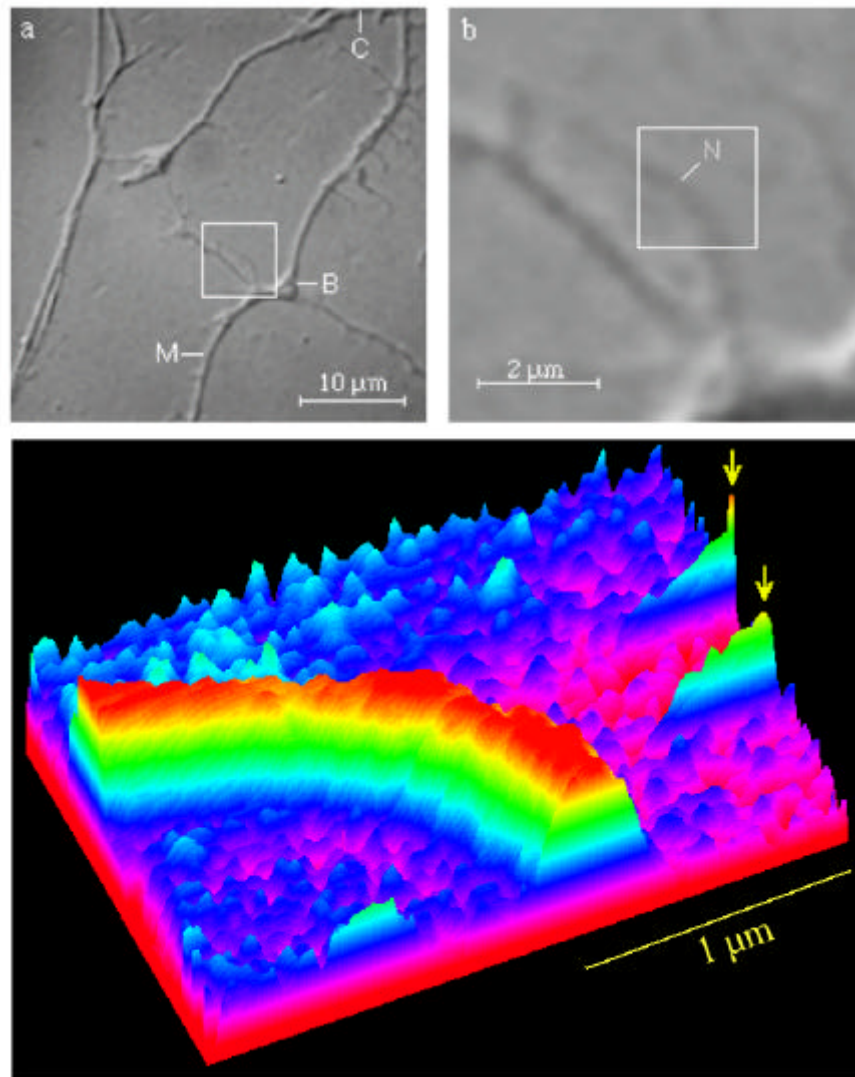
Figure 9-3: PFM image of a neurite recorded at 2W laser power (¼ 300mW intensity in the focal plane). For a trapped 0.2 ¹m-bead, this intensity results in 250 photons counted per 1 ms integration time. The image (64x64 pixels) was recorded within 30sec. The ‡uorescence intensity was converted into a height signal by a calibration factor obtained by pressing the trapped bead against the lower cover slip and measuring the ‡uorescence intensity decrease (100mV decrease corresponds to an axial displacement of 228nm). The lateral force constant was measured from the distribution of the thermally excited positions in the trapping potential to be $3:3 \notin 10^{i\, 5} N=m$. (Arrows mark artifacts caused by adhesion.)

(a) DIC image of BHK cell
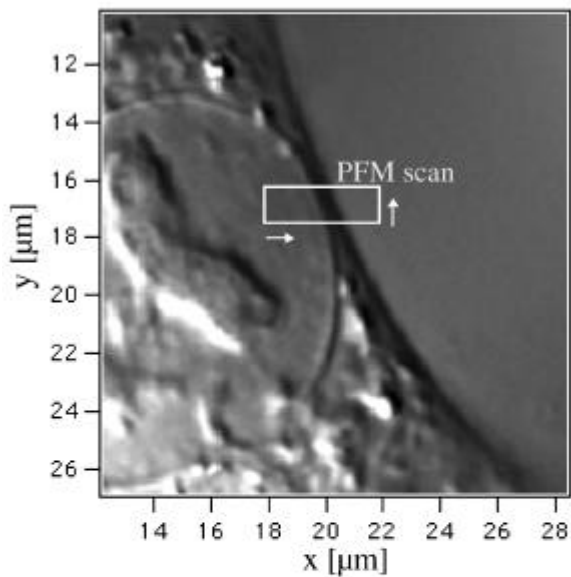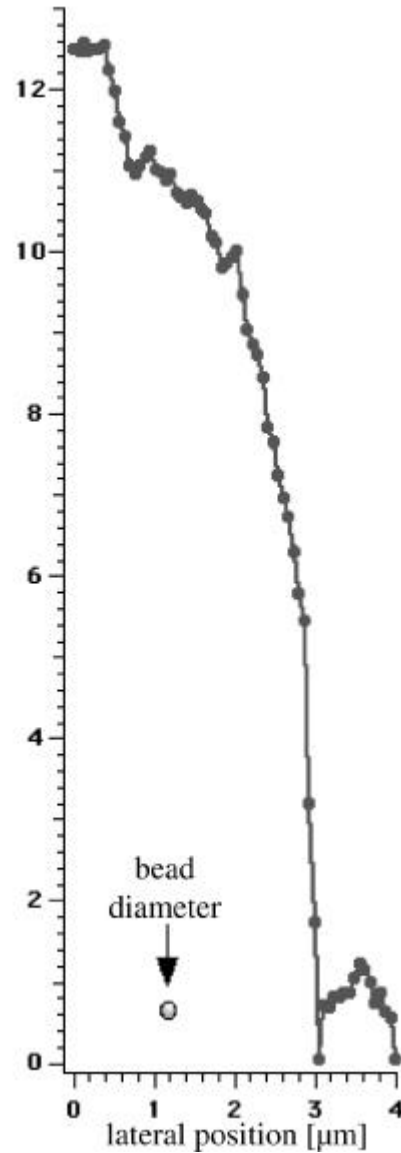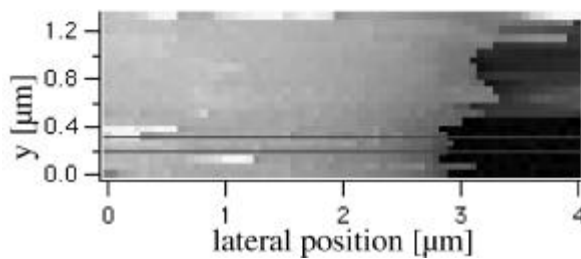
(b) PFM scan at edge of nucleus

bead diameter

Figure 9-4: Tapping mode (TM) allows imaging of steep edges: (a) DIC image of central area of a BHK cell. At the left, the nucleus is visible as circular structure, to the right is the free coverslip. The focal plan is in the middle of the cell. (b) PFM scan as indicated in (a) (scan from left to right and bottom to top in (a)), elevated areas are bright. (c) Line scan between the two lines in (b). Each dot represents one approach and retract cycle.

Figure 9-4 displays the TM-PFM image of the edge of a nucleus of a BHK ...broblast cell. The DIC microscopy picture (a) focuses in the middle of the cell, neither the upper surface nor the coverslip is in focus. The circular structure on the left is the nucleus of the cell. In part (b) a TM-PFM scan of the central region is shown, in which two lines mark the row taken for the line scan on the right. This

example demonstrates the imaging of extremely steep edges with a high dynamic range, in this example 12¹m, in principle only limited by the piezo used (100¹m in our instrument). Here the advantage of using light as cantilever beam is obvious: a mechanical lever arm would get in the way by touching the cell before the probe would and the large surface would result in an increased viscous drag and decrease the axial speed possible. The cell absorbs and distorts the IR-trapping beam very little: the measured two-photon ‡uorescence intensity of the sphere above the cell is only reduce by a few percent from the signal measure above a free area of the coverslip. In the line scan each point, 62:5nm apart, represents the endpoint of a force-scan, indicating that the sphere is guided along the almost vertical slope without any distortions. The simultaneously recorded lateral position signals from the QPD show only minimal lateral displacements out of the optical axis. The drop of the ‡uorescence intensity that triggered the retraction of the sphere was set to 30%, which corresponds to a axial displacement of about 200nm out of trap and 1pN (k = 5¹N=m). At these forces, the cell surface appears smooth down to the resolution limit of several tens of nanometers, given by photon statistic and thermal position noise. It is interesting to note that the nucleus indeed has a spherical shape of about 12¹m diameter, reaching far above the rest of the cell.

9.3 Limitations of mechanical scanning microscopy to study the cellular membrane organization

While mechanical scanning microscopy provides potentially high topographic contrast and informations on the mechanical properties of the investigated surface, the mechanical interaction between sample and probe causes disturbance of both signals. On a soft and especially a living sample, the probe can introduce severe deformations and changes. Even forces as little as 20 pN caused the growth cones of neurons to be indented hundred nanometers, corresponding to a elasticity of 200¹N=m for the growth cone. The spring constant of the membrane bilayer between the membrane skeleton is even smaller ((1 ¡ 5¹N=m), chap. 13). The spring constants of the weakest cantilevers use in SFM are comparable to the elasticity of the entire growth cone and several orders of magnitude larger than the membrane elasticity, so that the membrane bilayer is always indented between the underlying membrane skeleton elements.

Through the interaction the spring constant of the probe k_p is coupled to the one of the sample k_s, resulting in the overall spring constant:

$$\frac{1}{k} = \frac{1}{k_s + k_p}$$

Therefore, matching the compliance of the probe to the spring constant of the sample is desirable [Burnham, 1994]. While this involves changing the cantilever in an SFM, reaching from k_p = 0:1 mN=m to 10 mN=m, it is easily achieved by adjusting the

laser power in the PFM, at least for k_p from $0.5 \, \mu N/m$ up to $10 \, \mu N/m$.

The force regime of the PFM o¤ers compliance matching for cellular membranes. Using the PFM with spring constants of roughly $k_p = 1 \, \mu N/m$ (s. above), the plasma membrane appears smooth, indicating that the beads do not indent the bilayer. Because of the large thermal ‡uctuations of systems with such a small spring constant, the extreme ‡exibility of the membrane bilayer in the order of $1 \, \mu N/m$ prevents high lateral resolution imaging on cell surfaces. Only areas of the membrane reinforced by the cytoskeleton or a high protein concentration provide enough stability for high resolution SFM. The study of the gap junction by Hoh and colleagues [1993] and work by Schneider et al. [1997] are examples of higher resolution achieved in reinforced membrane areas. A living cell also reacts to the stimulus on its surface. Using the PFM it was observed that $0.1 \, \mu m$ ¡ $0.2 \, \mu m$ latex spheres are endocytosed by some cells.

A further limitation in scanning microscopy is the temporal resolution: the probe can only be guided over the sample with a limited speed resulting often in several minutes recording time per image. This acquisition rate is too slow to visualize the dynamic processes of cells: some reorganization of the membrane cytoskeleton might be observable, but the dynamics on the molecular scale is too fast. In addition, most molecules are not bound tightly enough to exclude thermal position ‡uctuations. The membrane itself ‡uctuates thermally with an amplitude of about 100nm (s. chap. 13.1). The absence of speci…c markers poses further limitations to the interpretation of topographic images. In some studies antibody coated colloid gold particles were used, but the natural abundance of spherical structures on the plasma membranes also limits this approach.

Chapter 10

Thermal noise imaging and 3D single-particle tracking

Precise positioning and a low contact force, i.e. low spring constant $\cdot$, are mutually exclusive because any object at temperature T undergoes Brownian position ‡uctuations with the mean square amplitude $\overline{r^2} = \frac{k_B T}{\cdot}$ (see theory sect. 2.0.2). So a further decrease of the compliance of the system leads to an increased position uncertainty. But if instead of aiming for a precise positioning, the position is just measured fast and precise enough to resolve the thermal position ‡uctuations, these ‡uctuations provide a valuable signal. In the simplest case they are just used as a random scanning procedure and the probability for each position is recorded. An image of these probabilities yields information on the con…nement of the probe by surfaces and potentials. This section shows an example of imaging by thermal noise (see …g. 10-2). If the motion is con…ned in a three dimensional harmonic potential, then the spring constant of the potential and the viscous drag on the probe can be measured (sect. 2.0.2). This method will be applied in chapter 13 to measure the local di¤usion of cell membrane components.

The use of the thermal noise as signal requires only are a precise position sensor and an instrument set-up to minimize all other noise sources, i.e. mechanical and electronic noise, that could obscure the thermal position ‡uctuations.

Three-dimensional laser trapping potential

Here, the e¤ect of a perturbation to the 3-dimensional trapping potential of the laser trap is discussed. In …gure 10-1(a) the positions reached by a $0{:}2^1$m diameter sphere trapped in the laser trap far from any surface are shown as an energy surface representation. The surface plotted represents the distance from the lowest point of the trapping potential that a particle with a certain amount of energy $^®k_B T$ can reach. It is also a position probability because in the potential the thermal energy transferred to the particle result in position ‡uctuations. Most of the time, the bead in 10-1(a) will be in the enclosed volume because its thermal ‡uctuations are smaller. When the trapping potential is brought in overlap with another structure, the shape
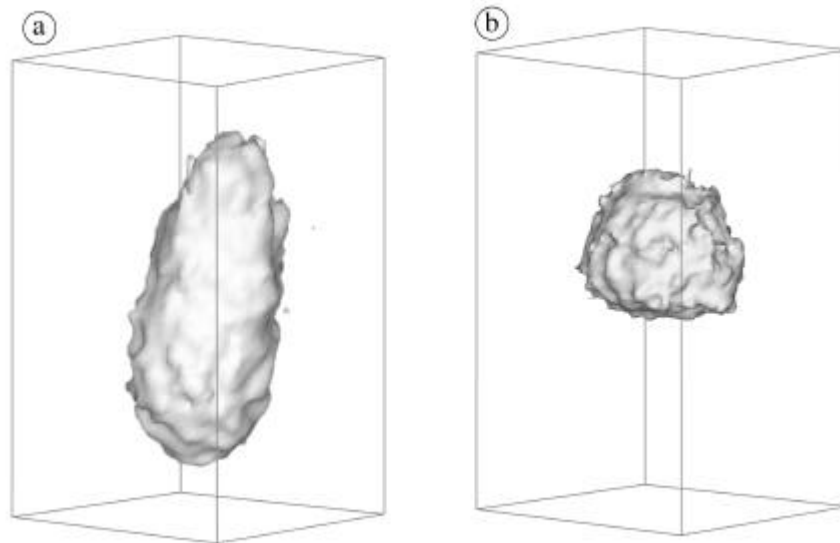
Figure 10-1: Isosurface representations enclosing the positions reached by a sphere undergoing thermal position ‡uctuations during a 0.5sec time interval in the laser trap: (a) far from any surface and (b) being held on top of the plasma membrane of a BHK cell. (see suppl. video for a timeseries)

of the volume is changed. In part (b) of the ...gure the center of the potential is close to the plasma membrane of a BHK cell. Therefore, the sphere cannot sample the bottom part of the image.

3D-SPT on neurite membrane

The random sampling of the trapping volume provides a way to extend the classical video-microscopy based single-particle tracking (SPT) (s. above) to three dimensions and signi...cantly higher temporal resolution. Figure 10-2 displays the three-dimensional tracking of a Thy1.1 molecule di¤using in the membrane of a hippocampal neuron. The tubular outline of the neurite is clearly visible as the molecule is di¤using around it. Subtracting the diameter of the sphere form the dimensions of the "tunnel" yield a diameter of about 200nm - 300nm for the neurite. So using 3D-SPT it is possible to track the actual motion of the membrane component over the curved cell surface at 20¹s temporal resolution. Conventional 2D-SPT based on video-microscopy is inadequate for such a study, because the loss of the axial position and the low temporal resolution of 25Hz. The loss of spatial information becomes apparent by just drawing the 2D projection of the track (...g. 10-2(c)). The 2D-video projection converts tracks up and down on the side of the neurite into areas of high probability and apparent con...nement (lower right in ...g. 10-2(c)), which would lead to inadequate interpretations. The importance of the

high temporal resolution becomes apparent when the tracks are overlaid at reduced temporal resolution (...g. 10-2(d)). A membrane protein with a di¤usion coe₵cient of about $D = 1 \cdot 10^{-10} \frac{cm^2}{s}$ would move in an area of about $(200nm)^2$ around its
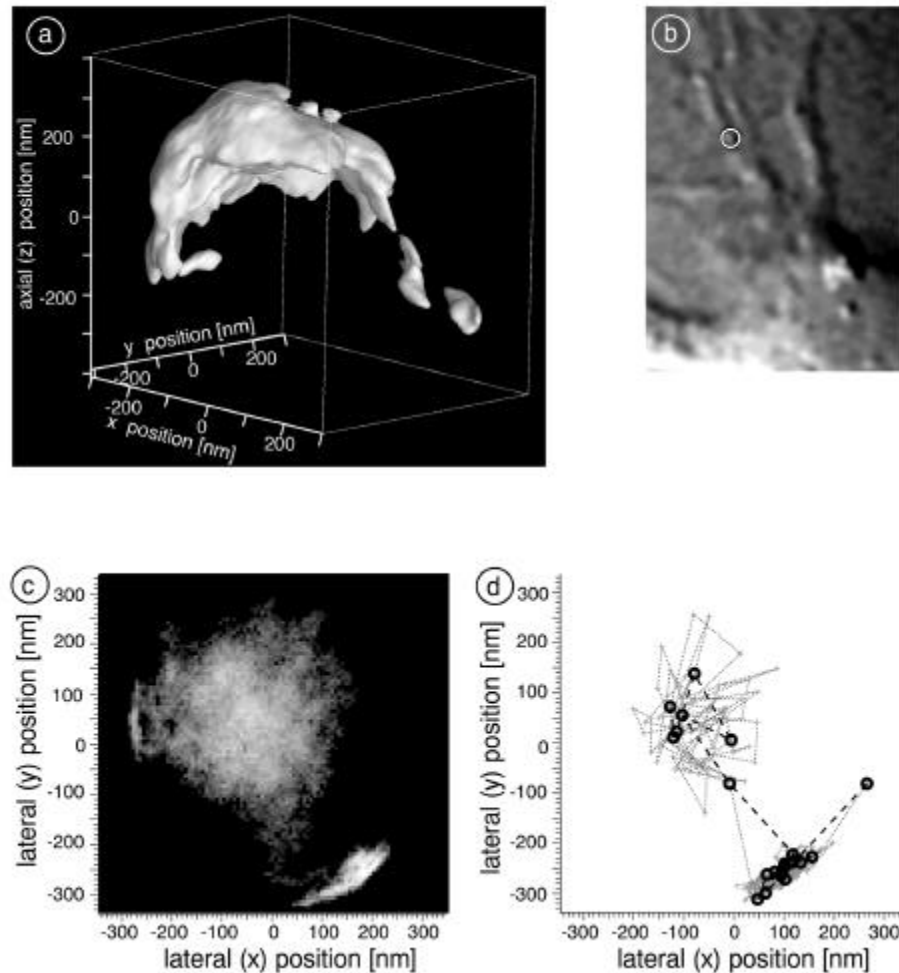

Figure 10-2: 3D-SPT of a Thy1.1 molecule di¤using around a neurite. (a) Surface representation of the volume in which the sphere has been di¤using during 85% of the time. A 0.2 ¹m-sphere was bound to the Thy1.1 molecule via an antibody. The position was measured every 20 ¹s over a period of 42 s resulting in $2:1 \cdot 10^6$ data points. (b) DIC-view of the bead (marked by the white circle) on the cell. For comparison with video-microscopy based 2D-SPT the probabilities of the positions reached in the ...rst 840 ms are shown in (c) as two-dimensional projection. (d) Same data at reduced temporal resolution: with 4 ms (+++) resolution, and at normal video-camera speed (40 ms, ooo).

origin in two subsequent video image (25 fps). Because several hundred position measurements are needed for a precise di¤usion estimate, a di¤usion coe₵cient determined by conventional 2D-SPT based on video-microscopy is an underestimation and represents more the shape of the cell and the density of obstacles to the di¤usion in the membrane than the characteristics of the individual molecule.

This example demonstrates the importance of the third dimension and the high temporal resolution (i.e. 20 ¹s) provided by 3D-SPT to obtain meaningful data on the di¤usion coe₵cient. Because of the size of the neurite of about 0:2 ¹m in diameter, the measured positions have to be deconvoluted with the detector response function (see chapter 2.2.2. on the detector response), and the in‡uence of the weak potential of the optical trap has to be accounted for.

Therefore, instead of following the molecule over the cell with 3D-SPT to measure the di¤usion of individual membrane proteins (chap. 13), the 3D-SPT was combined with con...ning the sampled volume by trapping the probe in the laser tweezer. This provides the further advantages of increased speed of the measurement because of the reduced autocorrelation time in a potential (see sect. 2.0.2). The localized measurement also eliminates the need for a deconvolution of detector artifacts, cell shapes and interactions with immobile obstacles in the plasma membrane. This method is applied in chapter 13 to study the di¤usion and size of membrane microdomains.

Chapter 11

Membrane mechanics

11.1 Biophysical properties studied by tethering of the cell membrane

The surface area of the plasma membrane providing the cell with a stable boundary, needs to be constantly readjusted due to endo- and exocytosis as well as cell growth. It is assumed that the cell surface is one continuum. It remains unclear how the cell regulates the membrane area and tension. To study the interaction of the lipid membrane bilayer and the underlying cytoskeleton, a series of "tethering" experiments was performed. "Tethers", highly curved membrane cylinders, are easily extracted from arti...cial vesicles [Waugh et al., 1982], red blood cells [Hochmuth et al., 1982] and neuronal cells [Dai and Sheetz, 1995].

We have used laser tweezers and beads coated to bind the ganglioside GM1 to extract lipid tethers from developing hippocampal neurons. The force needed to extract tethers in this cell type is less than 10pN and the tethers can grow up to a length of 70-100μm (see suppl. video for examples). Growing neuronal cells are well suited to study the membrane economy because they have functionally specialized areas that can be easily recognized and accessed in a light microscope and are constantly adding newly synthesized membrane at the growth cone (Craig and Banker, 1995; see also introduction on p.8).

Forces determining tethering of the membrane

The forces resisting the tether formation and elongation can be separated in a speed v dependent, a length l dependent part and an o¤set or holding force F_0:

$$F = F_0 + 2\pi \eta \cdot v + k \cdot l: \tag{11.1}$$

Our measurements support the ...nding of Dai and Sheetz (1995), that the length dependent spring constant is negligible, unless parts of the cytoskeleton are pulled into the tether. If cytoskeleton ...laments were pulled into the tether, its length was limited to a few micrometers and the tether was laterally sti¤er. These tethers
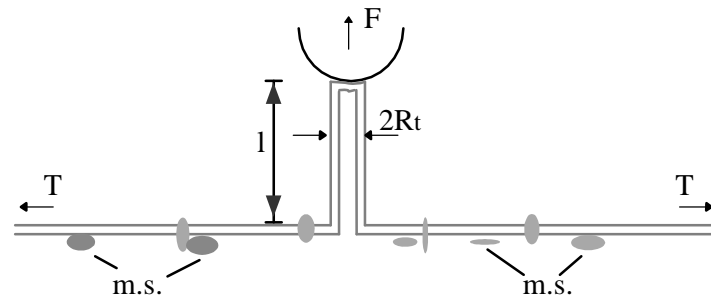
Figure 11-1: Schematics of extracting a tether with radius R_t from a bilayer by pulling an attached sphere with force F and speed v. The counteracting force is caused by the adhesion of the bilayer to components of the membrane skeleton (m:s:), the viscous drag around these, the bending of the membrane and the "far-…eld tension" T.

appeared rigid when moving the sphere side ways parallel to the membrane surface, while the normal tether would undulate like a string. The three components of the tethering forces can be attributed to the following: the adhesion of the membrane to the supporting structure and the bending of the membrane into a tubular structure F_0, the inherent viscous drag within the membrane and of the membrane against the cytoskeleton $°$ and the elastic stretching of some parts of the supporting structure k. In 1996, Hochmuth et al. have developed a model to describe the tethering process in the absence of any elastic contribution.

They have attributed the o¤set F_0 to the bending of the membrane into a tubular extension of radius R_t, the "far-…eld in-plane membrane tension" T, and the adhesion g of the membrane bilayer onto the membrane skeleton (see …g. 11-1):

$$F_0 = 2¼R_t\,(T\ + g) + \frac{¼B}{R_t}; \qquad\qquad (11.2)$$

with B being the membrane bending modulus [Hochmuth et al., 1996]. A constant radius R_t can be related directly to the tension and adhesion term $F_0 = 4¼R_t(T + °)$. From DIC-microscopy, the radius of the tether is estimated to be 100-300nm. But because the radius is so small, DIC-microscopy really only allows relative measurement of tether radii.

The contributions to the viscous drag are assumed to be the sliding of the two bilayers against each other $´_{si}$, their intrinsic viscosity $´_m$ and their ‡ow past the membrane-skeleton and transmembrane proteins $´_{sc}$ [Hochmuth et al., 1996]:

$$° = 2\,´_m + ´_{si}h^2 \ln (R_0=R_t) + ´_{sc}R_t^2 \ln (R_0=R_t)\,; \qquad\qquad (11.3)$$

with R_0 being the radius of the vesicle or cell that is tethered, and h the membrane thickness.

11.1.1 Tethering forces in hippocampal neurons

At the time, these experiments gave only a qualitative description due to a limited position control of the laser trap relative to the cell. To pull the tethers a DC-motor driven sample stage was operated in short ($70\,\mu s$) pulses to achieve the required speeds in the range of micrometers per second. To measure the exerted pulling forces, the positions of the $0.5\,\mu m$-diameter bead in the trap ($k = 0.3 \pm 0.05\,mN/m$) was recorded by video microscopy and tracked using the tracking-program described in the SPT section (see suppl. video). The beads used for these experiments were coated with the binding subunit of Choleratoxin which binds to the ganglioside GM_1 (see appendix).

Tethering forces are lowest at the growth cone

Depending on the location on a single cell, we ...nd variations in the visco-elastic parameters: The e¤ective viscous drag η is lowest at the cell body ($0.5 \pm 0.1\,\mu Ns/m$) and greatest at the growth cone and along the neurite ($1.3 \pm 0.2\,\mu Ns/m$). In successive tether extractions, the viscosity decreases rapidly. In these experiments, a tether was pulled to about $10\text{-}15\,\mu m$ length. Then the tether was released and allowed to retract. After it had been fully reabsorbed by the cell (no visible tether, the bead was back in the starting position), one minute was waited before the next pull commenced. Within four or ...ve extractions using the same sphere the apparent viscosity would decrease to $\gg 50\%$.

   The largest variation over the cell surface was found in the holding force F_0. It was lower in the distal areas of the cell than at the soma itself: at the growth cone about 2pN versus 7pN on the soma. In 1995, Dai and Sheetz have also reported that the holding force F_0 along the neurite of the dorsal root ganglion decreases from the cell body to the growth cone.

   Most the times, no signi...cant elastic contributions were measured. When elastic forces were measured, they contributing less than 10% to the total force. Long interaction times (in the range of a few minutes) between the bead and the membrane before tether extraction and repeated extractions of the same tether increased the occurrence of elastic forces.

Tethers slide along the surface

Once a tether was formed, it aligned vertically to the cellular surface to minimize the bending energy. It could be moved over the cellular surface with sub-Piconewton forces. Sometimes it stuck to some obstacle, but raising the force to a few Piconewtons let it slide free. On hippocampal neurons up to 12 days old, the tethers were freely moved from one neurite over the soma into another neurite. No indication of a barrier could be observed [see video].

Discussion

Using the thermal position fluctuations of a transmembrane protein an effective in-plane membrane viscosity of $0.1\,\mathrm{Pa\,s}$ was measured for BHK cells (see chapter 13.3). Assuming a similar value for the neuronal membrane and a membrane thickness of 5nm, the two-dimensional sheet viscosity η_m would be about $0.5\,\mathrm{nN\,s/m}$. Applying eq. (11.3) to describe the effective viscosity η, then the contribution of the intrinsic membrane viscosity $2\eta_m \gg 1\,\mathrm{nN\,s/m}$ to the measured $0.5 - 1\,\mu\mathrm{N\,s/m}$ is negligible. The interbilayer slip viscous drag $\eta_{si}h^2 \ln(R_0/R_t)$ was measured by Evans and Young [1994] in vesicles to be between 0.007 and $0.069\,\mu\mathrm{N\,s/m}$ depending on the lipids used to make the vesicles. So the main contribution to the viscous drag of the tether extraction in neuronal cells is caused by $\eta_{sc}R_t^2\ln(R_0/R_t)$, the viscous flow around immobile obstacles and along the cytoskeleton. Therefore, the local variations might represent a varying degree of coupling of membrane proteins to the cytoskeleton. This could also explain the reduction of the viscous drag in successive pulls.

Using eq. (11.2) the low holding force F_0 measured at the growth cone, indicates that the adhesion between the plasma membrane and the membrane skeleton is lowest at the growth cone. The membrane appears to be "stretched tighter" over the membrane skeleton near the cell body than at the growth cone. Dai and Sheetz have speculated that this could be driving of the retrograde flow of membrane on neurites that we and other have observed (sect. 12.1).

Elastic contribution were rarely measured and if observed, they occurred in short tethers. Long interaction times of the spheres with the membrane surface increased the occurrence of elastic forces. This suggests that they arise from non-specific interaction of the sphere with membrane proteins that are bound to the cytoskeleton. Longer interaction times increase the non-specific adsorption [Altmann, 1998]. In an experiment using rat-IgG coated beads we have observed elastic contributions to the force in about 50% of the extracted tethers, indicating that indeed cytoskeleton filaments cause the elastic forces. Also, hepatocytes treated with nocadozole, an actin severing drug, show no elastic contribution in their tether formation (see sect.11.1.2).

11.1.2 Connection between the cell membrane and supporting cytoskeleton varies between cell types

We had observed that the phospholipid bilayer of the neuronal cells can move quite freely in respect to the supporting membrane cytoskeleton. To investigate whether this is a general property of the cell membrane also in non-neuronal cells, membrane tethering experiments were performed on rat pancreatic acinar, hepatocytes and erythrocytes, and the influence of the cytoskeleton depolymerizing drugs cytochalasin B and Taxol.

Pancreatic acinar cells and hepatocytes were freshly isolated from male rats. A few erythrocytes remained in these preparations. A detailed description of the cell preparation can be found in Jena et al., 1991. The washed cells were plated on Cell-

Tak-coated glass cover slips. To impose an external force onto the plasma membrane, we used $0.5 \mu m$ diameter carboxylmodi…ed-latex spheres (Molecular Probes, actual diameter 431nm § 2:8%), which adsorb readily proteins. The forces applied during these experiments were around 100 ¡ 120pN. These forces were neither su¢cient to indent the plasma membrane nor to pull tethers of the hepatocytes and acinar cells. Contrary, erythrocytes were easily tethered with these forces. After incubating the acinar cells for 30 min. in $20 \mu M$ cytochalasin B, a microtubule severing drug, tethers could be formed. But in contrast to the situation in neurons and the erythrocytes the tether were laterally sti¤: it was possible to turn the cells around its anchoring point on the coverslip using the tether as handle. This indicated that the tether contained cytoskeleton elements. Even after the cytochalasin treatment the membrane could not be indented. After a 30 min. treatment with $20 \mu M$ Taxol, an actin severing and microtubule stabilizing drug, it was not possible to form tethers on the acinar cells, but the plasma membrane could be indented visibly.

Even those studies were not quantized, they showed qualitative variations between the cell types: the association of the lipid membrane to the underlying cytoskeleton in neurons and erythrocytes is weak, so that tethering is possible. In acinar cells tethering is only possible after depolymerizing the actin …laments of the membrane skeleton.

Chapter 12

Membrane protein dynamics in neurons

The membrane domains of polarized cells, such as epithelial and neuronal cells, have speci...c protein and lipid compositions. In the case of epithelia these are created by sorted delivery and maintained by the tight junctions as a di¤usional barrier (see sect.1.2). Similar mechanisms are expected to exist in mature polarized neurons. It has been shown that the growth of neuronal cells is localized at the distal end of the neurites. Studies with ‡uorescent labelled vesicles from the Golgi have shown that newly synthesized membrane is transported speci...cally to the growth cones [Craig et al., 1995]. Also it is known that the polarized distribution of membrane proteins is achieved by sorted delivery [Ledesma et al., 1998]. However it is not clear whether a barrier to di¤usion exists in the plasma membrane at the axonal hillock; the connection between the axon and the soma. In 1992, Kobayashi et al. transfected the axonal membrane domain of polarized neurons with labeled virus. A di¤usion of the label into the somato-dendritic domain was not observed. In contrast, Winkler and Poo [1996] have shown that a lipid dye di¤uses freely between the axonal membrane and the soma. Therefore, this chapter focuses on the dynamics of membrane proteins in developing hippocampal neurons to study the mechanisms maintaining a polarized membrane protein distribution.

12.1 Macroscopic domains in hippocampal neurons studied by SPT

To investigate the proposed di¤usional barrier at the axonal hillock and study the membrane dynamics of developing neurons, the di¤usion of lipids and proteins in the plasma membrane of growing hippocampal neurons was studied using SPT.

To measure the ‡ow of lipids, beads were bound to either the endogenous ganglioside GM_1 or to the lipid DHPE (dihexadecanoyl-phosphatidylethanolamine) which was inserted into the plasma membrane. Polystyrene spheres with 0.2^1m-diameter were used because colloid gold particles (d=40nm) were endocytosed by the cells
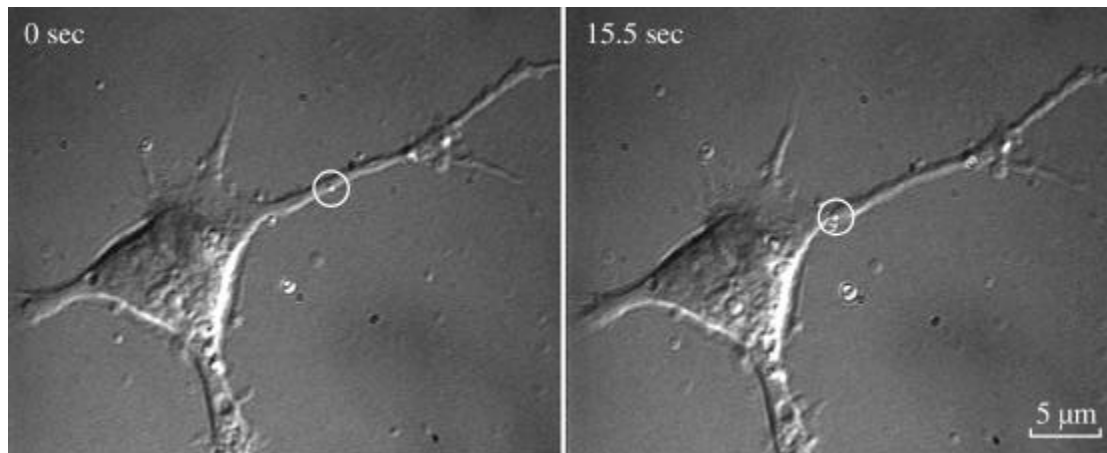
Figure 12-1: GM_1 bound sphere on 2d old hippocampal neuron.(s. suppl. video)

within minutes. To study the motion of GM_1 the binding fragment of Choleratoxin (ChTx B-frag.) was used. Biotinylated ChTx B-frag. was bound via Strepta-vidin to spheres coated with biotinylated BSA (see appendix A.1). To insert the lipid fluorescein-DHPE (Molecular Probes, Leiden, The Netherlands) into the cell membrane, the cells were incubated with 10^1g/ml fluorescein-DHPE at $37^{\pm}$C for 30 minutes. Anti-fluorescein antibodies were bound to the spheres via protein A (see appendix A.1).

As examples for the diffusion of proteins, the GPI-anchored protein Thy1.1 which is predominantly found in the axon, and the transmembrane transferrin receptor (TrfR) which is transcytosed by the neurons and found on the entire cell, were used. For both a commercially available monoclonal antibody (mAb; suppliers see appendix A.2) was bound to the beads via protein A. The density of the linkers on the sphere was kept low (5-20 molecules per bead), so that only a single membrane protein could be bound.

The resulting binding probabilities were extremely small: Holding the spheres with the laser trap for about 10s onto the membrane, about 15% of the lipid-binding spheres would bind, in the case of the proteins the probability was about 5%. Anti-Thy1.1 beads would bind preferentially on just one neurite of the cells. This agrees with the fact that Thy1.1 is mainly expressed on the surface of the axon.

In the following, the diffusion and mobility in very young cells, about 2 days in culture, is compared to the dynamics in maturing cells, about 9-13 days in culture.

Retrograde flow of lipids and membrane proteins in young cells

In the young (1-2 d old) hippocampal neurons, GM_1 bound beads diffused ret-rogradely onto the cell body at about 15 ¡ 35^1m/min (...gure 12-1). Diffusion from the soma back into one of the neurites was never observed in this work. This agrees with the observation of Craig et al. [1995] and Dai and Sheetz [1995] that newly

synthesized membrane is inserted at the growth cone and then di¤uses back toward the cell body.

In older but still maturing cells ($\gg 9$ days) lipids or proteins di¤used randomly. In about 20% of the cells, a retrograde ‡ow at about half the speed of the young cells was observed but the spheres never di¤used onto the cell body.

If the spheres were moved across the cell surface actively, using the laser tweezers adjusted to a lateral sti¤ness of $10 ¡ 50^1$N/m, the spheres could be pushed from one neurite onto the cell body and from the cell body onto a di¤erent neurite in a few cases, but typically the spheres became immobilized near the cell body. This happened in varying places and a direct cause for this hinderance could not be determined.

A possible reason is the steep increase in cell height in that area: the neurites are less than 1^1m high, whereas the cell body extends up $5-10^1$m (known from PFM and SFM imaging experiments, see chap.9). Therefore, tracing the membrane surface while moving the bead with the laser tweezers exerts additional force onto the membrane causing the sphere to become eventually immobilized. This immobilization does not have to be caused by a speci…c binding as even adsorption of a cytoskeleton bound membrane protein to the sphere would result in binding much stronger than the maximal tweezer force used ($\gg 10$pN, see sect. 9.2). Automated surface tracking could possibly allow to move a protein bound sphere greater distances across the cell surface because the interaction times and forces with other membrane components would be reduced. This would decreases the probability of unspeci…c adsorption [Altmann, 1998].

Barriers to free di¤usion in maturing cells

In two maturing neurons (11days old) obstacles to free di¤usion of Thy1.1 were encountered on the major neurite near the cell body. Spheres bound to Thy1.1 would move freely between these barriers but not across them (see …gure 12-2). Using the laser trap at maximal forces of 10pN, the spheres could be moved between the "lines". However it was impossible to push a sphere across the "line" from either side. No obstacles outside the cell were visible in the microscope. But whether this con…nement is speci…c to Thy1.1 and at which developmental stage of the cell it appears, could not be determined due to the rareness of the observation.

Summary of SPT di¤usion coeⅭcients and discussion

The following table summarizes the di¤usion coeⅭcients obtained for the various lipid and protein probes on developing hippocampal neurons. The age of the neurons in cell culture is given in days since plating in culture. The coeⅭcients were calculated from the …rst 1:5s of the mean-square displacement plots. The errors are
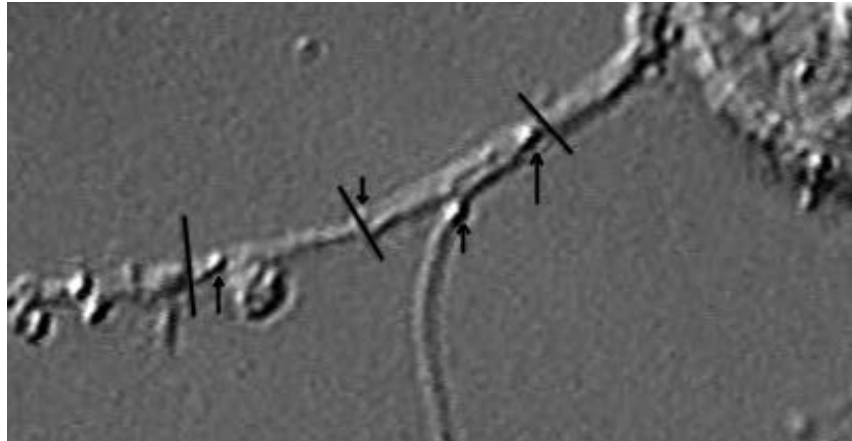
Figure 12-2: Barriers to the free di¤usion of Thy1.1 (lines), which could not be crossed by the beads (arrows). Between the lines the beads di¤used freely and could easily be moved by the trap. But the areas marked could not be crossed from either side. (age of neuron 11d ; s. suppl. video)

the maximal deviations from the mean.

lipids: GM$_1$ (ChTx) and PE (Ab)	$D = (21 \pm 6) \times 10^{-10}$ cm^2/s	(n=21)
GPI-an. protein: Thy1.1 (mAb)	$D = (15 \pm 14) \times 10^{-10}$ cm^2/s	(n=5)
transmembrane pr.: TrfR (mAb)	$D = (12 \pm 5) \times 10^{-10}$ cm^2/s	(n=7)

The measurements for the lipid probes, GM$_1$ and PE, were combined because no di¤erence could be observed. Also the data taken on cells of all ages from 3 to 13 days did not exhibit signi...cant variations. The spheres coated with antibodies against the proteins TrfR and Thy1.1 did not bind well to the cells. The TrfR di¤used about two-fold slower than the lipids. Binding to Thy1.1 was only observed in more mature cells (10-13 days).

Recently Ledesma et al., 1998, have shown that in mature neurons the GPI-anchor of Thy1.1 is found in DIGs while in immature cells Thy1.1 is detergent soluble. The large spread seen in the di¤usion coe¢cients measured for the Thy1.1 molecule could be caused by partial association to DIGs. But at this stage, it is pure speculation because of the low number of measurements and the limited resolution of video-based SPT. The measurements are averages of traces extending several micrometers across the cell surface and around the sides of the neurites. Therefore, inhomogeneities in the cell surface in‡uence the di¤usion measurement more than the size of the protein. Because of the two-dimensional projection, the lateral motion on the sides of the neurite are ignored. This results in an underestimation of the di¤usion coe¢cient (see 3D-SPT in sect. 10). The measured di¤usion coe¢cients agree well with previously published data on ...broblasts [Jacobson et al. 1997], but are one to two orders of magnitude too small to agree with the Sa¤man-Delbrück

theory of diffusion in a lipid bilayer (see section 2.2.1). Saxton [1987, 1989b] has shown that this discrepancy could be caused by the interaction with immobile and mobile obstacles along the path of diffusion.

The temporal resolution of video-tracking is too low to separate effects due to the size of the protein from effects due to the remainder of the membrane. Only localized diffusion measurements in a confined area without immobile obstacles performed with high temporal resolution promises to resolve the dependence of the diffusion coefficient on the characteristics of the molecule. To determine the size of the diffusing molecule from the diffusion coefficient, a localized diffusion measurements in a confined area without immobile obstacles performed with high temporal resolution ($\Delta t < 0.1ms$) would be required.

Such a technique was developed in this thesis work, the local diffusion of membrane proteins was measured by applying 3D-SPT in the PFM. The next section will focus on the characterization of membrane microdomains by such local diffusion measurements.

Chapter 13

Local environment of membrane proteins studied by thermal noise analysis and local diffusion measurement

There is a large discrepancy between the diffusion coefficients of proteins in the cell membrane measured by SPT (previous chapter) [Jacobson et al., 1987; Kusumi et al., 1993] and the ones predicted by the Saffman-Delbrück theory of diffusion in a lipid bilayer [sect.2.2.1; Saffman and Delbrück, 1975] and measured in artificial lipid bilayers [Jacobson et al., 1981]. Two possible reasons have been discussed and investigated in the literature: interaction of the diffusing protein with immobile and mobile obstacles along the path of diffusion [Saxton, 1987 and 1989b] and transient confinement of transmembrane proteins by the membrane skeleton [Kusumi et al., 1993; Sako and Kusumi, 1994]. However, at the local scale each membrane protein could still be surrounded by enough homogenous fluid lipid bilayer that its diffusion would be described correctly by the Saffman-Delbrück equation (eq.2.18 in sect. 2.2.1). Therefore, a method to measure the diffusion locally in a confined area of 100-150nm diameter by 3D-SPT in the PFM was developed (see section 8 on p.59) and applied to several membrane proteins.

The local diffusion measurements were used to address the existence of membrane microdomains in the cell membrane of intact cells. Membrane microdomains enriched in glycosphingolipids and glycosylphosphatidylinositol (GPI)-anchored proteins ("rafts") have been implicated in polarized sorting and cellular signalling (see sect.1.2 on page 8). The fate of these microdomains upon arrival in the plasma membrane is unclear, but recent findings indicate that they remain as one unit [Harder et al. 1998; Varma and Mayor, 1998; Friedrichson and Kurzchalia, 1998]. To study these detergent-insoluble glycolipid-enriched domains (DIGs), the viscous drag on a raft associated protein and on a non-raft transmembrane protein were measured.

Sections 13.0.1 and 13.0.2 describe the conceptional model behind this approach, the proteins used and the measurement procedure. The results that are independent

of the membrane protein used, such as the increased drag on the probes in the vicinity of the membrane and the measured membrane elasticity, are discussed in sections 13.1 and 13.1. Section 13.2 describes the observations made concerning the binding to the membrane proteins. The observed di¤erences between the viscous damping caused by the raft and non-raft membrane proteins are summarized in section 13.3. The results are then interpreted using the Sa¤man-Delbück theory (sect.13.3.3), and discussed in the light of previous measurements (sect.13.4).

13.0.1   Concept and materials

To probe living cells for lipid microdomains and to estimate their stability and size, the local di¤usion coe₵cients of microdomain associated GPI-anchored and transmembrane proteins in BHK cells were measured and compared to the di¤usion of a non-raft transmembrane protein. Two assumptions were made, and later supported by the experimental results: First, the direct environment of each membrane protein constitutes mainly a ‡uid lipid membrane, in which the proteins di¤use according to the Sa¤man-Delbrück theory (see sect. 2.2.1). Second, the microdomains are assumed su₵ciently rigid, so that only the di¤usion of the complex is measured and not the di¤usion of the individual protein within the microdomain. Under these conditions, the viscous drag imposed by the lipids on the protein should be a measure of the size of its transmembrane domain, or an estimate for the size of the microdomain, as appropriated.

Since the …rst assumption is not ful…lled on the scale of micrometers in the plasma membrane [Jacobson et al. 1997; Saxton 1987, 1989b], a local measurement of the viscous drag is necessary. The mean distance between membrane proteins in oocytes was measured by freeze-fracture EM to be 53nm [Eskandri et al., 1998]. In 1989, Saxton and Owicki had reported a mean distance of 6.3nm for rhodopsin in the rod outer segment. This extremely high protein density is probably due to the specialized function of this area in collecting light. In …broblasts the protein density are probably more like in oocytes. Therefore, the viscous drag measurements where localized to a region smaller than 130nm in diameter. Because of the fast di¤usion of membrane proteins in arti…cial lipid bilayers (10^i $^8cm^2$=s) [Jacobson et al., 1981], autocorrelation times of the spheres in the potential of the PFM of about 1ms were expected (sect.2.0.2). Therefore, a temporal resolution of $t < 0.1ms$ is required.

The local viscous drag of the following proteins was measured by 3D-SPT in the PFM: the transferrin receptor as a transmembrane non-raft protein, compared to the in‡uenza virus hemagglutinin as a transmembrane raft-associated protein and the placental alkaline phosphatase as a GPI-anchored raft-associated protein. The next sections characterize the molecular biology of these proteins.

Transferrin receptor - a transmembrane non-raft-protein   Transferrin is the major iron carrier protein in vertebrates and is required for the maintenance of cell viability. To deliver the iron, transferrin binds to the transferrin receptor (TrfR), the complex associates with clathrin on the cytoplasmic side and is internalized

via clathrin coated pits. The TrfR is a transmembrane glycoprotein composed of two disul...de-bonded subunits of about 90kD each. Each subunit contains a single transmembrane domain of 26 amino acids, an ectodomain of 672 residues and a cytoplasmic domain of 62 amino acids [Schneider, 1985]. Miller et al. [1991] have observed that the human TrfR promotes the formation of ‡at clathrin lattices, before these form invaginations. The TrfR does not interact with DIGs and is excluded when HA or PLAP-DIGs are clustered [Harder et al., 1998].

For the measurements of the membrane viscosity a construct of the human TrfR with a shortened cytoplasmic tail (TrfR-¢t; Harder, EMBL) was used. The amino acids 5-41, containing the endocytosis signal, were deleted. This left 25 amino acids on the cytoplasmic side of the protein before the transmembrane domain (63-88aa). This truncated version is not endocytosed and does not interact with the clathrin coated pits [Harder, pers. com.].

The human TrfR-¢t was transiently expressed in BHK cells. The overexpression level estimated from immuno‡uorescence images was high. So that initially a dimerization of the human-TrfR-¢t with the endogenous TrfR was expected to be unlikely. Unfortunately, no stable cell line could be obtained. The stably expressing clones grew only slowly and died soon. Thus, it had to be assumed that the non-endocytosable TrfR-¢t was interfering with the function of the endogenous TrfR by possibly dimerizing with the endogenous TrfR. The transiently transfected cells looked normal and were viable for several days. The cells were cotransfected with a cytoplasmic green-‡uorescent protein (GFP) to facilitate the selection of expressing cells. The experiments were preformed 12-36 hours after transfection.

Hemagglutinin - a transmembrane raft-protein   The in‡uenza virus hemagglutinin (HA) glycoprotein is a well studied viral transmembrane protein. It performs two essential functions for viral infectivity: ...rst, it recognizes and binds to the host cell receptors. Second, after uptake into the endosome, it mediates the fusion of the virus and the vesicle membrane to allow penetration of the cytoplasm. HA is inserted in the membrane as trimer of identical monomers. The three-dimensional structure of the ectodomain is known to protrude 13.5nm outward with the antibody recognition sites in the outer third of the molecule [Wilson et al., 1981; Wiley et al., 1981; Watson et al., 1988]. Schei¤ele et al. [1996] have shown that HA is palmitoylated in its cytoplasmic domain and associates with the DIGs.

When expressed in BHK cells, HA was inserted correctly into the plasma membrane and was associated with DIGs [Schei¤ele et al., 1996]. About 12-36 hours before the di¤usion measurements, the cells were transiently transfected using lipofectamin (for details see the appendix on page 116).

Placental alkaline phosphatase - a GPI-anchored raft-protein   Placental alkaline phosphatase (PLAP) is a GPI-anchored membrane protein. It is sorted apically in MDCK cells, and is detergent insoluble. It associates to a high degree with raft-microdomains: about 90% of the PLAP molecules in the plasma membrane is found in the detergent insoluble fraction [Brown and Rose, 1992]. When expressed

in BHK cells, PLAP is detergent insoluble and PLAP-DIGs form percolation clusters that exclude non-raft proteins like the TrfR when cross-linked by antibodies [Harder et al., 1998].

PLAP was easily expressed at high levels in BHK cells. Again, the cells were cotransfected with a cytoplasmic GFP. A stably PLAP expressing BHK cell line was produced (Harder). No di¤erence between the measurements in the transient transfected cells and this cell line could be observed.

Cholesterol depletion by cyclodextrin extraction   For cholesterol depletion 30% con‡uent BHK cells grown on coverslips were washed in ...ltered medium and then incubated with 10mM methyl-ß-cyclodextrin for 30min at 37±C. Following a wash, the coverslips were transferred to the microscope for the measurement. This concentration of methyl-ß-cyclodextrin was reported to extract more than 90% of the cholesterol from the membrane of in‡uenza virus particles [Schei¤ele et al., 1997].

13.0.2   Experimental procedure

Fibroblasts expressing the protein of interest (human-TrfR-₵t, HA or PLAP) were plated on a coverslip at a density that yielded small groups of 2-10 spread cells for the experiments (see appendix for sample preparation procedures). The sample chamber was ...lled with ...ltered culture medium supplemented with 5 mg/ml ...sh skin gelatin (FSG). FSG was used to reduce the non-speci...c adsorption. A 0.2¹m diameter polystyrene sphere coated with an antibody against the protein of interest was trapped in the solution with a laser intensity of about 30 mW. This intensity resulted in a lateral spring constant for the sphere of k ¼ 1¹N=m and position ‡uctuations of §65nm RMS-displacement.

Figure 13-1 shows the principle of the measurement: A ‡at area of the cell was selected and the trapped bead was positioned 1:5¡ 3 ¹m above the plasma membrane (precision was limited by the low contrast of the membrane in the DIC microscope) (part (A) of ...g. 13-1). At this distance, about ten times the sphere's radius, the sphere's motion was not in‡uenced by the surface. A reference measurement was taken which was used to countercheck whether the radius of the sphere was within the accepted tolerance of 3.8% given by the supplier and to calibrate the detector sensitivity for this particular bead (see methods section 6.3). The sphere's three-dimensional position was generally recorded every 25¹s using the forward scattered light (x-, y- and z-signals form the QPD). Due to memory limitations on the data-acquisition board, the recording interval had to be increased to 50¹s to perform long-time observations up to 100s. A 50¹s time interval is still su₵ciently shorter than the autocorrelation time of motion of the sphere in the trapping potential. These fast position signals of the three-dimensional motion of the sphere were used for the thermal noise analysis. In addition, the two-photon ‡uorescence intensity as time-averaged measure for the axial displacement of the sphere, and the distance of the focus from the surface were monitored with 1ms temporal resolution.
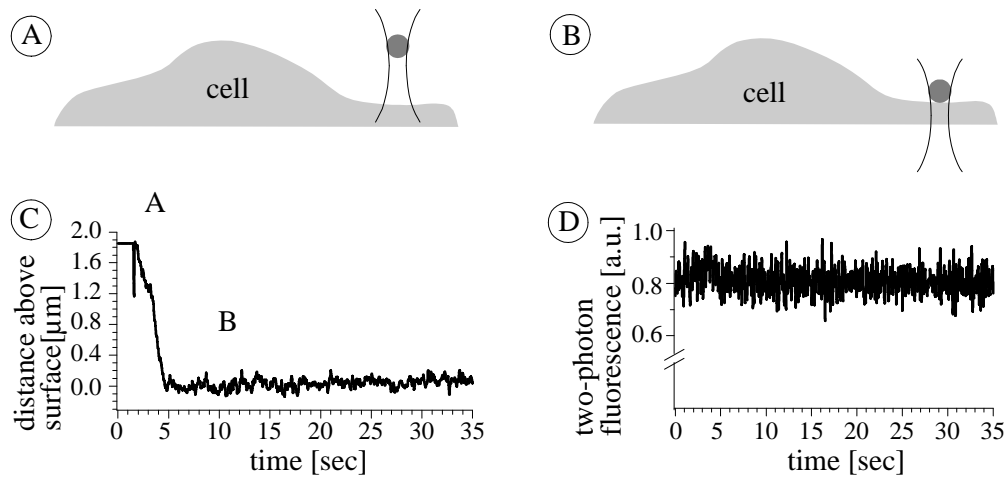
Figure 13-1: Measurement principle: trapping and reference measurement (A), approach of surface and contact (B). (C) displays the distance of the laser focus approaching the cell surface against the time of the measurement: at t=4s the feedback was engaged by the decrease in the two-photon ‡uorescence intensity and stopped the approach. (D) shows the two-photon intensity as position sensor signal against time of the measurement: during the approach the intensity ...rst increased and then, just before t=4s began to decrease (indicating the surface contact); thereafter it was kept constant by the feedback regulating the contact force.

A computer controlling the piezo of the objective lens moved the focus downward onto the cell (part (B) of ...g. 13-1). During the approach the two-photon ‡uorescence intensity increased (...rst 3s in (D) of ...g. 13-1). This increase is due to spherical aberrations [Florin et al., 1996]. Upon contact with the membrane, the bead was displaced from the focus axially and the two-photon ‡uorescence intensity decreased slightly (t=3 in part (D) of ...g. 13-1). A feedback program driving the focus positioning piezo kept the two-photon ‡uorescence intensity decrease minimal. The measured decrease of 10% corresponds to an average axial displacement of 200nm (see sect.5.2.1). Since the axial spring constant was $k_z = 0{:}15^1$ N/m (calibrated from the thermal noise according to sect.2.0.3), the force acting on the membrane was about 0:03pN.

The three-dimensional position distribution of the bead was analyzed to visualize the cellular surface in the location of the measurement. For further analysis and to calculate the di¤usion coe¢cients, only experiments in which the surface was ‡at and all three dimension were uncoupled were selected. The position ‡uctuations along each detector axis were evaluated independently. The time-series was calibrated using the reference measurement and cut into intervals of 1sec (or 40000 data points) duration, overlapping by 0.5sec. A constant o¤set was subtracted. For each interval the potential k was calculated from the Boltzmann statistic and the autocorrelation function computed. Fitting an exponential decay to the autocorrelation function

95

from 0:15ms to 25ms yielded the position autocorrelation time ι. The viscous drag $° = k\iota$ was computed and plotted as time series.

13.1 Potentials and di¤usion near the membrane

Reduced di¤usion near the surface

Figure 13-2 displays the lateral viscous drag of a sphere and the axial spring constant of the sphere-laser cantilever approaching the cell membrane versus time (same measurement as in ...g. 13-1). The measured lateral viscous drag $°$ in the x-direction (crosses in ...g. 13-2) and the y-direction (rhombi) in the bulk solution was $(1:62 \, \S \, 0:08) \, ¢ \, 10^{i\,9} \, Pasm$ and $(1:63 \, \S \, 0:12) \, ¢ \, 10^{i\,9} \, Pasm$, respectively. This agrees well with the Stokes drag of $1:628 \, ¢ \, 10^{i\,9} \, Pasm$ expected for the spheres used (r = 108nm) in a liquid of viscosity $´ = 0:8mPas$. The viscosity of water is $´ = 0:8mPas$ at $30^{±}C$ but decreases for higher temperature. The temperature of the objective lens at the bottom of the sample chamber was maintained at $35^{±}C$, so the temperature of the sample was expected to be slightly below this and the viscosity of the bu¤er reduced. Still, the measured viscosity of $´ = 0:8mPas$ is reasonable because the measurements were performed in a bu¤er containing 5mg/ml FSG which would increase the viscosity.

Due to the spatial con...nement, the viscous drag on a sphere is increased near a surface (see sections 2.1.1 and 8). In most experiments the viscous drag increased 1.8 to 2.2-fold for the $0.2^{1}m$-sphere near the cell surface (see ...g. 13-2(a)) which corresponds to a decrease in the di¤usion coe¢cient down to $45 \, \mathrm{¡} \, 60\%$. The di¤usion coe¢cients of $0.2^{1}m$ and $1^{1}m$-spheres near a coverslip surface decreased down to $40 \, \mathrm{¡} \, 50\%$ (the data for a $1^{1}m$-sphere are discussed in sect.8). In general the measurements agree with the theoretical description [Happel and Brenner, 1965; see section 2.1.1] which predicts a decrease to 40% for a sphere in contact with a smooth, rigid surface.
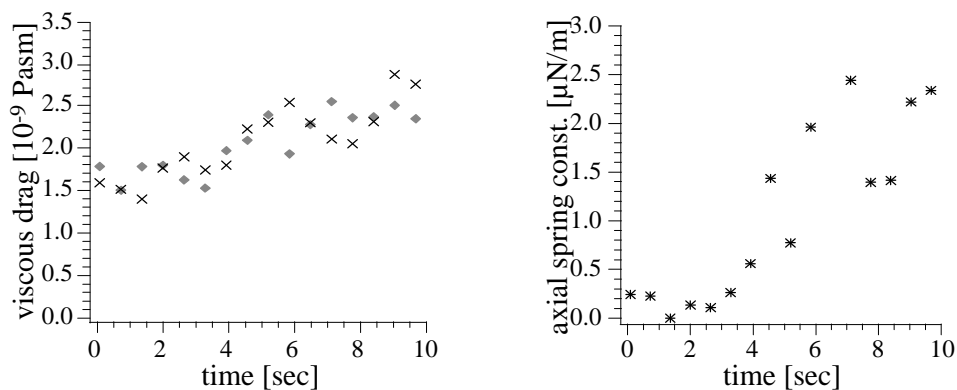

Figure 13-2: Lateral viscous drag (a) and axial spring constant (b) of a $0.2^{1}m$-sphere approaching the cell surface versus measurement time, surface contact at 5.4sec.
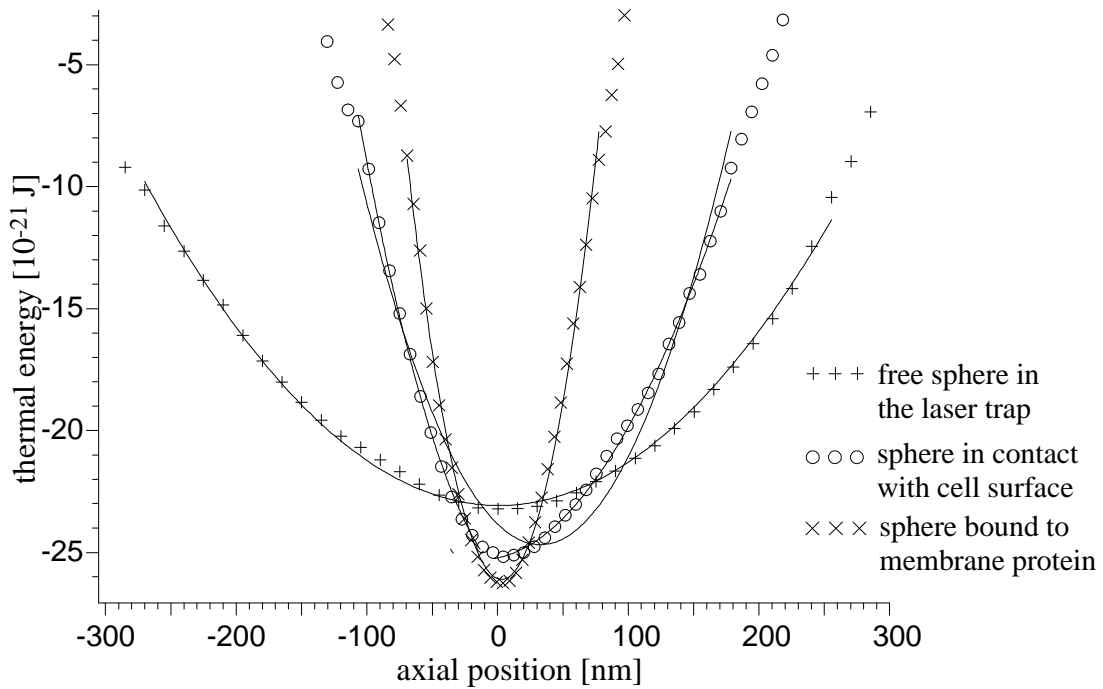
thermal energy [10^{-21} J]

-5

-10

-15

-20

-25

-300   -200   -100   0   100   200   300

axial position [nm]

+ + + free sphere in
the laser trap

o o o sphere in contact
with cell surface

× × × sphere bound to
membrane protein

Figure 13-3: Axial potentials for a free sphere in the trap in the bulk solution (+++, parabolic ...t: $k_z = 0{:}36$ ¹N=m), in repulsive contact with the cell surface (ooo, in-harmonic, parabolic ...t (dashed): $k_{z(average)} = 1{:}6$ ¹N=m) and bound to a laterally di¤using PLAP molecule (xxx, $k_z = 6{:}6$ ¹N=m). The cell is at the left (negative axial position). The potential trapping an unbound sphere in repulsive contact with the surface (ooo) is inharmonic and better approximated by two potentials: $k_{z(membrane)} = 2{:}3$ ¹N=m (left parable) and $k_{z(trap)} = 0{:}85$ ¹N=m (right parable).

The sometimes smaller decrease of the di¤usion coe₵cient near a cell surface could be due to a larger separation between the sphere and the surface at the same repulsive force: since the decrease of the two-photon ‡uorescence intensity was taken as mark for the contact to the surface, an additional repulsive force between membrane and sphere would displace the sphere earlier from the focus resulting in a ‡uorescence decrease at non-zero distance to the surface. According to the formula by Brenner, a decrease to 50% would correspond to a distance of 15nm between the surface and a sphere (r = 108nm).

Membrane ‡uctuations and elasticity

The axial spring constant, plotted against time in ...gure 13-2(b), increased upon contact with the cell membrane: the free axial potential was $k_z = (0{:}2 \S 0{:}1)$ ¹N/m, which increased to $k_z = (2 \S 0{:}8)$ ¹N/m upon contact with the membrane.

Axial cuts through the potential are shown in ...gure 13-3 at three time-points for a sphere binding to a PLAP molecule in the cell membrane (see ...g.13-4 lower

panel for a 3D-representation of the potential at the three time points). In ...gure 13-3 each curve represents a time-window of 1.25sec or 50000 points. The free potential with $k_z = 0:3\,^1$N/m was harmonic up to $\S250$nm displacements. Upon contact with the cell membrane, the potential was deformed by the repulsion from the membrane. The left-side, nearer to the membrane was better approximated by an exponentially repulsive potential (solid line) than by a harmonic one (dashed line). The harmonic part had a spring constant of $k_z = 1:2\,^1$N/m. After binding to a PLAP molecule di¤using freely within in the membrane the axial sti¤ness increased to $k_z = 5:5\,^1$N/m which is now a measurement for the sti¤ness of the lipid membrane bilayer orthogonal to its plane. In general, the spring constants of the membrane bilayer of BHK cells measured this way were $k_z = (7 \S 3)\,^1$N/m. When the beads attached to cytoskeleton bound proteins the spring constant rose to $k_z = (20 \S 15)\,^1$N/m.

(In relation to chapter 9.1: note that this small sti¤ness of the membrane in comparison to SFM cantilevers ($\gg 10$mN=m) explains the failure to resolve any details on the cell membrane using SFM. The membrane cytoskeleton underneath the membrane bilayer was imaged by SFM (p. 67), but not the membrane bilayer.)

13.2 Binding strength of the spheres to the membrane proteins

GPI-anchored PLAP

The spheres used were coated with an anti-PLAP polyclonal antibody by adsorption (see app. A.1). On untreated cells in the presence of 5mg/ml FSG in the bu¤er, 30% of these spheres would bind after being held near the cell membrane for 20-40s ($n_{tot}=30$).

The binding could be blocked by adding free human PLAP (P3895, Sigma). Adding 50nl of PLAP (1mg=ml; 15units=mg) to $10\,^1$l of a 1% spheres solution 15min prior to the experiment, did block the binding completely. Adding only 15nl of the PLAP solution to $10\,^1$l spheres, did not change the amount of spheres bound to the cell. But while 80% of the unblocked spheres became immobilized on the cell surface within the measurement interval, only 40% of the partially blocked sphere became immobilized after di¤using for more than a minute. These spheres were used for the measurements of the viscous drag (sect.13.3).

After depleting the cholesterol from the cells, only 30% ($n_{tot}=40$) of the anti-PLAP antibody coated spheres bound to the cell surface of the stably expressing PLAP cell-line. In transiently transfected cells the cholesterol depletion resulted in an even further reduced binding probability. All spheres bound were easily removed from the cell at the end of the measurement or even dissociated (33% of the bound spheres) after being bound for about 10s. The axial force constant of the PFM was about $0:5\,^1$N/m, and the thermal position ‡uctuations about $\S250$nm. Therefore, the maximal force pulling at the protein due to the thermal ‡uctuations during the

measurement was less than $0:15$pN. Since the trapping range is about $0:6\,\mu$m the maximal force encountered during the removal of the laser trap at the end of the measurement was about $0:3$pN. This indicates a very weak association of the GPI-anchor to the membrane after cholesterol depletion. It was observed before that extracting the cholesterol reduced the concentration of PLAP molecules on the cell surface [Keller, pers. com.].

Transmembrane proteins TrfR and HA

Spheres coated by adsorption with an anti-human TrfR polyclonal antibody (see app. A.1) were used. 53% of the spheres ($n_{tot}=32$) did bind to the cell surface. Of these one third was immobilized, while two thirds diffused over the cell surface. After removing the laser trap the spheres would diffuse over the cell surface for several minutes. These beads could also not be dissociated from the membrane by applying about 5pN pulling force.

Depleting the cholesterol from the cells by cyclodextrin extraction did not alter the percentage of spheres binding. Still the pulling force was insufficient to separated the bound spheres from the cells.

The spheres coated with anti-TrfR antibodies did not bind to untreated BHK cells or the PLAP expressing BHK cell lines. Only doubling the laser intensity and the contact force did cause 1-2% of the spheres to attach unspecifically.

The results for spheres bound to the raft-associated transmembrane protein HA were the same as for the TrfR: the spheres could neither in untreated cells nor in cholesterol depleted cells be separated from the membrane.

13.3   Viscous drag of membrane proteins

Placental alkaline phosphatase

The viscous drag of the GPI-anchored protein PLAP was measured to $\gamma_p = (3:3 \pm 0:7)\cdot 10^{-9}\,$Pas m (figures 13-4(a) and 13-6(a)). The error given is the standard deviation from the mean, the maximal deviation was $\gamma_p = 1:1 \cdot 10^{-9}\,$Pas m. No variation between stably and transiently transfected cells was observed. A freely diffusing particle captured again after $10-15$min by the PFM, exhibited a small increase of the viscous drag (see fig. 13-4(b)). While the lateral potential holding the molecule-sphere complex was influenced only slightly during the initial binding to the PLAP protein (fig. 13-4(c)), it increased suddenly during the second observation interval (fig. 13-4(d), arrow) indicating an elastic binding. In agreement with this, it was possible of move the sphere about $0.5\,\mu$m laterally before it escaped the trapping potential.

At the end of the measurement intervals, 60% of the bound spheres diffused over the entire cell. Most of the remaining spheres were tethered, i.e. it was only possible to move them laterally between 300nm and 600nm before they escaped from the
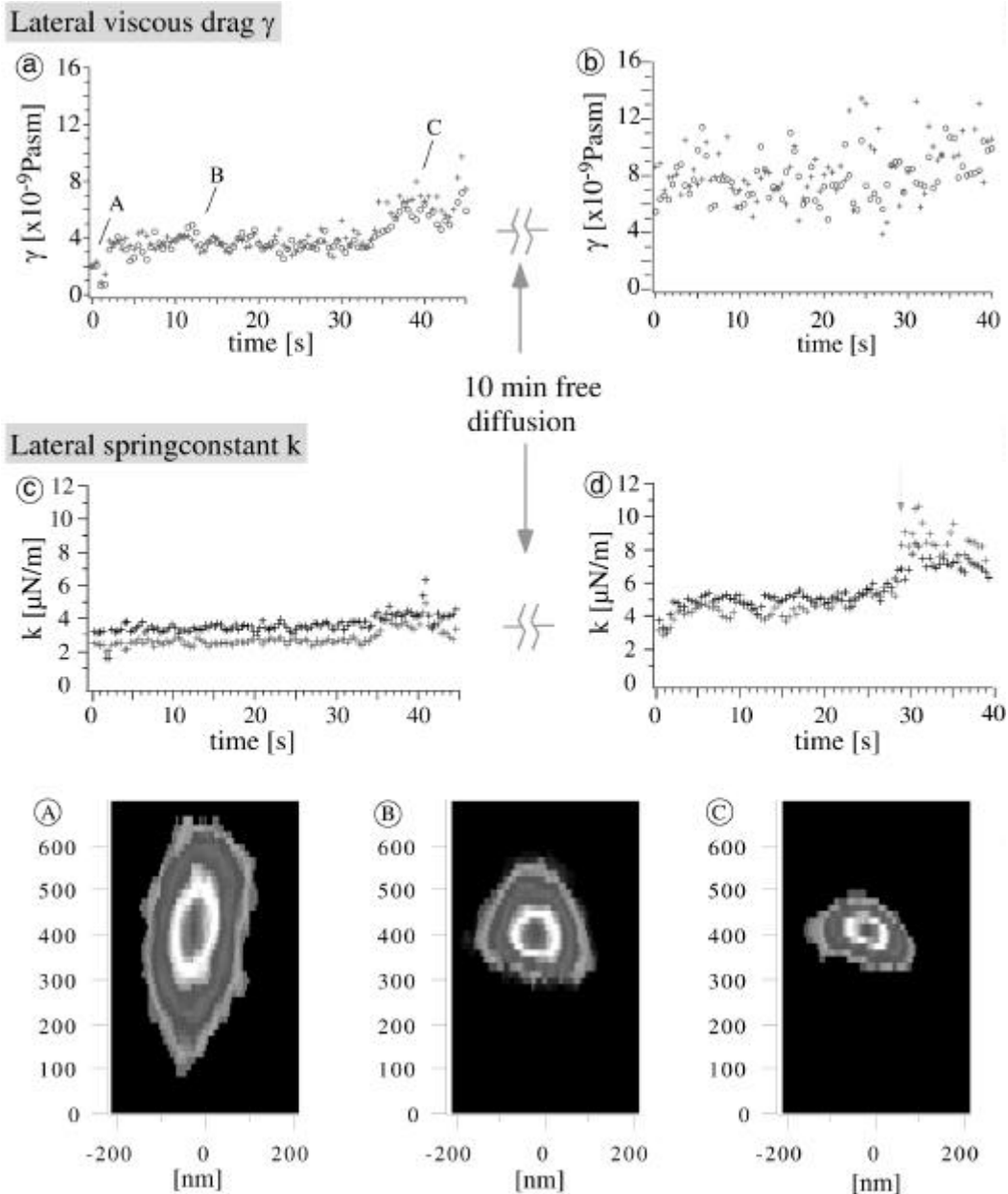
Figure 13-4: The binding of the sphere to a PLAP molecule, resulted in steep increase of the viscous drag (a). The lateral spring constant was hardly changed (c). After releasing the sphere from the trap, it di¤used freely over the cell surface (in this case for 10min in an area of about 5 £ 5¹m). After retrapping the same viscous drag was measured (b). Eventually the lateral spring constant increased and the sphere became immobilized (d). The lower images show the axial cuts through the potential trapping the sphere at the time-points (A)-(C), indicated in plot of the di¤usion coe¢cient: (A) laser trap potential, (B) laser trap plus repulsive surface at bottom and (C) bound to a di¤using molecule.

axial autocorrelation time

t^z [ms]

12
10
8
6
4
2
0

0 5 10 15 20 25 30 35 40 45

time [s]

axial spring constant

k^z [µN/m]

6.0
5.0
4.0
3.0
2.0
1.0
0.0

0 5 10 15 20 25 30 35 40 45

time [s]
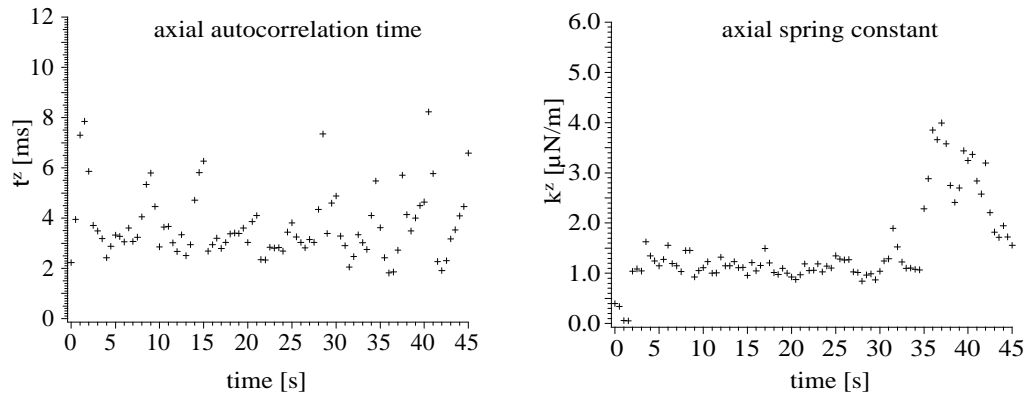
Figure 13-5: The axial signals to the previous ...gure. Upon binding to PLAP the axial autocorrelation time τ only slightly changed, while the axial spring constant k increased three fold, resulting in an increased viscous drag $\gamma = k\tau$.

laser trap which was used at k ¼ 1¹N=m. Only about 10% of the spheres were completely immobilized.

After extraction of the cholesterol by incubation with methyl-ß-cyclodextrin the damping was reduced (...g. 13-6(d)). One third of the 30% binding spheres showed still a viscous drag of more $\gamma_p = 2{:}5 \cdot 10^{-9}$ P as m, while two thirds of the measurements yielded values below $\gamma_p = 2 \cdot 10^{-9}$ P as m. Assuming that this spread was due to incomplete dissociation of the lipid microdomains the ...rst lowest measurements ($\gamma_p = (0{:}6 \S 0{:}4) \cdot 10^{-9}$ P as m) were taken to represent the smallest entity, possibly a single GPI-anchor.

Transferrin receptor

The probes bound to the TrfR and di¤using showed a wide range of viscous damping (...g. 13-6(c)). Some (n=3) measurements were not included in ...g. 13-6(c) because they yielded an extraordinary large increase of the viscous drag ($\gamma_p = 17 ¡ 26 \cdot 10^{-9}$ P as m). In the these cases (discussed in sect.13.3.2, ...g. 13-7) the lateral spring constant was not changed (...g. 13-7(b)), just the autocorrelation time was increased. So the complex that the sphere was binding was free to di¤use within the boundaries given by the trap potential. Binding to this complex increased that axial viscous drag γ_z about ...vefold (...g. 13-7(d)) and doubles the axial spring constant k_z (...g. 13-7(e)).

The group of measurements with lowest viscous drag was around $\gamma_p = (1{:}6 \S 0{:}5) \cdot 10^{-9}$ P as m, which was assumed to be the measurement of an individual TrfR molecule.

Experiments performed with spheres with a radius of 55nm yielded essentially the same increase of viscosity due to the binding. Except that handling of those spheres is increasingly di¢cult, so that only some tests were performed.

After extracting the cholesterol using methyl-ß-cyclodextrin the values obtained of the viscous drag of the TrfR-Φt did not change (...g. 13-6(f)). The large viscous damping observed sometimes in the untreated cells, was also seen in the cholesterol depleted cells. The lowest values were again clustered around $\eta_p = (1\text{:}6 \S 0\text{:}4) \Phi 10^{i\,9}$ Pasm.

13.3.1 Evidence of cholesterol stabilized microdomains

The viscous drag of the GPI-anchored protein PLAP ($\eta_p \frac{1}{4} 3\text{:}3 \Phi 10^{i\,9}$ Pasm) was greatly reduced by depleting the cholesterol from the membrane with cyclodextrin ($\eta_p \frac{1}{4} 0\text{:}6 \Phi 10^{i\,9}$ Pasm). In contrast, the viscous drag of the TrfR protein ($\eta_p = 1\text{:}6 \Phi 10^{i\,9}$ Pasm) was not in‡uenced by cholesterol depletion.
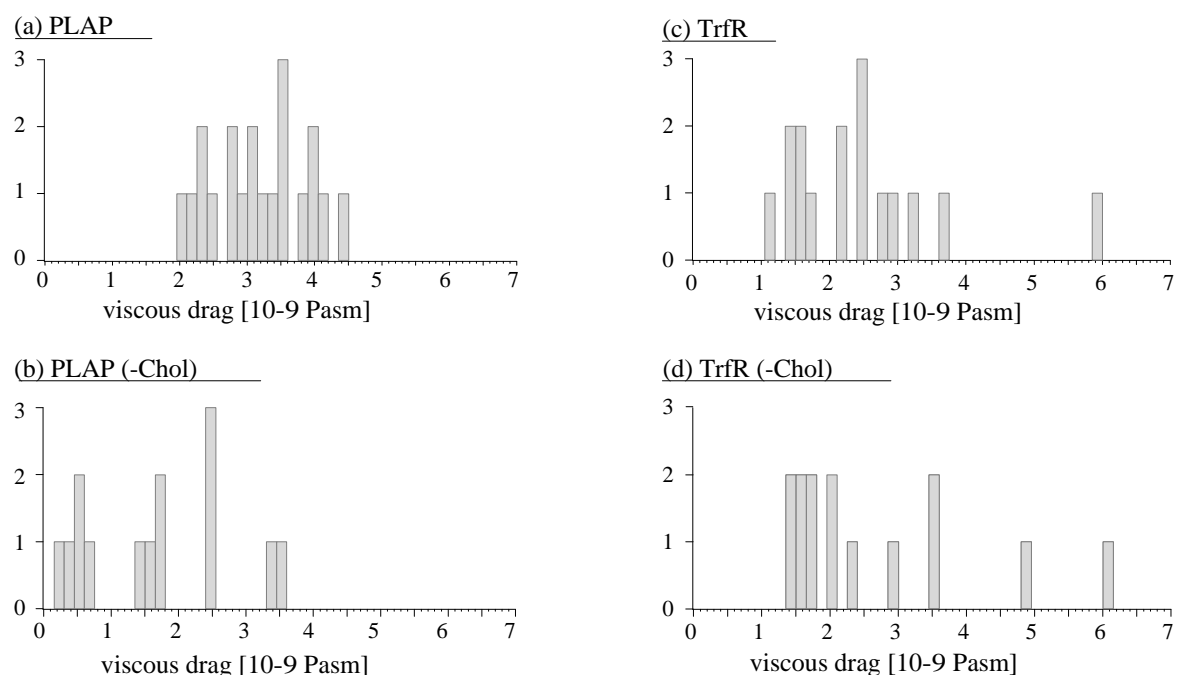
Figure 13-6: Overview of the viscous damping measured for the membrane proteins PLAP, HA and TrfR and their change after depleting the cholesterol from the cells (-Chol): (a) PLAP in untreated cells caused a characteristic viscous damping ($3\text{:}3 \Phi 10^{i\,9}$ Pasm), (d) cholesterol depletion resulted in a shift to much lower damping, but the measurements were spread over a range up to viscous drags measured in untreated cells; (b) the viscous drag of HA peaked in untreated cells around $2 \Phi 10^{i\,9}$ Pasm. (e) Cholesterol depletion resulted also in a values around $1\text{:}3 \Phi 10^{i\,9}$ Pasm and around $3\text{:}2 \Phi 10^{i\,9}$ Pasm similar spread of values. (c) The lowest drags measured for the TrfR clustered around $1\text{:}6 \Phi 10^{i\,9}$ Pasm, but a range of higher values up to 20times this value (not shown) were also measured; (f) this did not change after cholesterol depletion.

102

This increased viscous damping of the PLAP protein in comparison to the TrfR has to be attributed to the size of the di¤using object. Especially the change for PLAP caused by the cholesterol depletion indicates that PLAP is bound to a diffusing object which is stabilized by cholesterol. It also excludes that the di¤erences between PLAP and TrfR would be caused by di¤erences in the size or ‡exibility of the ectodomain of the proteins. Since the potential con...ning the particles motions was measured simultaneously, in‡uences of additional lateral trapping potentials could be caused by immobile obstacles in the membrane and the associated membrane skeleton can be excluded.

Therefore the measurements indicate that PLAP is part of a stable complex that di¤uses as one entity for at least several minutes.

Some preliminary measurements of the viscous drags on HA in cholesterol depleted cells ($\eta_p \approx 1.3 \cdot 10^{-9}\,Pa\,s\,m$ and $\eta_p \approx 3.2 \cdot 10^{-9}\,Pa\,s\,m$) agree with this interpretation of the PLAP and TrfR results, because after dissolving the microdomains HA as a transmembrane protein should have a viscous drag similar to the TrfR ($\eta_p = 1.6 \cdot 10^{-9}\,Pa\,s\,m$), undissolved microdomains should be similar to PLAP ($\eta_p \approx 3.3 \cdot 10^{-9}\,Pa\,s\,m$).

13.3.2 Large autocorrelation times measured for the TrfR

The extremely large viscous drags sometimes observed for the TrfR could have three possible causes:

1) First, the spheres could be multivalent and bind several TrfR molecules simultaneously causing a larger increase in the viscous drag. But the coating density of the spheres was optimized for a low binding probability. Usually 20-40s passed before any binding occurred. To then have a multiply binding within the 0.5s temporal resolution of the measurement seems unlikely.

2) Second, the expressed TrfR-¢t could have dimerized with wild-type TrfR which clusters due to its interaction with Clathrin forming ‡at complexes of several hundred nanometers diameter, before these invaginate to form clathrin coated pits [Miller et al., 1991]. The human TrfR-¢t construct used for the measurements does not interact with clathrin directly because the required amino acid sequence was deleted, however it could dimerize with endogenous TrfR. The sharp increase in axial viscosity, normal to the membrane surface, suggests the binding to a more rigid structure. But the axial spring constant is only raised two-fold. Because no change in the lateral spring constant is observed, it has to be assumed that the sphere is not bound to the cytoskeleton and has not entered a membrane invagination, such as a coated pit or caveolae, which would reduce the lateral motion.

3) Finally, the TrfR-¢t molecule could be damped randomly by sporadic interactions with the membrane skeleton. It was shown that E-Cadherin with 21 amino acids in the cytoplasmic domain [Kusumi et al., 1994] and MHC I
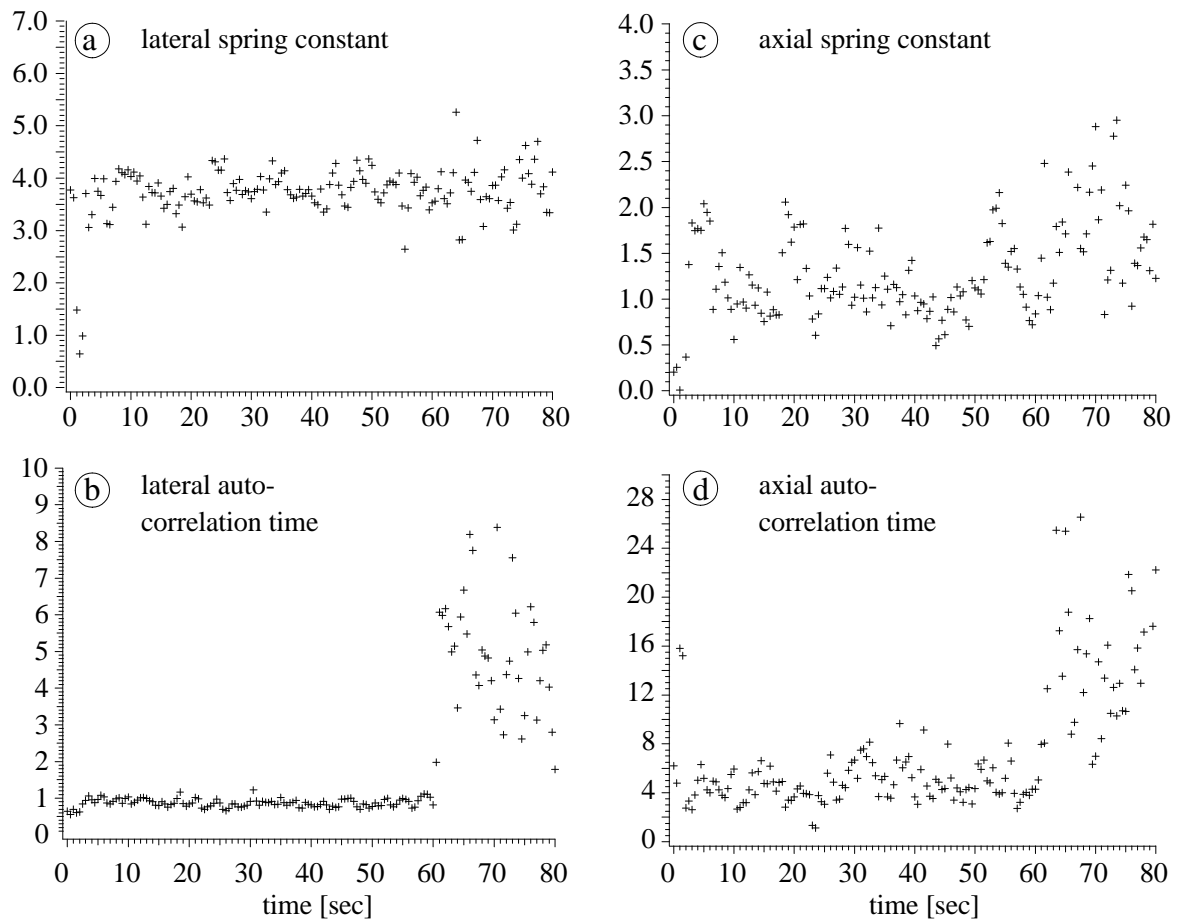
Figure 13-7: In some case the beads bound to the TrfR-¢t construct showed a large damping ($^\circ$ = 17 ¢ 10^{i} ^{9}P asm). This is purely a result of the viscous drag because only ¿ was increased (a) and not the lateral spring constant (b). While the axial spring constant only increased sightly (c), the axial-autocorrelation time (d) rose ...vefold.

mutants with only 7 amino acids [Edidin et al., 1991] still interact with the membrane skeleton. So the TrfR-¢t construct with 26 amino acids in the cytoplasmic tail could still interact with the membrane skeleton. But, the same publications also showed barrier free paths for the interacting molecules of 1-1.5¹m, which is much larger than the area sampled in our local measurement.

Currently, it is not possible to draw a ...nal conclusion. A construct of a transmembrane protein with an even shorter cytoplasmic tail or even modi...ed transmembrane domain is needed to exclude interactions on the cytoplasmic membrane side.
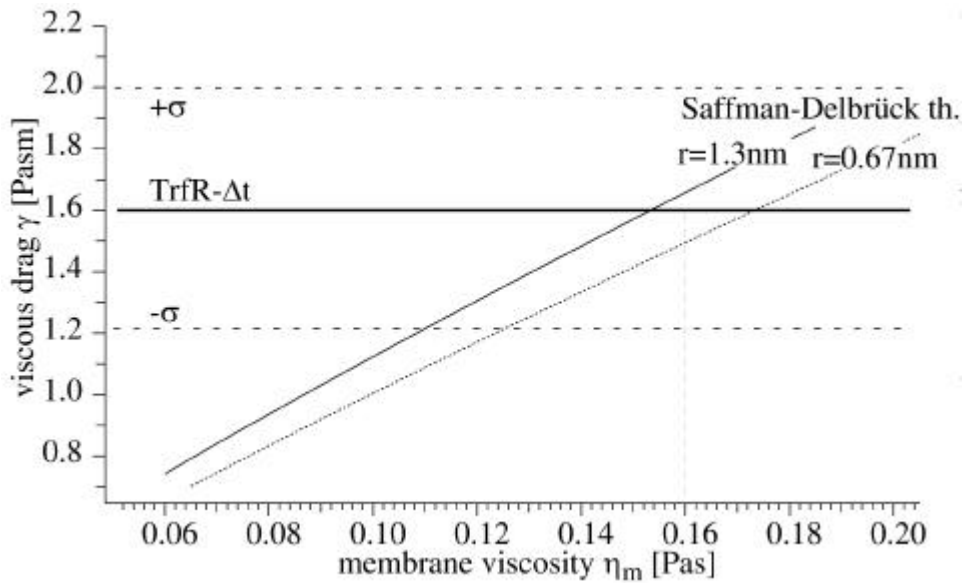
Figure 13-8: Dependance of the viscous damping ° of a transmembrane protein on the membrane viscosity η_m according to the Saꞌman-Delbrück theory. The theoretical dependence is shown for a transmembrane domains with r=0.67nm and r=1.3nm, assuming a membrane thickness of 5nm. The measured viscous drag for the TrfR-₵t is plotted with maximal errors.

13.3.3 Interpretation applying the Saꞌman-Delbrück model

Determination of the membrane viscosity

Since the measurements were done within an area of 130nm diameter in about 1s, the surrounding medium was assumed to be fairly uniform. The fact that no change of the lateral trapping potential upon binding to the membrane proteins was observed (e.g. ...g.13-4 lower images), suggests that the studied membrane proteins and microdomains were indeed free to diꞌuse within the sampled circle of 65nm radius.

Therefore, the theory of Saꞌman and Delbrück for the diꞌusion of proteins in a lipid bilayer (see theory section 2.2.1 on p. 22) was used to estimate the viscosity of the lipid bilayer from the TrfR measurements. The viscous drag for a cylindrical protein of radius r in a bilayer of viscosity η_m and thickness h would be (see eq.(2.19b)):

$$°_p = 4\pi \eta_m h \left[\ln \frac{\eta_m h}{\eta_w r} \mathbf{i} \ 0{:}5772 \right]^{\mathbf{i} \ 1} : \qquad (13.1)$$

 The viscous drag depends on the radius r of the membrane protein, the membrane viscosity η_m and thickness h. A few mobile obstacles would mainly increase the eꞌective viscosity [Cherry and Godfrey, 1981; sect.13.4]. An arti...cial lipid bilayer
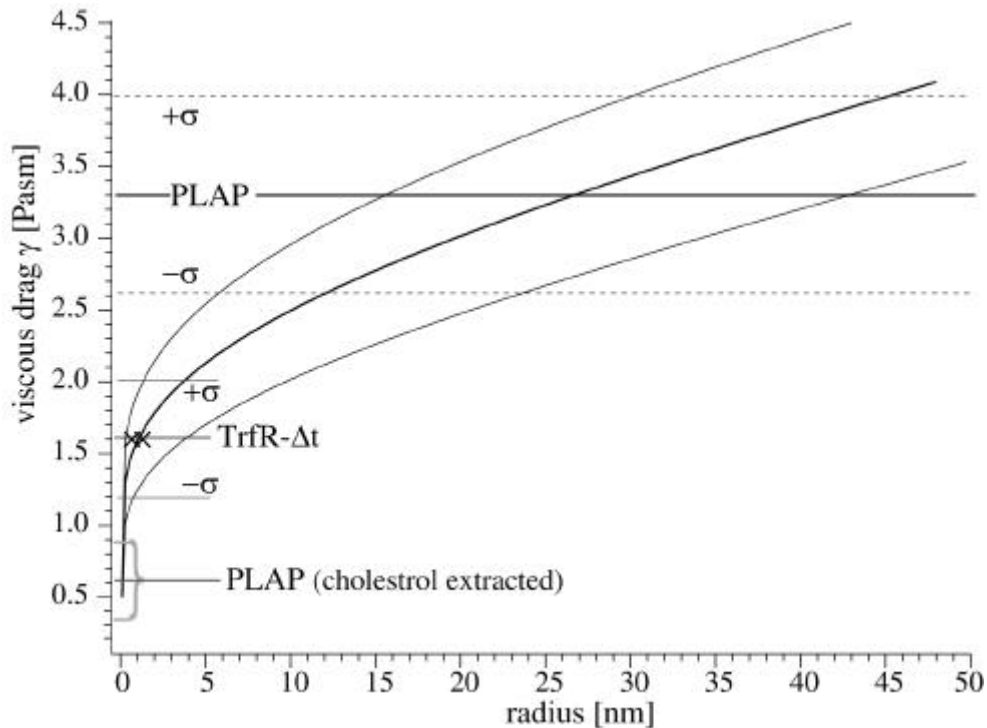
Figure 13-9: Dependance of the viscous damping of a transmembrane protein on the radius of the transmembrane domain according to the Saxman-Delbrück theory for membrane viscosities $\eta_m = 0.16 Pas$ (—) and the lower and upper bounds $0.12 Pas$ and $0.2 Pas$ (- - -). The viscous damping measured for PLAP, TrfR-¢t and PLAP in cholesterol depleted cells are marked with maximal errors.

made of dimyristoylphosphatidylcholine (DMPC) is about $4.5 nm$ thick [Peters and Cherry 1982]. Cellular bilayers are composed of a variety of lipids and contain a large proportion of proteins that could in‡uence the e¤ective thickness and viscosity (see discussion on p. 107 for their in‡uence on the viscosity). A thickness of 5nm is generally assumed for the plasma membrane [Alberts et al., 1984]. The TrfR protein has a single transmembrane domain, that was assumed to be an ®-helix as all transmembrane domains investigated so far have ®-helical structure [Alberts et al., 1984]. The diameter of the carbon backbone of an ®-helix is about 0.5nm [Stryer, 1988], but it is not clear how much space a transmembrane domain with the sidechains occupies in the lipid bilayer. Recently, Eskandari et al. [1998] have measured the transmembrane area of several membrane proteins and estimated that a single transmembrane helix occupies $1.4 nm^2$, which corresponds to a radius of 0.67nm. Because the TrfR is a dimer, we have indicated the viscous drag for proteins with r = 0.67nm and r = 1.3nm as a function of membrane viscosity in …gure13-8.

A viscosity of $\eta_m = 0.16 Pas$ agrees best with the data for the TrfR. Due to the

large error in the measurement and the low dependence of the viscosity on the size of the di¤using molecule, a range of viscosities ($0.12 ¡ 0.2 Pas$) would still agree with our data. This lies at the upper end of the values assumed in the literature ($0.08 ¡ 0.15 Pas$) [Vaz et al., 1984]. Peter and Cherry [1982] have determined the viscosity of DMPC vesicle to be $´_m = 0.11 Pas$ which can be assumed to be a lower bound for the viscosity of cellular membranes.

Estimation of the size of the microdomains

Even though the PLAP protein is only inserted in the outer lea‡et of the bilayer by the GPI-anchor, the model suggests that both lea‡ets are part of the raft microdomain [Simons and Ikonen, 1997]. This is assumed because of the large chain length of the sphingolipids that could reach into the second lea‡et and because of the signalling that is transmitted through GPI-anchored proteins into the cell. The fact that the viscous drag for HA and PLAP in untreated cells was about the same enforces this assumption.

Therefore, the theory of Sa¤man and Delbrück for the protein di¤usion in a lipid bilayer (eq. 13.1) was applied with the same membrane thickness $h = 5nm$ as for the TrfR measurement and the viscosity of the lipid bilayer ($´_m = (0.16 § 0.04) Pas$) obtained in these TrfR measurements (see above and ...g. 13-8). Using these parameters ...gure 13-9 displays the dependence of the viscous drag on the radius r of the di¤usion cylindrical object according to the Sa¤man-Delbrück theory (eq. 13.1). The measured value for viscous drag of the PLAP protein in untreated cells and after cholesterol depletion is shown. From this a radius of $r = (26 § 13)$ nm was estimated for the lipid microdomains in which PLAP was found. The large error is due to the logarithmic dependence of the viscous drag on the radius and the uncertainties associated with the membrane viscosity.

13.4   Discussion

Thermal noise analysis: e¤ect of linker between bead and protein

When reconstructing the motion of a molecule from the motion of a sphere linked to the molecule, the geometry is important. If the tether length is large and holds the sphere like on a stalk, the sphere could rotate around the linker without moving the molecule's base. This could lead to measurement error because ...rst, the sphere could move without the protein moving and secondly, the directions in space would be coupled. The following discussion should clarify that in the investigated case the sphere di¤used together with the membrane protein.

The scaled model of the experimental situation in ...gure 13-10 gives a perspective of the linker length. Assuming that the Y-shaped antibody adsorbs with one short arm and the Fc area (lower part of the Y) to the sphere, the length of the linker would be about 10nm to 15nm for the HA molecule for which the dimensions are known (see section 13.0.1). One has to assume that the geometries for the PLAP

molecule and TrfR are similar. A sphere of radius r=108nm linked to a ‡exible joint on a hard surface by a sti¤ linker of 15nm length would move on a section of a sphere around the anchor point. A projection of this motion on the plane of the surface, would appear as lateral displacements of §47.5nm. The plasma membrane and the sphere are covered with proteins, that occupy space and repel the opposing surface. Thus it can be assumed that the linker is under tension and the ‡exibility reduced. For a 10nm thick protein coat and a linker length of 15nm, the sphere could still move §34.7nm laterally without moving the protein in the membrane. In contrast, the area sampled by the sphere was larger than §65nm.

The membrane around the sphere was not ‡at either: it ‡uctuated thermally excited, but was on average depressed by the sphere. As visible in ...gure 13-3, the membrane ‡uctuated almost §100nm. Since the membrane's spring constant was ten-fold higher than the one of the laser trap (sect.13.1) and the sphere was displaced about 150nm in the laser trap (sect.13.0.2), the membrane was on average 10-15nm indented by the sphere (see ...g. 13-3). Only when binding to a protein connected to the cytoskeleton, the deformation was decreased to 2-5nm. Then the linker could cause the sphere to move independently.

An independent motion of sphere and molecule would result in two position autocorrelation times due to the large di¤erent viscous drag on both. The auto-correlation functions obtained of beads bound to freely di¤usion protein did not show a double-exponential decay. Only the ...rst time points up to 75-100¹s are indicate a faster decay, but it is not enough to be signi...cant. Once the sphere is bound to a cytoskeletal structure, meaning the lateral spring constant measured is increased, then the position autocorrelation of the sphere would be better ...t by a double-exponential decay.

Therefore, it is assumed that the sphere's motion represents the actual displacement of the membrane molecule for a freely di¤using molecule.
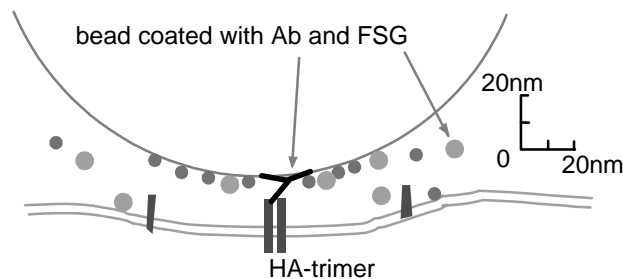

Figure 13-10: Scaled model of the bead bound to a HA molecule in the plasma membrane.

Comparison to diffusion coefficients measured by SPT and FRAP

The diffusion coefficients obtained by various investigators in the past years have varied greatly. The following table compares the current results to earlier measurements:

molecule	$[10^{-10}\ cm^2/s]$	publication	meth.	cells
TrfR-ΔT	D = 350	this study	TNA	BHK cells
TrfR (wt)	D = 12	- " -	SPT	hipp. neurons
- " -	D = 1	Kusumi JCB (98); (94)	- " -	L-cells;...broblasts
PLAP	D = 160	this study	TNA	BHK cells
- " -	D = 24	Jacobson JCB(91)	FRAP	COS-1 cells
Thy 1.1	D = 22	this study	SPT	hipp. neurons
- " -	D = 133	Jacobson Biochem (81)	- " -	lipid bilayer
- " -	D = 8	Sheets Biochem (97)	SPT	C3H cells

There is a large spread in the diffusion coefficients ($1 - 24 \cdot 10^{-10}\ cm^2/s$) obtained by SPT. These measurements are one to two orders of magnitude smaller than the theory of protein diffusion in a lipid bilayer would predict [Saffman and Delbrück, 1972] (sect.2.2.1). The SPT results depend on the length of the track analyzed and on the different diffusional mode assumed (see theory section). It is largely a measurement of the interaction of the protein of interest with the other membrane proteins, resulting in values too small for freely diffusing proteins. Several theoretical models have been developed to take the effects of mobile and immobile obstacles in the membrane in to account [Saxton, 1987 and 1989b]. The FRAP measurements also average over micrometer distances and in addition are an ensemble average comprising uncertainties about the diffusing molecules [Saxton and Jacobson, 1997; Feder et al., 1997]. It is hence not surprising that the diffusion constants measured by SPT were smaller than the local diffusion coefficients obtained by the thermal noise analysis in this study.

Previously reported membrane viscosities

The membrane viscosity η_m of cells is not known. All measurements performed so far were based on diffusion which is hampered for the case of proteins by the interaction of the probe with the membrane skeleton and other proteins. Also, it cannot be assumed that the viscosities deduced from the rotational motion of lipid probes are applicable on the scale of proteins.

Using the rotation of the lipid probe diphenylhexatriene in DMPC Kinosita and colleagues have determined a viscosity $\eta_m \approx 0.03\ Pas$ at $32^{\circ}C$ [1981]. Peters and Cherry [1982 and 1986] have investigated the influence of the protein density in the lipid bilayer onto the diffusion of bacteriorhodopsin (BR) in DMPC-vesicles. Using fluorescence recovery after photobleaching (FRAP) to determine the lateral diffusion coefficient and utilizing previous measurements of the rotational diffusion [Cherry and Godfrey, 1981] they have determined the radius of BR ($r = 4.3 \pm 0.5$) and the

viscosity of DMPC ($T_m = 23.5°C$) at $32°C$ depending on the lipid/protein ratio [mol/mol]:

lipid/protein ratio	210	140	90	30	∞ (extrapolated)
D $[10^{-12}m^2/s]$	3.4	2.3	1.3	0.15	-
γ $[10^{-9}Pa \cdot m \cdot s]$	1.2	1.8	3.2	27.9	-
η_m [Pas]	0.11	0.18	0.35	(4.3)	0.06-0.08

In agreement with these values, Poo and Cone [1974] have measured using FRAP the diffusion coefficient $D_L = 0.35\,10^{-12}$ m^2/s for the frog rhodopsin in the rod outer segment disk membrane, a membrane lacking cytoskeletal elements. The lipid/protein ratio in this membrane is close to 65 [Dratz et al., 1979]. Cherry has compared his measurements to values obtained by Liebman and Pugh [1979] for diffusion of the labelled lipid diO-C18 in the DMPC vesicles. The diffusion coefficients of BR and of diO-C18 decreased in the same linear manner for lipid-protein ration of 210 down to 90.

Laser influence

Even though the absorption of water and biological material is minimal in the range of the wavelength $\lambda = 1064nm$ used, some energy is absorbed and the strong field near the focus could interact with the surrounding molecules, resulting in two possible artifacts: localized heating and tension induced in the membrane.

The rise in temperature has been investigated by Liu et. al., 1995, on liposomes and Chinese hamster ovary (CHO) cells. They have exploited the temperature sensitivity of the environment sensitive lipid-probe Laurdan (6-dodecanoyl-2-dimethyl aminonaphthalene). The Stoke-shift of the fluorophore Laurdan changes depending on the surrounding lipid-phase. Using a IR-laser ($\lambda = 1064$) with a focus spot size of $\sim 0.8\mu m$ they have measured a temperature rise of $\sim 1.45 \pm 0.15°C/100mW$ in the phospholipid 15–OPC and $\sim 1.15 \pm 0.40°C/100mW$ in CHO-cells. As the measurements of the local diffusion were done at $20mW$ to $40mW$ the temperature rise can be ignored.

Bar-Ziv et al., 1998, have shown that laser tweezer with $\lambda = 514nm$ can induce local tension in artificial lipid bilayers. The interaction energy between laser and bilayer is

$$U = (\epsilon_L - \epsilon_W) \int \left\langle |E|^2 \right\rangle = \frac{(\epsilon_L - \epsilon_W)\,ID}{c_W\,w_0^2} \int_{St} dS \qquad (13.2)$$

with ϵ_L and ϵ_W being the dielectric constants of the lipid and water, respectively, c_W speed of light in water, I the intensity, D the thickness of the bilayer, w_0 the focal beam half-width and the integral extending over the interaction area. Because of the inverse dependence on w_0^2 the effect is expected to scale with λ^{-2}. They have reported that laser intensities of $10mW$ were the lower bound for any effects, so that hardly any effect is expected for the intensities of $20mW$ to $40mW$ at twice the wavelength, that were used in this work.

13.4.1 Conclusions

The technique developed for this thesis work could elucidate the membrane viscosity of living cells at the single protein level. The locally measured viscous drag imposed by the membrane bilayer on the transmembrane domain of the TrfR agrees with the diffusion of a protein with a single transmembrane domain in a lipid bilayer with a viscosity of 0.16 Pa s. These measurement were the first diffusional studies performed in cells to agree with the theory of diffusion in a bilayer that had been proven in artificial bilayers before. The large viscous drag measured for the GPI-anchored protein PLAP shows that this protein is part of a lipid microdomain of about 50nm diameter that diffuses as one entity in the plasma membrane. The decrease in the viscous drag after cholesterol depletion indicates that these microdomain are stabilized by cholesterol. In cholesterol depleted cells the GPI-anchor could be extracted from the cells with less than 0.3pN force while in untreated cells this was impossible. This underlined the role of cholesterol in stabilizing the lipid microdomain structures.

The spring constants of the membrane bilayer of BHK cells was measured to be $5 \cdot 10^{-1}$ N/m. This small stiffness of the membrane in comparison to SFM cantilevers ($\gg 10$ mN/m) explains the difficulties in imaging the cell surface using SFM. Due to the applied forces the membrane cytoskeleton underneath the membrane was imaged by SFM, but not the membrane bilayer.

13.5   Outlook and future applications

The proof of the existence of the rafts in living intact cells and the determination of their size within this thesis work is an essential contribution to the understanding of cell membrane structure and dynamics and demonstrates the power of the method developed. The knowledge obtained and the method will have a great impact when applied to further cell biological questions:

Microdomains have been implicated in cell signalling, but it is unclear how the signals are transferred to the inside of the cell. Some studies have shown that a signalling cascade is started and actin is polymerized when raft associated receptors are clustered. During the studies for this thesis it was observed that spheres held after binding to PLAP in one place would become elastically tethered. In this way, it would possible to measure the binding of signalling molecules and the following cytoskeletal reaction with high temporal resolution. Since the role of cellular signalling becomes more and more noted in immunology, developmental biology and cell biology, this opens a wide area of applications for the PFM.

Besides grouping membrane components necessary for signalling, membrane microdomains in‡uence the di¤usion of membrane components. In an array of cytoskeleton anchored proteins, microdomains would be immobile while smaller proteins and lipids could di¤use freely. Such a structure can form selective di¤usion barriers, such as the barrier proposed at the base of the axon, that was studied by SPT in this thesis. Applying the PFM this model can be tested and the distance between the immobile cytoskeleton anchored proteins be measured.

A further, still not well understood process at the cell membrane is the uptake of external structures through the cell membrane. By tracking the Brownian motion of a sphere imported by a cell, the time course of the role cytoskeleton and the forces involved can be studied.

Besides questions from cell biology the method can have a much broader range of applications:

The temporal resolution of the three-dimensional particle-tracking within a con-...ning potential can be increased several orders of magnitude with the appropriate photo diodes and electronics. Then it would be an ideal tool to study the microscopic dynamics of Brownian motion in more depth, and investigate possible e¤ects of surface properties of the di¤using object. Also the in‡uence of mobile or immobile obstacles in the case of two-dimensional di¤usion in a bilayer and for three-dimensional di¤usion of the sphere could be studied. In this way the method could have an impact on the development of microstructure devices for chemical analysis.

These are just a few possible applications of the method developed, three-dimensional particle tracking in the PFM, and the knowledge gained about the cell membrane.

Part VI

Appendix

Appendix A

Probes

A.1 Functionalizing polystyrene spheres

Polystyrene spheres, often referred to as latex beads, are produced industrially in a broad range of diameters, from 30nm to several micrometers, with various surface groups that can be used to bind proteins covalently. They are homogeneously labelled with a variety of ‡uorophores (Molecular Probes, Bangs, Seradyn). Unless stated otherwise, the spheres used in this work were orange-‡uorescent (530nm ex./560nm em.) carboxyl-modi...ed latex (CML) from Molecular probes. These were chosen, because this ‡uorophore is excitable by a two-photon process by the IR-trapping laser and a wide range of sizes with the same surface coating was available. Mostly 0.2¹m-beads were used: they have a nominal diameter of 0:2¹m and a measured radius of 108nm § 3:8%.

Adsorbing a protein coat The best method to bind proteins and especially antibodies proved to be adsorption. The conditions had to be optimized for each protein and bead because good adsorption depends strongly on the electric charges on both surface, but the protocol was based on the procedure applied by Sako and Kusumi (1995[?]). A good approximation for 0.2¹m CML-‡uorospheres (Molecular Probes) was an aqueous suspension of 1% spheres (» pH 6) incubated for 30 min. in 1mg/ml protein. This resulted in an almost completely covered surface. Before the coating step, the spheres were washed three times in borate-bu¤er (pH 9) to remove any solvent form the production process. The incubation bu¤er was a 50mM MES-bu¤er (pH 6). After the coupling the beads were washed in 10mg/ml FSG PBS.

Covalent coupling Covalent coupling o¤ers additional stability, but is a more elaborate procedure. The cross-linker used to link the protein to the sphere can also cross-link amino acids within the coating protein and damage its activity. This was a problem when using antibodies. These were therefore always adsorbed to the spheres. But covalently cross-linking o¤ered provided a way to introduce an extended linker, which was necessary for small proteins such as the Choleratoxin binding fragment used. In those case, biotinylated BSA was linked covalently to

the carboxyl-modi...ed latex spheres using carbodiimide (EDAC, Sigma) according to the protocols provided by Molecular Probes. After washing and blocking of the activated head-groups with ethanolamine, the biotinylated ChTx-B fragment was bound to the biotinylated BSA via streptavidin.

Estimating total amount of bound protein To optimize the binding protocols the amount of protein bound to the surface of the spheres was measured with the BCA-assay from Pierce (Germany). Bicinchoninic acid (BCA) is used to stabilize the product of the biuret reaction in which the protein reduces Cu^{+2} to Cu^{+1}. The resulting $BCA-Cu^{+1}$ complex adsorbes at 562nm and is stable, so that the beads could be ...ltered out before the measurement of the absorption.

Beads for the PFM imaging experiments

These carboxylate modi...ed latex spheres were coated with ...sh skin gelatine (FSG) (Sigma, Deisenhofen, Germany) to minimize unspeci...c adhesion according to the adsorption procedure above. The medium used in the PFM experiments contained free ...sh skin gelatine (FSG, 0:5mg=ml) (Sigma) to further reduce any adhesion between the bead and the plasma membrane.

Beads for SPT and noise analysis experiments

For the SPT tracking of the ganglioside GM_1 0.2^1m beads were covalently coated with biotinylated BSA (b-BSA) using EDAC. The biotinylated ChTx binding fragment was bound to these beads via streptavidin. This was done to include BSA as additional space for the small binding fragment of ChTx. The spheres to track the motion of proteins were bound via antibodies that were allowed to adsorb to the spheres surface (s. above). All spheres were incubated 30min at room temperature with 10mg/ml FSG to block the remaining surface and washed twice in 10mg/ml FSG in PBS.

To achieve paucivalent spheres the beads were incubated with the free ligand, i.e. PLAP (P3895, Sigma). In the case of PLAP, 15nl of the PLAP solution (1mg=ml; 15units=mg) was added to 10^1l spheres (1% solution). Adding 50nl of PLAP did block the binding completely.

A.2   Ligands and antibodies

Choleratoxin (ChTx) is a venom toxin that binds to the ganglioside GM_1. The wild-type toxin inserts into the membrane and forms pentamers with a pore in the center killing the host cell by this perforation of the plasma membrane.

For the studies of the di¤usion of the ganglioside GM1 in the hippocampal neurons the binding fragment of the choleratoxin molecule (ChTx-B fragment) was used. It was obtain from Sigma (Deisenhofen, Germany) pure and adsorbed to the spheres or biotinylated and bound via streptavidin and biontinylated BSA.

Antibodies

Because a concentration of about 1 mg=ml protein was required to coat 0:2 μm diameter carboxyl-modi...ed latex bead, it was not economic to purchase monoclonal antibodies in the required amount. Some experiments were performed using commercial monoclonal antibodies, but most antibodies were polyclonal from ascitic ‡uid or bleeding immunized rabbits, puri...ed and concentrated by running them through a Protein A-column, followed by dialysis.

- ² Thy1.1 - a monoclonal mouse anti rat Thy1.1 antibody (MRC OX-7) from Serotec (Oxford, England).

- ² PLAP - a polyclonal rabbit antibody raised at EMBL (Harder, EMBL) against the exoplamsic part of the human placental alkaline phosphatase (Plap). Some experiments were done with the monoclonal mouse anti-human Plap antibody (Clone (B6) from Daco (Glostrup, Denmark), but no di¤erence was observed.

- ² TrfR - a polyclonal antibody against the exoplasmic part of the human transferrin receptor (TrfR) which was produced by a hybridoma cell line (B3/25.2) obtained from Throwbridge. It does not cross-react with the endogenous hamster TrfR (Harder, pers. communication).

Appendix B

Cell culture and sample preparation

MDCK II epithelial and BHK ...broblast cells

Madine-Darby Canine Kidney cells (MDCK II) and baby-hamster kidney (BHK-21) cells were grown according to standard cell culture procedures, in tissue culture ‡ask in with supplemented eagles(E)-MEM and Glasgow(G)-MEM, respectively, and passaged every 2-3 days.

For the di¤usion studies on placenta-alkaline phosphatase (PLAP) and hemagglutinin (HA), the BHK cells were either transiently transfected using the lipofectamin system. T. Harder (EMBL) created a stable cell line, expressing PLAP, from the same BHK cell clone.

Hippocampal neurons

All experiments were performed on a primary culture of hippocampal neurons. These cells were extracted from 18 day old rat embryos, plated on poly-l-lysine coated cover slips in a dish that is preincubated with glia cells and grown at 37^0C and 5% CO_2 in N2-culture medium (Goslin and Banker, 1991[?]).

B.0.1   Samples for SFM and SPFM imaging

SFM studies on MDCK and BHK cells

Round glass coverslips (11mm) were used as substrate for the cells. These were cleaned and sterilized (either autoclaved or washed in acetone/ethanol and dried in sterile air). MDCK II epithelial cells were taken from the routine culture between the 3rd and 25th passage of the routine culture. They were plated at low density on the coverslips and then allowed to grow to con‡uence. For imaging of living cells, these were washed in ...ltered culture medium and imaged in the same. To ...x cells, they were washed in complemented phosphate-bu¤ered saline (PBS) and ...xed with 1% glutaraldehyde for four hours on ice.

SPFM experiments on hippocampal neurons

The imaging experiments were performed on 3-5 day old cultured cells to study the early development of the major processes and the growth cone morphology.

For the experiments on ...xed cells, the cells were washed twice in PBS, ...xed in 1% Glutaraldehyde for 10min at room temperature, washed three times in PBS and incubated for 10min in 50mM NH_4Cl to block any free aldehyde groups. Before the experiment they were washed again in PBS containing 10mg=ml FSG. The scanning experiments were carried out in the same solution. All solutions were ...ltered through $0:1^1m$ SuporeAcrodisc ...lters (Gelman Sciences, Ann Arbor, MI, USA).

For the images of living cells, part of the culture medium was removed from the dish, ...ltered and the beads were added. This way the composition of the medium during the experiment was maintained, including the nutritions provided by the glia cells. The cells were washed in medium plus 10mg=ml FSG and the microscope stage heated to $35^{\pm}C$.

B.0.2   Sample preparation for di¤usion studies

Studies on endogenous proteins

The neuron for the studies of di¤usion by single particle tracking and by thermal noise analysis, were treated the same way as the neurons for imaging of life cells.

The BHK cells for the noise analysis were plated at low density on sterilized cover slip, so that after 1-2 days there were still enough cells with free sides, on which the cells typically spread more, providing a ‡at membrane surface for the experiments. The experiments were carried out in GMEM with low CaNO concentration (0.35%), to avoid changes in the pH during the experiment due to interaction with oxygen.

Transfection of cells

The BHK ...broblasts were transfected 12-14 hours before the measurement using the lipofectamine (Gibco) according to the instructions of the manufacturer. The lipofectamine was mixed with Opti-MEM (Gibco) ($4^1l=100^1l$ per 30mm culture dish) and incubated at room temperature for 30min. to allow the formation micelles. The DNA ($\gg 2^1g$) encoding the protein of interest was mixed with medium and incubated with the lipofectamine 15min. Both were added to the cells and these incubated for 4 hours. The cells were cotransfected with a cytomplasmatic green ‡uorescent protein (E-GFP) to facilitate the search for successfully transfected cells during the experiment under the microscope.

Rat hepatocytes and acinar cells

The pancreas or liver were dissected out, chopped into $0:5mm^3$ pieces, and mildly agitated for 15 min. in a siliconized glass tube with oxygenated bu¤er A (98 mM NaCl, 4.8 mM KCl, 2 mM $CaCl_2$; 1.2 mM $MgCl_2$, 0.1% BSA, 0.01% SBTI, and 25 mM HEPES, pH 7.4) at 37^0C, containing 1000 units of collagenase. The suspension

of cells was ...ltered through a 224 ¹m Spectra-mesh polystyrene ...lter to remove large clumps of cells. The acini or hepatocytes were washed six times in ice-cold bu¤er A and plated on Cell-Tak-coated glass cover slips.

Appendix C

Documentation of the instruments

C.1   Details to the microscope set-up and the PFM

The video microscopy and the PFM were based on an inverted microscope (Axiovert 35, Zeiss, Jena, Germany) with standard DIC equipment (Zeiss) and an oil-immersion objective lens (Plan Neofluor 100x, Zeiss, Jena, Germany) with a high numerical aperture (NA=1.3). As DIC illumination a wavelength band around 700nm was used to minimize cell damage. The objective lens was mounted on a PiFoc (Physik Instrumente, Waldbronn, Germany), that allowed piezo-driven axial positioning over a range of $100\mu m$, and was inside a tempering foil. To move the sample chamber laterally in the focal plane a $100\mu m \times 100\mu m$ piezo scan stage with capacitive position sensors and digital feedback (Queensgate, New York, USA) was used. The images were recorded with a CCD (charge-coupled device) camera (Hamamatsu Photonics, Japan), amplified and background subtracted by an ARGUS-20 image processor (Hamamatsu Photonics, Japan) and stored on a S-VHS video recorder.

For the single particle tracking by video the video images were digitized by the perception video recorder (PVR) from Digital Processing Systems (DPS, Toronto, Canada). It is a video-editing board with integrated hard-disc controller that digitizes incoming images in real time, applies only reversible compression algorithms and stores each frame on a 9GB hard drive at speeds up to 6.5MB/s. The tracking software was developed on a SUN workstation [Nguyen-Ngoc, 1997].

To build the SPFM described in the section 7 a trapping laser (Nd:YVO4 laser, T20-B10-106Q, Spectra Physics) with 4W maximal light power was added. It was directed into the scanning optics via a scanning mirror mounted on a triple-axis piezo (PiezoSystems Jena, Germany). A photomultiplier (R2949, Hamamatsu, Herrsching, Germany) in photon counting mode together with a gated photon counter (5CI, Ortec, München, Germany) was used to measure the two-photon fluorescence intensity. Typical dark-count rates were 40-50 photon counts per second. To acquire images, laser intensities were used, that resulted in about 250 counts per ms integration time. As probes homogeneously labeled orange fluorescent (530/560) FluoSphere (Molecular Probes, Leiden, The Netherlands) with nominal diameter of
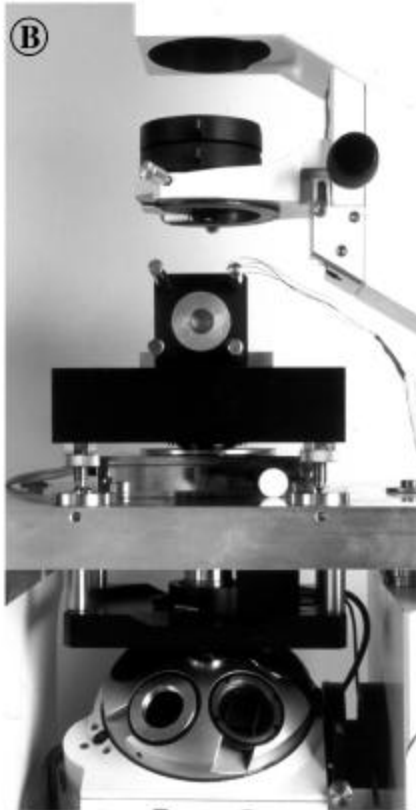
The PFM at EMBL: (A) overview of the set-up. (B) side-view displaying the alignment of the microscope lens mounted underneath the base-plate, the baseplate, and standing on it, the position detection system: the dichroic mirror (not visible) and the QPD (back of mount visible). (C) The piezo scanning stage.
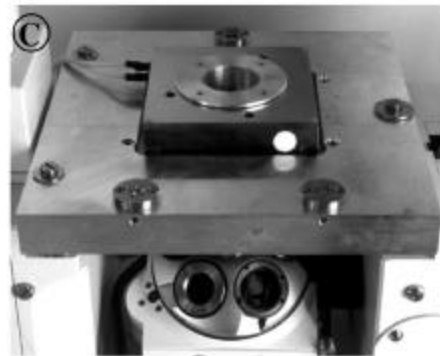
Figure C-1: The photonic force microscope at EMBL.

0.2¹m were used (r = 108nm § 3:8%). The surface of these polystyrene spheres was carboxyl-modi...ed.

For the thermal noise analysis in the PFM, a QPD (Hamamatsu Photonics, Japan) was mounted in the BFP to record the relative position of the trapped sphere from the forward scattered light. The signals of the four quadrants were ampli...ed and combined by a preampli...ers developed at EMBL to yield the signals for the three directions (x,y,z). All signals recorded were fed through ampli...ers developed at EMBL to adjust them to the input level of the A/D-converter board used and to ...lter out frequencies above the digitization frequency. To digitize all signals, to provide the signals for the scanning and to implement the axial position feedback a transputer-data acquisition board (ADWin F5, Jäger Electronics, Germany) was used. It contains two A/D-converters, 16Mb memory and a transputer programmable in ADWinBasic.

Bibliography

[1] B. Alberts, D. Bray, J. Lewis, M. Ra¤, K. Roberts, and J. D. Watson. Molecular Biology of the Cell. Cold Spring Harbor Laboratory, 1994.

[2] M. W. Allersma, F. Gittes, M. J. DeCastro, R. J. Stewart, and C. F. Schmidt. Two-dimensional tracking of ncd motility by backfocal interferometry. Biophys. J., 74:1074–1085, 1998.

[3] S. M. Altmann. Kraftspektroskopie an einzelnen Proteinen mit dem Rasterkraftmikroskop. Diplomarbeit, Universität Heidelberg. 1998.

[4] A. Ashkin. Optical trapping and manipulation of viruses and bacteria. Science, 235(4795):1517–1520, 1987.

[5] A. Ashkin, J. M. Dziedzic, J. E. Bjorkholm, and S. Chu. Observation of a single-beam gradient force optical trap for dielectric particles. Opt. Lett., 11:288–290, 1986.

[6] T. C. Bakker-Schut, G. Hesseling, D. G. "de Grooth", and J. Greve. Experimental and theoretical investigation on the validity of the geometrical optics model for calculating the stability of optical traps. Cytometry, 12:479–485, 1991.

[7] M. S. Bartlett. On the theoretical speci...cation of sampling properties of autocorrelated time series. J. Royal Stat. Soc., page 27, 1946.

[8] G. Binnig, C. F. Quate, and C. Gerber. Atomic force microscope. Phys. Rev. Lett., 56,9:930–933, 1986.

[9] S. M. Block, D. F. Blair, and H. C. Berg. Compliance of bacterial ‡agella measured with optical tweezers. Nature, 338(6215):514–518, 1989.

[10] S. M. Block, L. S. Goldstein, and B. J. Schnapp. Bead movement by single kinesin molecules studied with optical tweezers. Nature, 348(6299):348–352, 1990.

[11] J. M. Boggs. Lipid intermolecular hydrogen bonding: in‡uence on structural organization and membrane function. Biochim. Biophys. Acta, 906:353–404, 1987.

[12] M. Born and E. Wolf. Principles of Optics. Pergamon Press, Oxford, sixth edition, 1989.

[13] G. E. P. Box and G. M. Jenkins. Time Series Analysis. Holden-Day, San Francisco, 1976.

[14] M. S. Bretscher. Moving membrane up to the front of migrating cells. Cell, 85:465–467, 1996.

[15] D. A. Brown and E. London. Structure of detergent-resistant membrane domains: does phase separation occur in biological membranes ? Biochem. Biophys. Res. Comm., 240:1–7, 1992.

[16] D. A. Brown and J. K. Rose. Sorting of GPI-anchored proteins to glycolipid-enriched membrane subdomains during transport to the apical cell surface. Cell, 68:533–544, 1992.

[17] R. E. Brown. Sphingolipid organization in biomembranes: what physical studies of model membranes reveal. J. Cell Sci., 111:1–9, 1998.

[18] N. A. Burnham. Accounting for the Sti¤ness of the Probe and Sampling in Scanning Probe Microscopy. Journal of Vacuum Science Technology B 12(3), pages 2219–2221, 1994.

[19] S. Chandrasekhar. Stochastic problems in physics and astronomy. Rev. Mod. Phys., 15(1):2–87, 1943.

[20] R. J. Cherry and R. E. Godfrey. Anisotropic rotation of bacteriorhodopsin in lipid membranes. Comparison of theory with experiment. Biophys. J., 36(1):257–276, 1981.

[21] C. M. Cohen, J. M. Tyler, and D. Branton. Spectrin-actin associations studied by electron microscopy of shadowed preparations. Cell, 21(3):875–883, 1980.

[22] A. M. Craig, R. J. Wyborski, and G. Banker. Preferential addition of newly synthesized membrane protein at axonal growth cones. Nature, 375(6532):592–594, 1995.

[23] J. Dai, , and M. P. Sheetz. Mechanical properties of neuronal growth cone membranes studied by tether formation with optical tweezers. Biophys. J., 68(3):988–996, 1995.

[24] J. Dai and M. P. Sheetz. Axon membrane ‡ows from the growth cone to the cell body. Cell, 83(5):693–701, 1995.

[25] M. De Brabander, R. Nuydens, H. Geerts, and C. R. Hopkins. Dynamic behavior of the transferrin receptor followed in living epidermoid carcinoma cells by nanovid microscopy. Cell Motil. Cytoskeleton, 9:30–47, 1988.

[26] W. Denk and K. Svoboda. Photon upmanship: why multiphoton imaging is more than a gimmick. Neuron, 18(3):351–357, 1997.

[27] W. Denk and W. W. Webb. Optical measurements of picometer displacements of transperent microscopic objects. Appl. Opt., 29:2382–2391, 1990.

[28] B. Drake, C. B. Prater, A. L. Weisenhorn, S. A. G. T. R. Albrecht, C. F. Quate, D. S. Cannell, H. G. Hansma, and P. K. Hansma. Imaging crystals, polymers, and processes in water with the atomic force microscope. Science, 243(4898), 1989.

[29] E. A. Dratz, G. P. Miljanich, P. P. Nemes, J. E. Gaw, and S. Schwartz. The structure of rhodopsin and its disposition in the rod outer segment disk membrane. Photochem. Photobiol., 29(4):661–670, 1979.

[30] R. Eckert. Adsorption von Proteinen auf gesputterten Ober‡ächen. Diplomarbeit, Fakultät für Physik und Astronomie, Universität Heidelberg, 1996.

[31] S. Eskandari, E. M. Wright, M. Kreman, D. M. Starace, and G. A. Zampighi. Strutural analysis of cloned plasma membrane proteins by freeze-fracture electron microscopy. Proc. Natl. Acad. Sci., 95:11235–11240, 1998.

[32] J. T. Finer, R. M. Simmons, and J. A. Spudich. Single myosin molecule mechanics: piconewton forces and nanometer steps. Nature, 368:113–118, 1994.

[33] E.-L. Florin, J. K. H. Hörber, and E. H. K. Stelzer. High-resolution axial and lateral position sensing using two-photon excitation of ‡uorophores by continuous Nd:YAG laser. Appl. Phys. Lett., 69:446–448, 1996.

[34] E.-L. Florin, V. T. Moy, and H. E. Gaub. Adhesion forces between individual ligand-receptor pairs. Appl. Phys. A, 264(5157):415–417, 1994.

[35] E.-L. Florin, A. Pralle, J. K. H. Hörber, and E. H. K. Stelzer. Photonic force microscope based on optical tweezers and two-photon excitation for biological applications. J. Struct. Biol., 119:202–211, 1997.

[36] E.-L. Florin, A. Pralle, E. H. K. Stelzer, and J. K. H. Hörber. Calibration of photonic force microscope by Boltzmann statistics. Appl. Phys. A, 66:S75–78, 1998.

[37] H. Geerts, M. De Brabander, R. Nuydens, G. Geuens, M. Moeremans, J. Mey, and P. Hollenbeck. Nanovid tracking: a new automatic method for the study of mobility in living cells based on colloid gold and video microscopy. Biophys. J., 952:772–782, 1987.

[38] J. Gelles, B. J. Schnapp, and M. P. Sheetz. Tracking kinesin-driven movements with nanometer-scale precision. Nature, 331:450–453, 1988.

[39] R. N. Ghosh and W. W. Webb. Automated detection and tracking of individual cell surface LDL-receptor molecules. Biophys. J., 66:1301–1318, 1994.

[40] L. P. Gishlain, N. A. Switz, and W. W. Webb. Measurement of small forces using an optical trap. Rev. Sci. Instrum., 65:2762–2768, 1994.

[41] L. P. Gishlain and W. W. Webb. Scanning-force microscope based on an optical trap. Opt. Lett., 18:1678–1680, 1993.

[42] F. Gittes and C. F. Schmidt. Interference model for back focal plane displacement detection in optical tweezers. Opt. Lett., 1998.

[43] K. Goslin and G. Banker. Culturing nerve cells. M.I.T. Press, Cambridge, MA, 1991.

[44] W. Häberle, J. H. K. Hörber, F. Ohnesorge, D. P. Smith, and G. Binnig. In situ investigations of single living cells infected by viruses. Ultramicroscopy, 42-44(B):1161–1167, 1992.

[45] Q. Hale. Optical constants of water in the 200nm to 200¹m wavelength region. Appl. Optics, 12:555–563, 1973.

[46] P. K. Hansma, J. P. Cleveland, M. Radmacher, D. A. Walters, M. Bezanilla, M. Fritz, D. Vie, H. G. Hansma, C. B. Prater, J. Massie, L. Fukunaga, J. Gurley, and V. Elings. Tapping mode atomic force microscopy in liquids. Applied Physics Letters, 64(13):1738–1740, 1994.

[47] J. Happel and H. Brenner. Low Reynolds Number Hydrodynamics. Prentice Hall, New Jersey, 1965.

[48] T. Harder, P. Schei¤ele, P. Verkade, and K. Simons. Lipid-domain structure of the plasma membrane revealed by patching of membrane components. J. Cell Biol., 141(4):929–942, 1998.

[49] E. Henderson, P. G. Haydon, and D. S. Sakaguchi. Actin ...lament dynamics in living glial cells imaged by atomic force microscopy. Science, 257:1944–1946, 1992.

[50] R. M. Hochmuth and E. A. Evans. Mechanochemical properties of membranes. Biophys. J., 30:747–762, 1982.

[51] R. M. Hochmuth, J. Shao, J. Dai, and M. P. Sheetz. Deformation and ‡ow of membrane into tethers extracted from neuronal growth cones. Biophys. J., 70:358–369, 1996.

[52] J. H. Hoh, G. E. Sosinsky, J. P. Revel, and P. K. Hansma. Structure of the extracellular surface of the gap junction by atomic force microscopy. Biophys. J., 65(1):149–163, 1993.

[53] B. D. Hughes, B. A. Pailthorpe, and L. R. White. The translational and rotational drag on a cylinder in a membrane. J. Fluid Mech., 111:65–74, 1981.

[54] J. D. Jackson. Classical Electrodynamics. John Wiley Sons, New York, second edition, 1986.

[55] K. A. Jacobson, A. Ishihara, and R. Inman. Lateral di¤usion of proteins in membranes. Annu. Rev. Physiol., 49:163–175, 1987.

[56] B. P. Jena, P. Pad...eld, T. S. Ingebritsen, and J. D. Jamieson. Protein tyrosine phosphatase stimulates Ca(2+)-dependent amylase secretion from pancreatic acini. J. Biol. Chem., 266(27):17744–17746, 1991.

[57] P. Keller and K. Simons. Post-Golgi biosynthetic tra¢cking. J. Cell Sci., 110(24):3001–3009, 1997.

[58] K. Kinosita, Jr., R. Kataoka, Y. Kimura, O. Gotoh, and A. Ikegami. Dynamic structure of biological membranes as probed by 1,6-diphenyl-1,3,5-hexatriene: a nanosecond ‡uorescence depolarization study. Biochem., 20(15):4270–4277, 1981.

[59] T. Kobayashi, B. Storri, K. Simons, and C. G. Dotti. A functional barrier to movement of lipids in polarized neurons. Nature, 359(6396):647–650, 1992.

[60] A. Kusumi and Y. Sako. Cell surface organization by the membrane skeleton. Curr. Opin. Cell Biol., 8:566–574, 1996.

[61] A. Kusumi, Y. Sako, and M. Yamamoto. Con...ned lateral di¤usion of membrane receptors as studied by single particle tracking (nanovid microscopy). e¤ects of calcium-induced di¤erentiation in cultured epithelial cells. Biophys. J., 65:1227–1240, 1993.

[62] H. Lamb. Hydrodynamics. Cambridge University Press, New York, 1932.

[63] M. Langer. Entwicklung eines Rasterkraftmikroskops zur Untersuchung der elastischen Eigenschaften von Mechanosensoren im Innenohr. Dissertation, U Tübingen. Dissertation, U Tübingen, 1998.

[64] C. Le Grimellec, E. Lesniewska, C. Cachia, J. P. Schreiber, F. de Fornel, and J. P. Goudonnet. Imaging of the membrane surface of MDCK cells by atomic force microscopy. Biophys. J., 67:36–41, 1994.

[65] C. Le Grimellec, E. Lesniewska, M. Giocondi, E. Finot, V. Vié, and J. Goudonnet. Imaging of the surface of living cells by low-force contact-mode atomic force microscopy. Biophys. J., 75:695–703, 1998.

[66] M. D. Ledesma, K. Simons, and C. G. Dotti. Neuronal polarity: essential role of protein-lipid complexes in axonal sorting. Proc. Natl. Acad. Sci., 95(7):3966–3971, 1998.

[67] G. U. Lee, L. A. Chrisey, and R. J. Colton. Direct measurement of the forces between complementary strands of DNA. Science, 266(5186):771–773, 1994.

[68] C. LeGrimellec, E. Lesniewska, C. Cachia, J. P. Schreiber, F. de Fornel, and J. P. Goudonnet. Imaging of the membrane surface of MDCK cells by atomic force microscopy. Biophys. J., 67(1):36–41, 1994.

[69] C. LeGrimellec, E. Lesniewska, M. C. Giocondi, E. Finot, V. Vie, and J. P. Goudonnet. Imaging of the surface of living cells by low-force contact-mode atomic force microscopy. Biophys. J., 75(2):695–703, 1998.

[70] P. A. Liebman and E. N. Pugh, Jr. The control of phosphodiesterase in rod disk membranes: kinetics, possible mechanisms and signi...cance for vision. Vision Res., 19:375–380, 1979.

[71] Y. Liu, D. K. Chen, G. J. Snoek, M. W. Berns, C. F. Chapman, and B. J. Tromberg. Evidence for localized cell heating induced by infrared optical tweezers. Biophys. J., 68(5):2137–2144, 1995.

[72] A. Meller, R. Bar-Ziv, T. Tlusty, E. Moses, J. Stavans, and S. A. Safran. Localized dynamic light scattering: A new approach to dynamic measurements in optical microscopy. Biophys. J., 74:1541–1548, 1998.

[73] I. Mellman, E. Yamamoto, J. A. Whitney, M. Kim, W. Hunziker, and K. Matter. Molecular sorting in polarized and non-polarized cells: common problems, common solutions. J. Cell Sci. Suppl., 17:S1–S7, 1993.

[74] K. Miller, M. Shipman, I. S. Trowbridge, and C. R. Hopkins. Transferrin receptors promote the formation of clathrin lattices. Cell, 65:621–632, 1991.

[75] D. Müller, A. Engel, and M. Amrein. Preparation techniques for the observation of native biological systems with the atomic force microscope. Biosensors and Bioelectronics, 12(8):867–877, 1997.

[76] V. Moy, E.-L. Florin, and H. Gaub. Intermolecular forces and energies between ligands and receptors. Science, 265:257–259, 1994.

[77] D. Müller, M. Amrein, and A. Engel. Adsorption of biological molecules to a solid support for scanning probe microscopy. J. Struct. Biol., 119:172–188, 1997.

[78] D. Müller, C.-A. Schoenenberger, F. Schabert, and A. Engel. Structural changes in native membrane proteins monitored at subnanometer resolution with the atomic force microscope: A review. J. Struct. Biol., 119:149–157, 1997.

[79] S. Nguyen-Ngoc. Détection et suivi d'objets biologiques par ...ltrage adaptatif. application á des séquences de vidéo-microscopie. Rapport de stage IGE2, EMBL, Heidelberg, and E.N.S. de Télécommunication, Paris, 1996.

[80] G. L. Nicolson, V. T. Marchesin, and S. L. Singer. The localization of spectrin on the inner surface of human red blood cell membranes by ferritin-conjugated antibodies. J. Cell Biol., 51(1):265–272, 1971.

[81] S. Nir and W. D. Stein. Two modes of di¤usion in liquids. J. Chem. Phys., 55:1598–1603, 1971.

[82] J. P. Noll. Aufbau und Charakterisierung einer Optischen Pinzette. Diplomarbeit, Universität Heidelberg. 1997.

[83] R. G. Parton and K. Simons. Digging into caveolae. Science, 269:1398–1399, 1995.

[84] R. Peters and R. J. Cherry. Lateral and rotational di¤usion of bacteriorhodopsin in lipid bilayers: experimental test of the Sa¤man-Delbrück equations. Proc. Natl. Acad. Sci., 79(14):4317–4321, 1982.

[85] R. Peters and R. J. Cherry. Free volume model for lipid lateral di¤usion coe₡cients. Assessment of the temperature dependence in phosphatidylcholine and phosphatidylethanolamine bilayers. Biochim. Biophys. Acta, 862(1):231–234, 1986.

[86] M.-M. Poo and R. A. Cone. Lateral di¤usion of rhodopsin in the photoreceptor membrane. Nature, 247(441):438–441, 1974.

[87] A. Pralle, E.-L. Florin, E. H. K. Stelzer, and J. K. H. Hörber. Local viscosity probed by photonic force microscopy. Appl. Phys. A, 66:S71–73, 1998.

[88] A. Pralle, M. Prummer, E.-L. Florin, E. H. K. Stelzer, and J. K. H. Hörber. Three-dimensional high-resolution particle tracking for optical tweezers by forward scattered light. Micro. Res. and Tech., 1998.

[89] D. C. Prieve, S. G. Bike, and N. A. Frej. Brownian motion of a single mircoscopic sphere in a colloid force …eld. Faraday Discuss. Chem. Soc., 90:209–222, 1990.

[90] M. Prummer. Kraftspektroskopie an einzelnen Polymermolekülen mit der Optischen Pinzette. Diplomarbeit, Fakultät für Physik und Astronomie, Universität Heidelberg, 1998.

[91] C. A. J. Putman, K. O. Van der Weerf, B. G. De Grooth, N. F. Van Hulst, and J. Greve. Tapping mode atomic force microscopy in liquids. Applied Physics Letters, 64(18):2454–2456, 1994.

[92] J. Rädler and E. Sackmann. Langmuir, 8:848–853, 1992.

[93] M. Radmacher, R. W. Tillmann, M. Fritz, and H. E. Gaub. From molecules to cells: imaging soft samples with the atomic force microscope. Science, 257(5078):1900–1905, 1992.

[94] M. Radmacher, R. W. Tillmann, and H. E. Gaub. Imaging viscoelasticity by force modulation with the atomic force microscope. Biophys. J., 64:735–742, 1993.

[95] F. Reif. Fundamentals of statistical and thermal physics. MacGraw-Hill, New York, 1965.

[96] M. Rief. Kraftspektroskopie an einzelnen Molekülen. Dissertation, LMU München. Dissertation, LMU München, 1997c.

[97] M. Rief, M. Gautel, F. Oesterhelt, J. M. Fernandez, and H. E. Gaub. Reversible unfolding of individual titin immunoglobulin domains by AFM. 1997.

[98] M. Rief, F. Oesterhelt, B. Heymann, and H. E. Gaub. Single molecule force spectroscopy on polysaccharides by atomic force microscopy. 1997.

[99] M. J. Rindler, I. E. Ivanov, H. Plesken, E. Rodriguez-Boulan, and D. D. Sabatini. Viral glycoproteins destined for apical or basolateral plasma membrane domains traverse the same Golgi apparatus during their intracellular transport in doubly infected Madin-Darby canine kidney cells. J. Cell Biol., 98(4):1304–1319, 1984.

[100] P. G. Sa¤man and M. Delbrück. Brownian motion in biological membranes. Proc. Natl. Acad. Sci., 72:3111–3113, 1975.

[101] Y. Sako and A. Kusumi. Compartmentalized structure of the plasma membrane for receptor movements as revealed by nanometer-level motion analysis. J. Cell Biol., 125:1251–1264, 1994.

[102] Y. Sako and A. Kusumi. Barriers for lateral di¤usion of transferrin receptors in the plasma membrane as characterized by receptor dragging by laser tweezers: fence versus tether. J. Cell Biol., 129:1559–1574, 1995.

[103] B. E. A. Saleh and M. C. Teich. Fundamentals of Photonics. John Wiley Sons, New York, 1991.

[104] M. B. Sankaram and T. E. Thompson. Interaction of cholesterol with various glycerophospholipids and sphingomyelin. Biochemistry, 29:10670–10684, 1990.

[105] M. Saxton and Owicki. Biochim. and Biophys. Acta, 979:27–, 1989.

[106] M. J. Saxton. Lateral di¤usion in an archipelago. The e¤ect of mobile obstacles. Biophys. J., 52:989–997, 1987.

[107] M. J. Saxton. Lateral di¤usion in an archipelago. Distance dependence of the di¤usion coe₵cient. 1989.

[108] M. J. Saxton. Lateral di¤usion and aggregation. A Monte Carlo study. Biophys. J., 61:119–128, 1992.

[109] P. Schei¤ele, M. G. Roth, and K. Simons. Interaction of in‡uenza virus haemagglutinin with sphingolipid-cholesterol membrane domains via its transmembrane domain. EMBO J., 16(18):5501–5508, 1997.

[110] C. Schneider and J. G. Williams. Molecular dissection of the human transferrin receptor. J. Cell Sci. Suppl., 3:139–149, 1985.

[111] R. Schroeder, E. London, and D. A. Brown. Interactions between saturated acyl chains confer detergent resistance to lipids and glycosylphosphatidylinositol (GPI)-anchored proteins: GPI-anchored proteins in liposomes and cells show similar behavior. Proc. Natl. Acad. Sci., 91:12130–12134, 1994.

[112] K. Simons and E. Ikonen. Functional rafts in cell membranes. Nature, 387(6633):569–572, 1997.

[113] K. Simons and G. van Meer. Lipid sorting in epithelial cells. Biochemistry, 27(17):6197–6202, 1988.

[114] S. L. Singer and G. L. Nicolson. The ‡uid mosaic model of the structure of cell membranes. Science, 175(23):720–731, 1972.

[115] K. Svoboda and S. M. Block. Biological applications of optical forces. Ann. Rev. Biophys. Biomol. Struct., 23:247–285, 1994.

[116] K. Svoboda, C. F. Schmidt, B. J. Schnapp, and S. M. Block. Direct observation of kinesin stepping by optical trapping interferometry. Nature, 365(6448):721–727, 1993.

[117] S. Tsukita and H. Ishikawa. Cytoskeletal network underlying the human Erythrocyte membrane. Thin-section electron microscopy. J. Cell Biol., 85(3):567–576, 1980.

[118] G. E. Uhlenbeck and L. S. Ornstein. On the Theory of the Brownian Motion. Rev. of Mod. Phys., pages 823–841, 194.

[119] G. van Meer, E. H. K. Stelzer, R. W. Wijnaendts-van-Resandt, and K. Simons. Sorting of sphingolipids in epithelial (Madin-Darby canine kidney) cells. J. Cell Biol., 105(4):1623–1635, 1987.

[120] R. Varma and S. Mayor. Gpi-anchored proteins are organized in submicron domains at the cell surface. Nature, 6695:798–801, 1998.

[121] W. L. C. Vaz and P. F. F. Almeida. Phase topology and percolation in multiphase lipid bilayers: is the biological membrane a domain mosaic. Curr. Opin. Struct. Biol., 3:482–488, 1993.

[122] W. L. C. Vaz, C. Goodsai-Zalduondo, and K. A. Jacobson. Lateral di¤usion of lipids and proteins in bilayer membranes. FEBS, 172, 1984.

[123] K. Visscher and G. J. Brakenho¤. Theoretical study of optically induced forces on spherical particles in a single beam trap I: Rayleigh scatterers. Optik, 89:174–180, 1992.

[124] K. Visscher and G. J. Brakenho¤. Theoretical study of optically induced forces on spherical particles in a single beam trap II: Mie scatterers. Optik, 90:57–60, 1992.

[125] M. C. Wang and G. E. Uhlenbeck. On the Theory of the Brownian Motion II. Rev. of Mod. Phys., pages 323–342, 1945.

[126] J. D. Watson, N. H. Hopkins, J. W. Roberts, J. A. Steitz, and A. M. Weiner. Molecular biology of the gene. The Benjamin/Cumminggs Pub. Co., Menlo Park, CA, forth edition, 1988.

[127] R. E. Waugh. Surface viscosity measurements from large bilayer vesicle tether formation. II. Experiments. Biophys. J., 38:29–37, 1982.

[128] D. C. Wiley, I. A. Wilson, and J. J. Skehel. Structural identi...cation of the antibody-binding sites of Hong Kong in‡uenza haemagglutinin and their involvement in antigenic variation. Nature, 289:373–378, 1981.

[129] I. A. Wilson, J. J. Skehel, and D. C. Wiley. Structure of the haemagglutinin membrane glycoprotein of in‡uenza virus at 3Åresolution. Nature, 289:366–373, 1981.

[130] B. Winckler and M. M. Poo. No di¤usion barrier at axon hillock. Nature, 379(6562):213, 1996.

[131] T. Wohland, A. Rosin, and E. H. K. Stelzer. Theoretical determination of the in‡uence of the polarization on forces exerted by optical tweezers. Optik, 102:181–190, 1996.

Acknowledgment

Curriculum Vitae

name	Arnd Pralle
born	on July 17th, 1969, in Bremen
citizenship	German
parents	Hans and Gisela Pralle

9/75-6/79	Elementary school in Großen-Buseck
9/79-6/88	High school at the Landgraf-Ludwig Schule, Gießen
9/85-6/86	High school at Lakeville High, Lakeville, MI
10/88-6/94	Study of Physics at the Justus-Liebig-U., Gießen
9/91-7/92	Grad. studies at the U. of Washington, Seattle, WA (supported by an DAAD stipend)
10/92-2/94	Diploma thesis work at the research center Jülich in the group of Prof. C. Heiden
since 10/94	PhD studies at the European Molecular Biology Laboratory in Heidelberg and at the Ludwig-Maximilians-University, Munich (supported by an EMBL fellowship)